Washington University in St. Louis

Washington University Open Scholarship

McKelvey School of Engineering Theses & Dissertations

McKelvey School of Engineering

5-6-2022

Optical imaging and VHH screening for brain molecular MRI contrast agent development

Shiran Su
Washington University in St. Louis

Follow this and additional works at: https://openscholarship.wustl.edu/eng_etds

WASHINGTON UNIVERSITY IN ST. LOUIS

McKelvey School of Engineering

Department of Biomedical Engineering

Dissertation Examination Committee:
Dennis Barbour, Chair
Hongyu An
Philip Bayly
David Brody
Vijay Sharma

Optical Imaging and VHH Screening for Brain Molecular MRI Contrast Agent Development
by
Shiran Su

A dissertation presented to
The Graduate School
of Washington University in
partial fulfillment of the
requirements for the degree
of Doctor of Philosophy

May 2022
St. Louis, Missouri

Table of Contents

List of Figures

List of Tables

List of Abbreviations

Aβ: amyloid-β
AD: Alzheimer's Disease
AICc: small sample corrected Akaike information criterion
BBB: blood brain barrier
BLI: bio-layer interferometry
BSA: bovine serum albumin
cDNA: complimentary DNA
CNS: central nervous system
ESIONs: extremely small iron oxide nanoparticles
HCAbs: heavy chain-only antibodies
IONPs: iron oxide nanoparticles
IPTG: isopropyl-beta-D-thiogalactoside
IV: intravenous
mPEG: poly(ethylene glycol) methyl ether
MRA: magnetic resonance angiography
mTfR: mouse transferrin receptor
NIR: near infrared
NT: neurotensin
PBMC: peripheral blood mononuclear cell
PBS: phosphate Buffered Saline
PEG: polyethylene glycol
phosphoryl trichloride
PK: pharmacokinetics
PO-PEG: PEG-derivatized phosphine oxide
RES: reticuloendothelial system
RIA: radioimmunoassay
RMT: receptor-mediated transcytosis
ROI: regions of interest
ROS: reactive oxygen species
scFv: single chain variable fragment
SEC: size exclusion chromatography
SPIONs: superparamagnetic oxide nanoparticles
TEM: transmission electron microscopy
TfR: transferrin receptor
TGA: thermogravimetric analysis
VHH: single domain antibodies

<u>Acknowledgments</u>

This thesis work would not have been possible without the following people:

First and foremost, I would like to thank my mentor, Dr. David Brody for being extremely supportive and helpful throughout my entire thesis study. His passion for science has always inspired me to work hard and push my boundaries. The discussions with Dr. Brody about my thesis work helped me to understand how to do research and grew to be a more mature scientist. I not only learned about how to do science, but also learned to be a better person.

Second, I would like to thank all members of the Brody lab who have been so friendly, helpful, and supportive throughout the years. I would like to thank Mihika for her patience and guidance. I would especially like to thank TJ for his direction and support for my thesis work. I learned so many techniques from TJ and it has been such a valuable experience learning from TJ.

Third, I would like to thank my thesis committee for their valuable suggestions and guidance. They helped me stay on track during my thesis study.

Also, I would like to thank the staff who worked in the animal facility and mouse imaging facility at NIH who provided a great space and resources for my thesis work. I would like to thank Rolf Swenson and Haitao Wu from the NIH Chemistry and Synthesis Center for helping with IONP

Dedicated to my parents

ABSTRACT OF THE DISSERTATION

Optical Imaging and VHH Screening for Brain Molecular MRI Contrast Agent Development

by

Shiran Su

Doctor of Philosophy in Biomedical Engineering

Washington University in St. Louis, 2022

Professor Dennis Babour, Chair

Alzheimer's disease (AD) is one of the most important causes of dementia in the elderly. With no effective therapies to cure or inhibit AD symptom progression, AD severely decreases patients' quality of life and creates an enormous burden on the health care system and society. Currently, clinical AD diagnosis is based on cognition and the relative impact of impairments on daily activities. However, multiple neurodegenerative and vascular pathologies can coexist and produce cognitive and behavioral symptoms which could overlap with each other. This makes it difficult to accurately identify pathology based solely on clinical symptoms. Imaging methods including structural MRI which detects brain atrophy, and PET for assessing brain amyloid-beta (Aβ), tau, and glucose metabolism have been developed to aide AD diagnosis. However, PET images have limited resolution and expose patients to radiation. Structural MRI lacks specificity and does not allow visualization of the histological markers for AD, Aβ or Tau. There is an unmet need for developing MRI molecular imaging methods which allow direct, non-invasive, high-resolution detection and measurement of specific AD markers and many other pathologies in the brains of living patients.

This dissertation developed imaging methods and mathematical models to aid the development of a novel family of brain MRI molecular contrast agents. This family of contrast agents has several modules, including an ultra-small iron oxide nanoparticle (IONP) core for T1 MRI contrast, a polyethylene glycol- based coating to prevent nonspecific fouling of the iron oxide core, a single-domain antibody fragment from camelid (VHH, also referred to as Nanobody) which targets the transferrin receptor (TfR) on brain endothelial cells for blood brain barrier transcytosis, another VHH that targets the specific pathology of interest (in this case the AD hallmark $A\beta$ in brain parenchyma), and a near-infrared (NIR) fluorescence dye for tracking in mice. An efficient NIR imaging method was established to monitor VHH and VHH conjugated IONP kinetics in mice using a hybrid approach: kinetics in blood were assessed by direct sampling, and kinetics in kidney, liver, and brain were assessed by serial in vivo NIR imaging. Based on the hybrid approach, a five-compartment pharmacokinetic model (PK) has been constructed. This PK model fits the NIR imaging data well and could be used to understand and predict contrast agent PK during the development phase. After understanding the biodistribution and clearance of the VHHs and IONPs in vivo, a VHH screening system based on neurotensin was developed to rapidly test for blood brain barrier transcytosis. This VHH screening system identified a VHH with good blood-brain barrier crossing ability and the target engagement in brain of this VHH was further analyzed using a mouse model of AD-related $A\beta$ pathology. The establishment of the feasibility of these methods lays a foundation for future development of the brain MRI molecular contrast agents. In the future, the family of molecular contrast agents could be used to assess many other neurological disorders and provide a direct assessment of target engagement in response to candidate therapeutics.

Chapter 1: Introduction

Neurological disorders affect millions of people worldwide, but at present our ability to assess these disorders objectively and quantitatively is limited [1]. Improvements in the assessment of neurological disorders would allow for disease progression monitoring and provide direct assessment of candidate therapeutics [2-5]. The ultimate goal of this project is to develop a brain MRI molecular contrast agent which is able to get across blood brain barrier (BBB) through transferrin receptor mediated transcytosis and binds to the brain targets of the neurological disorders such as tau, α-synuclein, etc. This contrast agent is consisted of four modules. The first module is the extremely small 3nm iron oxide core to provide MRI T1 signal; the second module is the PEG to prevent fouling of the nanoparticle and provide binding sites for the third module, the singlet domain antibodies (VHHs) which bind to the TfR for BBB transcytosis then bind to brain targets. The fourth module is the near infrared dye to study the PK of the contrast agent in vivo. For the proof of concept, a contrast agent for diagnosis of Alzheimer's disease (AD) has been developed.

AD is one of the most important causes of dementia in the elderly [6]. About 6.2 million Americans are living with AD, and it's predicted that the number will increase to 13.8 million by 2050 [7]. With no effective therapies to cure or inhibit significant AD symptom progression[8], AD severely decreases patients' quality of life and creates an enormous burden on the health care system and society [6, 9]. Currently, clinical AD diagnosis is based on cognition and the relative impact of

impairments on daily activities [10]. However, multiple neurodegenerative and vascular pathologies can coexist and produce cognitive and behavioral symptoms which could overlap with each other [11]. This makes it difficult to accurately identify pathology based solely on clinical symptoms. The accuracy of clinical diagnosis of AD at the National Institute of Aging and National Institute of Aging sponsored AD centers varies depending on the clinical and neuropathologic criteria used [12]. The sensitivity of AD diagnosis ranges from 70.9% to 87.3%, whereas specificity ranges from 44.3% to 70.8%, which need to be improved. Imaging methods including MRI and PET have been developed to aid the diagnosis of AD [13, 14]. However, PET imaging for AD provides limited resolution and requires radiation exposure. Structural MRI lacks specificity and does not allow direct visualization of amyloid plaques β (Aβ) or tau, the histological hallmarks of AD. There is an unmet need for developing methods like molecular contrast MRI which have better resolution than PET and better specificity than structural MRI imaging.

In this study, iron oxide nanoparticles (IONPs) conjugated to VHHs and labeled with a near-infrared (NIR) fluorescent dye were injected intravenously (IV) into mice. The pharmacokinetics (PK) of VHHs alone and VHH conjugated IONPs were monitored using a high resolution NIR scanner. Fluorescence signal change in mouse head, kidney, and liver were imaged over a period of two days post injection to qualitatively and quantitatively understand the PK of the nanoparticles. A five compartment PK model was constructed to describe the relationship between in vivo PK and hydrodynamic size following single bolus IV injection. To efficiently and rapidly screen VHHs for transferrin receptor (TfR) mediated BBB transcytosis, mouse TfR-binding VHHs were generated, and a neurotensin (NT) based modular screening system was established. This screening system includes four modules. The first module is an anti-mTfR VHH for receptor mediated transcytosis across the BBB; the second module is the neurotensin peptide for assessment

of target engagement in vivo through measurement of hypothermia. The third module is a dimer of anti-Aβ VHHs for disease-relevant brain target engagement. The fourth module is a fluorescence dye for visualization of VHH constructs in situ.

This study found that increasing VHH and nanoparticle size results in a switch from kidney dominant clearance to liver dominant clearance, which is consistent with past findings. The use of mathematical PK models provides a quantitative method to study the relationship between PK parameters and nanoparticle/VHH sizes and can be used to explore the in vivo pharmacokinetics and distribution of other VHHs and nanoparticles for future studies. The modular VHH screening system was used to identify a VHH variant with good BBB transcytosis ability. The identified VHH variant was conjugated to a payload to evaluate the brain target engagement using post-mortem confocal microscopy. This study established a foundation to understand the PK of IONPs and to screen VHH variants. The near-infrared methods for PK assessment and the PK model will be incorporated and modified for describing novel VHH-IONP in vivo PK characteristics to guide the development of the brain MRI molecular contrast agent. The VHH screening system will be adjusted and utilized to identify more appropriate VHHs for the future brain MRI molecular contrast agents.

The work described in Chapter 3 has been published in *International Journal of Molecular Sciences*, and that the work described in Chapter 4 has been submitted to *Fluids and Barriers of the CNS*.

1.1   Iron Oxide Nanoparticles

Iron oxide nanoparticles have been widely used for medical applications including cancer diagnosis and treatment [15, 16], treatment of iron deficiency anemia [15], enhanced blood pool

and tumor MRI imaging [17, 18], MRI molecular imaging [19-22] and magnetic resonance angiography (MRA) [23]. Sillerud et al. synthesized a novel MRI contrast agent by conjugating superparamagnetic oxide nanoparticles (SPIONs) with anti-amyloid-beta precursor protein (AβPP) antibodies to specifically target amyloid-beta plaques [24]. Iron oxide nanoparticles have also been functionalized with single-chain antibodies (scFv) against activated platelets for T1 and T2- weighted MRI of thrombi [19]. IONPs are considered relatively safe and do not induce cytotoxicity below 100 μg/ml in vitro [25]. MRI Molecular contrast agents based on iron oxide nanoparticles have good biocompatibility, at least in part because human blood and tissues are naturally rich in iron [26, 27]. The FDA has approved an IONP, Ferumoxytol, for treatment of iron-deficiency anemia in patients with chronic kidney disease [28]. Ferumoxytol is also used off-label as a contrast agent for MR angiography in patients with impaired renal function as well [29] and no major safety concerns have been reported. In a widely cited publication, Kim et al [18] demonstrated that homogenous size iron oxide nanoparticle cores for MR imaging could be synthesized at large scales. Their extremely small 3nm iron oxide nanoparticles (ESIONs) were shown to have a high r1 relaxivity of 4.78 mM-1s-1 at 3T and low r2/r1 ratio of 6.12, which maximizes the T1 contrast effect. ESIONs were tested using in vivo MRI. After tail vein injection of ESION (2.5 mg Fe/kg), blood vessels were brightened on the T1 weighted MR images, confirming that ESIONs can enhance T1 relaxation and be used as a T1 MRI contrast agent. The iron oxide core of this prototype nanoparticle contrast agent was coated with polyethylene glycol (PEG) [30]. PEG is a common coating material which is used to prevent nanoparticle fouling in blood by reducing protein binding and used to prolong circulation times by reducing clearance by the reticuloendothelial system (RES) [31]. To minimize the size of the

4

contrast agent and acquire T1 contrast, the extremely small iron oxide nanoparticles was incorporated as part of this brain MRI molecular contrast agent.

1.2   Blood Brain Barrier

The blood-brain barrier (BBB) represents a significant obstacle in delivering diagnostic and therapeutic agents to the central nervous system (CNS), preventing uptake of more than 98% of potential neurotherapeutics to brain [32-35]. BBB crossing based on receptor mediated transcytosis (RMT) is potentially especially promising. The use of protein shuttles has the potential to facilitate the transport of therapeutic agents across the BBB using specific endogenous receptor systems. Candidate receptor systems including transferrin receptors (TfR), low-density lipoprotein receptors, insulin receptors and neuropeptide receptors are highly expressed on the BBB where they mediate receptor-mediated transcytosis [34]. Among the different receptors, TfR has been widely used for transporting macromolecules across the BBB [36, 37]. Jefferies et al. identified a monoclonal antibody OX-26 specific for transferrin receptors [38]. This antibody was tested and was confirmed to be able to facilitate TfR-mediated transcytosis across BBB [39]. Yu et al. generated a bispecific antibody that binds to TfR for transcytosis and also to the enzyme β-secretase for inhibiting Aβ production[40]. However, the existing anti-TfR antibodies have relatively large size, especially when conjugated to additional components for RMT or other payloads such as imaging contrast agents. Also, it is expensive to engineer and synthesize monoclonal antibodies, which are typically produced in mammalian cell culture. There is an unmet need for smaller, less expensive, and easier to engineer system for BBB transcytosis.

1.3 Neurotensin

Current methods to evaluate BBB crossing require substantial resources and can be time-consuming [40, 41]. An efficient way to screen for BBB crossing in vivo would be helpful since in vitro models may not be fully predictive of in vivo results. Neurotensin is a 13 amino acid peptide first identified by Carraway and Leeman in 1973 from bovine hypothalamic extracts [42]. NT is expressed in CNS as well as in peripheral tissues, mostly in the gastrointestinal tract. NT is involved in regulating appetite, nociception, and thermoregulation in the CNS, and alters nutrient absorption, gastrointestinal motility, and secretion in the peripheral gastrointestinal tract [43]. It was found that NT induces rapid and transient hypothermia in mice and rats when injected to CNS [44, 45]. Meanwhile, intravenously injected NT does not typically cause hypothermia [46]. On the other hand, when NT-conjugated mouse TfR (mTfR)-binding VHHs were injected intravenously to mice, the NT-mTfR VHH conjugates induced hypothermia in mice, presumably because they get across the BBB and bind to NT receptors in hypothalamus [41, 47]. These properties of the NT system make it an apparently attractive assay platform for rapid testing of VHH BBB transcytosis.

1.4 Single domain Antibodies

Camelids produce functional antibodies devoid of light chains called heavy chain-only antibodies (HCAbs) [48, 49]. HCAbs recognize their cognate antigens by one single domain, the variable domain (VHH). The VHH in isolation is very small compared with other antibodies. The molecular weights of VHHs are typically ~15kDa, which is about 1/10 of the molecular weight of a conventional IgG and about half the molecular weight of a single chain variable fragment [49, 50]. Because of their small size, VHHs can also bind to epitopes not recognized by

conventional antibodies and can have better tissue penetration capacities [51, 52]. Despite of the small size, VHHs have affinities at the same order of magnitude as conventional IgGs, often in the nanomolar or subnanomolar range [53]. Importantly, VHHs have been found that can facilitate BBB penetration and allow brain target binding. The use of VHHs for BBB transcytosis and target engagement is promising. Specifically, Stanimirovic et al. identified an insulin-like growth factor 1 receptor binding VHH which crosses the BBB by receptor mediated transcytosis [54, 55]. Danis et al. identified and optimized VHHs to mitigate brain accumulation of pathological tau in a tauopathy mouse model [56]. Dupre et al., identified VHHs which could be used to detect tau in transgenic mice brain tissues [57]. However, the extent to which VHHs that engage in receptor mediated transcytosis using the TfR can carry diagnostic and therapeutic payloads across the BBB still has not been assessed. It is important to identify VHHs that bind to TfR and cross the BBB through RMT.

1.5 Pharmacokinetics

Pharmacokinetics (PK) is the study of drug absorption, distribution, metabolism and excretion [58]. Pharmacokinetic and biodistribution characteristics are important parameters to consider when designing and testing novel nanoparticles to achieve an appropriate level of nanoparticles in the target tissue site. Nanoparticles with either extremely short or extremely long circulation time are generally considered non-optimal; nanoparticles with extremely short circulation time may not have enough time to penetrate target tissue sites, while nanoparticles with extremely long circulation time could cause off-target tissue toxicity and reduce signal-to-noise ratio due to background signal [59-62]. Thus, it is helpful to measure PK characteristics at an early phase in the project development so that this information can be used to optimize contrast agent design.

Chapter 2: Methods

2.1 Single domain antibody production and characterization

2.1.1 Immunization of llama with mouse transferrin receptor

A single adult male llama (Lama glama) was immunized under contract agreement through

Triple J Farms (Kent Laboratories, Bellingham, WA) following the method previously

described [63]. Briefly, subcutaneous injections of 100 µg ectodomain (Cys89-Phe763)

mTfR (50741-M07H, SinoBiological) were performed with protein emulsified with complete

Freund's adjuvant on day 0, followed by additional 100 µg immunizations emulsified with

incomplete Freund's adjuvant on days 14, 28, and 42. On day 49, peripheral blood was

drawn for peripheral blood mononuclear cell (PBMC) isolation. Triple J Farms operates

under established National Institutes of Health Office of Laboratory Animal Welfare

Assurance certification number A4335-01 and United States Department of Agriculture

registration number 91-R-0054.

2.1.2 Generation of VHH immune phage display library

The generation of an immune phage display library and isolation of mTfR binding VHH

clones was performed using the methods previously described [63]. Briefly, total RNA

extracted from PBMCs was used for synthesis of first-strand complimentary DNA (cDNA)

using the SuperScript IV First-Strand Synthesis kit (#1891050, Invitrogen). The heavy-chain

variable domain was then amplified from the cDNA using Q5 high-fidelity DNA polymerase

(New England Biolabs) with the described primers (CALL001: 5′-

GTCCTGGCTGCTCTTCTACAAGG-3′ and CALL002: 5′-

GGTACGTGCTGTTGAACTGTTCC-3'). The heavy-chain specific amplicon was isolated

using electrophoresis with low-melting point agarose extraction with the QIAquick Gel

Extraction kit (Qiagen). A secondary amplification was performed using a modification of

the primers (VHH-Esp-For: 5′-

CCGGCCATGGCTGATGTGCAGCTGCAGGAGTCTGGRGGAGG-3′ and VHH-Esp-

Rev: 5′-GTGCGGCCGCTGAGGAGACGGTGACCTGGG T-3′) used by Pardon et al. to

facilitate cloning into the phagemid pHEN2 [64]. The amplified sequences were cleaved

with the restriction endonucleases NcoI and NotI (New England Biolabs) and subsequently

ligated into compatibly cleaved pHEN2 phagemid at a 3:1 (insert:phagemid) ratio overnight

at 16□C followed by purification. The resulting ligation mixture was electroporated into TG-

1 phage-display competent cells (#60502-1, Lucigen) and plated onto 2xYT agar containing

100 µg/mL carbenicillin and 2% (w/v) glucose at 37°C overnight. The resulting library

contained > 107 independent clones. Phage was produced for screening using the M13KO7

helper phage (#18311019, Invitrogen) followed by precipitation by addition of one-fifth

volume 20% polyethylene glycol 6000 / 2.5 M sodium chloride solution on ice and

centrifugation to purify the phage particles.

2.1.3 Immunopanning and clone screening

Selection of mTfR specific VHH was performed using direct binding of phage to immobilize

mTfR. Standard radioimmunoassay (RIA) tubes were coated with 500 µL mTfR solution at 5

µg/mL in sodium carbonate buffer, pH 9.6 overnight at 4°C. The coating solution was

removed, and the RIA tube filled with a 2% (w/v) non-specific blocking solution (bovine

serum albumin or nonfat dry milk) in 1x Phosphate Buffered Saline (PBS). Amplified phage

(~1011 phage) was mixed with blocking solution to a final volume of 500 µL and then transferred into the RIA tube to allow for association at room temperature and 600 rpm mixing. The RIA tube was then washed 20 times with 1x PBS and then the bound phage eluted with 100 mM triethylamine solution for 20 mins. The eluted phage solution was neutralized with 1:10 volume 1 M Tris-HCl, pH 8.0. The eluted phage was amplified in TG-1 cells and a second round of immunopanning was performed.

Following the second round of immunopanning, individual colonies were selected and cultured in 96-well blocks containing 2xYT containing carbenicillin at 37°C with 300 rpm shaking for 4-6 hours. Expression of VHH was induced by addition of isopropyl-beta-D-thiogalactoside (IPTG) to a final concentration of 1 mM and incubation overnight at 37□C. The culture blocks were centrifuged to pellet the cells and frozen at -80°C for 1 hour following removal of the culture supernatant. The culture block was then equilibrated to room temperature and 500 µL 1xPBS added to each well followed by shaking at 1500 rpm to resuspend the cell pellets and allow for release of VHH from the cells. The culture block was centrifuged for 20 min at 2000xg. Nunc Maxisorp plates were coated with mTfR at 1 µg/mL as described above and blocked with 1% bovine serum albumin (BSA). The clarified VHH supernatants were incubated on the mTfR plates for 1 hour at room temperature. The assay plate was washed and peroxidase conjugated goat anti-alpaca VHH domain specific antibody (#128-035-232, Jackson ImmunoResearch) at 0.8 µg/mL was transferred to the plate and incubated for 1 hour at room temperature. Following a final wash, the assay was developed by addition of tetramethylbenzidine (#T5569, Sigma-Aldrich) and absorbance was measured at 650 nm on a Biotek Synergy 2 plate reader. Clones with absorbance values greater than two standard deviations above background were considered of interest and subsequently

sequenced.

2.1.4 Amyloid beta specific VHH production.

Paraschiv et al. previously reported the isolation of amyloid beta binding VHH clones [65].

We selected the sequence for the named Nb3 clone for use in this study. The Nb3 amino acid

sequence was imported into SnapGene software (GSL Biotech LLC) and reverse translation

performed using preferred codon usage for expression in E. coli. Additional sequence,

including a (Gly-Gly-Gly-Ser)₃ between VHH domains, was incorporated for cloning into

pHEN2 as a tandem dimer as part of the heterotrimer clones synthesized with TfR binders.

To reduce the potential for recombination events, the DNA sequence was manually curated

to adjust the codon usage and reduce the frequency of repetitive sequence within the Nb3-

Nb3 dimer. The affinity of the Nb3-Nb3 dimer was measured using bio-layer intergerometry

as described below.

2.1.5 Bio-layer interferometry (BLI) assessment of VHH binding kinetics.

The binding kinetics of the selected VHH clone against mTfR and Aβ was assessed by BLI.

For measurements of mTfR kinetics, biotinylated VHH was diluted into assay buffer at 1

µg/mL and immobilized onto streptavidin coated biosensors (#18-5019, Sartorius) to a

minimum response value of 1 nm on the Octet Red96 System (Sartorius). For measurements

of amyloid beta, beta-amyloid(1-40)-Lys(biotin-LC) (AS-23517, Anaspec), was diluted into

assay buffer at 1 µg/mL and immobilized onto streptavidin coated biosensors (#18-5019,

Sartorius) to a minimum response value of 1 nm on the Octet Red96 System (Sartorius).

Purified mTfR or VHH clones were diluted into assay buffer at the specified concentrations.

The immobilized antigen biosensors were allowed to associate at 37°C followed by

dissociation in the baseline buffer well location. All assays included a background correction

condition to allow for sensor normalization. The ForteBio Data Analysis suite was used to normalize the association curves following background subtraction and Savitzky-Golay filtering. Curve fitting was applied using global fitting of the sensor data and a steady state analysis calculated to determine the association and dissociation constants. All assay steps were prepared in Greiner 96-well plates (#655209) in a volume of 300 µL. Assay buffer was defined as 0.1% BSA (w/v) in 1xPBS.

2.1.6 Synthesis and expression of VHH constructs.

Based on the methods described in **Immunopanning and clone screening** and **BLI assessment of VHH binding kinetics** sections, several neurotensin-fused VHH monomers with different binding affinities to mouse transferrin receptor were synthesized for VHH screening study. These constructs were termed "M1$_{WT}$-NT", "M1$_{P96H}$-NT", "M1$_{AA}$-NT", "M1$_{R100dH}$-NT". In addition, VHH monomers of a Nb3; a single polypeptide VHH heterotrimer that consisted of NB3, a (GGGS)$_3$ linker, NB3, a (GGGS)$_3$ linker, and H1; and a single polypeptide VHH heterotrimers that consisted of M1$_{P96H}$, a (Gly-Gly-Gly-Ser)$_3$ linker, Nb3, a (Gly-Gly-Gly-Ser)$_3$ linker, and Nb3; were produced using the method described in **Amyloid beta specific VHH production**. These constructs were termed "VHH singlet", "VHH triplet", and "M1$_{P96H}$-triplet". The VHH naming convention for P96H and R100dH are based on the Kabat nomenclature and refer to the specific amino acid residue modification positions within the VHH sequence [66]. Another neurotensin fusion with a VHH generated against human TfR, which does not bind mouse TfR called "H1-NT," was used as control. All VHH constructs were designed using SnapGene Software and synthesized (Twist Bioscience) with corresponding restriction endonuclease sites for direct cloning into pHEN2. Sequence confirmed pHEN2 clones with the various constructs were

transferred into BL21(DE3) competent E. coli cells (C2527I, New England Biolabs). Transformed cells were grown in terrific broth medium containing carbenicillin at 37°C and 300rpm shaking in baffled flasks. Once the culture density reached an optical density equal to 0.6, IPTG was added to a final concentration of 1mM to induce protein expression. For monomer VHH expression the post-induction incubation temperature was maintained at 37°C but reduced to 30°C for the $_{M1P96H}$-triplet. Following overnight expression, cells were pelleted by centrifugation and VHHs were extracted through osmotic shock and recovery of the periplasmic fraction [63, 67]. Clarified periplasmic fraction was purified using HisPur™ Ni-NTA Resin (88222, Thermo Fisher Scientific) column chromatography. The eluted VHH proteins were further purified by size-exclusion chromatography (SEC) over a Superdex75 10/300 column on an AKTA Pure (Cytiva). Protein purity was assessed by SDS-PAGE on a 10% Bis-Tris MES acrylamide gel and found to be >95% pure.

$M1_{P96H}$-triplets and H1-triplets were fluorescently labeled with using Alexa Fluor™ 647 succinimidyl ester dye by incubating with the succinimidyl ester dye for 1 hour in 50mM sodium carbonate buffer, pH 9.6 followed by purification with a 5mL HiTrap desalting column in-line with the AKTA Pure. The fluorescence dye labeled $M1_{P96H}$-triplet and H1-triplet were named "$M1_{P96H}$-triplet-647" and "H1-triplet-647"

VHH singlet and VHH triplet were labeled with a NIR dye called FNIR-Tag-NHS provided by the Schnermann group [68]. Lysine groups on VHHs were labeled with FNIR dye through standard NHS conjugation. For conjugation of FNIR dye to VHH, a 1:1.5 molar ratio of VHH and FNIR dye were incubated together at room temperature for 2h. Following conjugation, the VHH-dye conjugate was purified from unincorporated label using a 5mL HiTrap® desalting column.

Total protein concentration was measured using the Epoch microplate spectrophotometer (BioTek®) by measuring absorption at wavelength 280 nm and corrected using the theoretical extinction coefficient.

2.1.7 Production of IONPs, ligand exchange, and conjugation of VHH constructs

IONPs were generated by the thermal decomposition and ligand exchanged methods described by Kim, et al. [18]. Two different approaches to ligand exchange were used, involving 1) PEG-Azide-2k, MW 2000 Da (Nanosoft Polymers) and 2) a 1:1 ratio of PEG-Azide-2k and PEG methyl ether, MW 750Da (Sigma Aldrich). We developed two types of NPs. The first one was IONP$_{PEG2000}$, which contained only PEG-Azide (MW 2000Da) on the surface while the second type IONP$_{PEG2000/750}$ comprised of both PEG-Azide (MW 2000Da) and methoxy-PEG-ether (MW 750Da). Solid state IONP$_{PEG2000}$ and IONP$_{PEG2000/750}$ were dissolved in 0.9% saline + 0.05% tween 80 solution and sonicated for 15 min followed by filtration through a 0.22 µm syringe filter. Then, a Superose™ 6 Increase 10/300 column (Cytiva) was used for size exclusion chromatography (SEC). Fractions corresponding to the eluted peak were collected. Hydrodynamic size of IONP were measured using the Dynapro® Nanostar® cuvette-based Dynamic light scattering (DLS) instrument. FNIR dye and Dibenzocyclooctyne-amine (DBCO) were conjugated to VHH triplets at 1:1.5 molar ratio through standard NHS conjugation as described in **synthesis and expression of VHH constructs**. Peak fractions of IONPs were concentrated and conjugated with FNIR dye and DBCO labelled VHH triplets via copper-free click chemistry for 24hr at room temperature [69, 70].

The click chemistry allowed reaction of DBCO conjugated VHH triplets to the azide groups

at the terminus of the PEG2000, yielding covalent attachment of VHH triplet-DBCO to PEG-Azide-2k ligand coated IONPs. After 24hr incubation, the click-reaction was resolved through a Superose 6 Increase column for size exclusion separation of unreacted constituents. Fractions at the peak of size exclusion were collected and their size was measured using DLS. The peak fractions corresponding to VHH conjugated IONP were used for in vivo pharmacokinetic studies.

2.1.8 Endotoxin removal

Removal of contaminating endotoxin was achieved using High-Capacity Endotoxin Removal Resin (88270, Pierce) from the VHH preparations. A volume of 0.25ml endotoxin removal resin was added to 1ml of VHH sample. The VHH and resin were mixed for 2hr at room temperature to allow for absorption of endotoxin. The mixture was centrifuged to pellet the resin and the supernatant collected. A volume of 0.25ml fresh endotoxin removal resin was added to the first-pass solution and mixed for another 2hr at room temperature. Following a final centrifugation to pellet the resin, the solution was collected for endotoxin level testing. Endotoxin levels were measured using the Chromagenic Endotoxin Quant kit (A39552, Pierce) according to the manufacturers protocol to ensure a level of endotoxin <0.5 endotoxin units/mg of total protein.

2.1.9 Binding assessment of histidine mutations by ELISA

To determine the effect on histidine mutation introduction, an ELISA was performed with the post VHH binding wash buffer at normal and reduced pH. Nunc Maxisorp plates were coated with mTfR at 1 µg/mL in 50mM sodium carbonate, pH 9.6 overnight at 4°C. The plates were blocked with 1% BSA in 1xPBS buffer and then triplicate dilutions of each VHH prepared in 0.5% BSA in 1xPBS buffer and transferred to the plate. Binding at room

temperature for 2 hours was followed by three cycles of 5-minute washes with either 1xPBS, pH 7.2 or 1xPBS, pH 5.5. Following the pH dependent wash step, the bound VHH was detected with peroxidase conjugated goat anti-alpaca VHH domain specific antibody (#128-035-232, Jackson ImmunoResearch) at 0.8 µg/mL incubated for 1 hour at room temperature. Following a final wash, the assay was developed by addition of tetramethylbenzidine (#T5569, Sigma-Aldrich), the reaction was terminated by addition of 50 µL 1M hydrochloric acid and absorbance was measured at 450 nm on a Biotek Synergy 2 plate reader.

2.2   Animals

All animal experiments were conducted under protocols approved by the National Institute of Neurological Disorders and Stroke (NINDS)/ National Institute on Deafness and Other Communication Disorders (NIDCD) Animal Care and Use Committee in the National Institutes of Health (NIH) Clinical Center. C57BL/6J female mice were purchased from Jackson labs at 6-7 weeks of age and used at 7-12 weeks of age. APP_{SWE}/PSEN1dE9 (MMRRC Strain #034832) positive transgenic mice were purchased from Jackson labs [71, 72], maintained on a hybrid (C57BL/6xC3H) background.

The dark color fur coat of the strain of mouse used impedes the penetration of NIR light; therefore, the fur overlaying the regions of interest was removed by applying a topical depilatory cream above the head, on the ventral and dorsal torso and tail of the mice one day prior to IV injection. Delayed skin hyperpigmentation was observed starting 4 days after hair removal.

Anesthetized mice were injected via tail vein with VHHs, VHH-NT fusions and IONP-VHH conjugates. Experiments were performed at the same time each day.

2.3   Intravenous Injection

Mice were anesthetized with 60% oxygen/ 40% medical air gas mixture containing 5% isoflurane in an induction box. After a stable anesthesia plane was established, mice were maintained at 1.5-2% isoflurane level. Artificial tears ointment was applied to prevent eye injury due to drying. Mice were placed on an electrical heating pad to maintain body temperature at 37C°. The VHHs, VHH-NTs and IONP-VHHs were injected to mice through the tail vein using a 30 Gauge needle in a single bolus Mice were maintained under anesthesia for approximately 2-3 minutes. Following the procedure, the mice were allowed to recover on a heating pad until fully ambulatory and then returned to their home cage with immediate access to food and water.

2.4   Temperature measurement

Infrared thermometry was used for temperature measurement using an infrared thermometer (Model# 62 MAX+, Fluke). Abdominal fur was removed by application of topical depilatory cream prior to temperature measurement for precise data collection. Baseline temperature was measured three times before IV injection with a time interval of 30min between measurements. Then, mouse temperatures were measured at the time intervals of 30min, 1hr, 1.5hr, 2hr, 2.5hr, 3hr, 3.5hr, 4hr, 4.5hr and 5hr after injection. All temperature measurements were performed by investigators blinded to the identity of the injected VHH sample. Mice were briefly anesthetized (<20 seconds) with isoflurane for each temperature measurement. In preliminary experiments we confirmed that this brief anesthesia did not affect temperature.

2.5   Imaging and Image Analysis Method

2.5.1 NIR imaging methods

Mice were anesthetized with 60% oxygen/40% medical air gas mixture with 5% isoflurane for induction of anesthesia and 1.5% isoflurane level for maintenance. Mice were imaged using the Pearl Trilogy Near-Infrared Fluorescent and Bioluminescent small animal imaging system (Licor, Nebraska, USA). The specific parameters for NIR imaging were resolution = 170um, fluorescence channel at 800nm (excitation at 785 nm and emission at 820 nm) for FNIR dye. NIR images were collected before and at time 2min, 1hr, 2hr, 4hr, 8hr, 1day, 2days post IV injection using Pearl. After end-point imaging, mice were euthanized by transcardial perfusion using 1X phosphate-buffered saline with heparin under 5% isoflurane.

2.5.2 NIR Image and Data Processing

Equally sized regions of interest (ROI)s were manually drawn using the software Image Studio (ver 5.2) from Li-Cor. Head and right kidney ROIs were drawn from the prone view images while liver and front left paw ROIs were drawn from the supine view images. The average fluorescence intensity of each ROI was calculated and generated by Image Studio (ver 5.2).

2.5.3 Confocal microscopy of mice brains injected with triplet-647

Two hours post IV injection mice were sacrificed under isoflurane anesthesia by cardiac perfusion with 1X PBS + Heparin (10 units Heparin per milliliter 1X PBS). Following perfusion, mice were decapitated using a pair of sharp surgical shears and the brain was carefully excised from the cranium. Brains were fixed in 4% PFA for 24hrs then equilibrated in 30% sucrose for 48 hours. Then, mouse brains were sectioned at 50 µm thickness using a freezing sliding microtome. Staining was performed to visualize amyloid plaques using the

Congo Red derivative X34.[73] Tissue was rinsed with 1xPBS two times. Then, tissues were incubated in 40%EtOH/60%PBS at pH10 containing 10 μM X34 (SML1954-5MG, Sigma) for 10min. After X34 incubation, tissue was rinsed with milliQ water five times then differentiated in 40%EtOH/60%PBS at pH10 for 2min. After differentiation, the tissue was rinsed with miliQ water for 10min then mounted onto positively charged slides (EF15978Z, Daigger®). The mounted tissue sections were allowed to dry overnight at room temperature and cover slipped using fluoromount-G (00-4958-02, Invitrogen™).

To objectively evaluate the effect of intravenous injection of M1$_{P96H}$-Triplet-647 and H1-Triplet-647 on APP/PS1 mice, brain sections at around 2.5mm posterior to bregma were selected for confocal fluorescence imaging. The brain sections were equally divided into 10 parts in both horizontal (x) and vertical (y) directions. X and y coordinates were randomly selected using by random numbers from 1 to 10. When (x, y) coordinates fell onto a cortical area, stacks of images were taken which covered 16μm depth (z direction) starting from the top of the brain section. When (x, y) coordinates fell outside of the cortex, the microscope was moved to the next randomized (x, y) coordinates without taking images. Brain sections were imaged using a Zeiss LSM 510 microscope. Stacks of images were acquired with eight images per stack and 2μm optical thickness at 20x magnification using a Zeiss Plan-Apochromat 20x/0.8NA lens. Images were acquired using laser wavelength at 633nm to visualize the VHH triplets conjugated with 647 dye and 405 nm wavelength laser to visualize the X-34 dye. For 647 channel images, laser at wavelength 633nm was used with a LP650 filter and laser power set to be at transmission 100%. For X34 channel images, laser at wavelength 405nm was used with a BP420-480 filter and laser power set to be at transmission 15%. The images were exported in lsm file format for image analysis using

ImageJ.

2.5.4 Fluorescent confocal microscopy - Naïve brain as controls

Naïve APP/PS1 positive mouse brain sections stained only with X-34 for fluorescence confocal microscopy were used as a negative control. Naïve APP/PS1 positive mouse brain sections stained with both X34 and ex vivo $M1_{P96H}$-Triplet-647 for fluorescence confocal microscopy were used as a positive control. For ex vivo $M1P96H$-Triplet-647 staining, naïve brains were sectioned and washed in 1XPBS. Sections were incubated in 3% normal donkey serum for 30min to block non-specific binding. After blocking, tissue sections were incubated overnight at 4C° in $M1_{P96H}$-Triplet-647 at a concentration of 10ug/ml in blocking solution. Tissues were then washed in 1xPBS three times followed by X34 staining as described.

2.5.5 Automated image analysis

To quantitatively analyze the confocal microscope images, thresholding and particle analysis were performed to remove background signals and isolate target structures of interest. The percent area of X34 stained amyloid plaques was quantified with thresholding at (0, 30) followed by Particle analysis. To remove low signal background, 647 channel image thresholding was set at 0-1000. Then the 647 channel images was analyzed with particle analysis. The parameters for particle analysis were set to be 0-1000 pixels for size and 0.1-1.0 for circularity. The parameters for thresholding and particle analysis were determined through testing of different parameters to capture the qualitative morphology of amyloid plaques as assessed by experienced investigators. Amyloid plaque levels were represented as % area of X34 coverage and VHH triplet-647 entry into the brain parenchyma was represented as % area of Alexa 647 dye coverage in the areas with X34 staining. Because

there is mouse-to-mouse variability in plaque size and X34 staining intensity, we analyzed the ratio of the Triplet-647 coverage to X34 coverage.

2.6 Statistical analysis

Unpaired student t-test were performed to evaluate the differences between the transcytosis ability of $M1_{P96H}$-triplet-647 and H1-triplet-647 to amyloid plaques in APP/PS1 transgenic mice brains. Graphs were created using Prism. Sample sizes were based on availability of transgenic mice and previous experiments. No formal power calculations were performed.

2.7 Mathematical modeling

Mathematical models were built using MATLAB (The Mathworks, Inc.) to predict distribution and pharmacokinetics based on nanoparticle size. The mathematical models were built based on kinetic data from VHH singlet, VHH triplet, $IONP_{PEG2000}$ VHH triplet, and $IONP_{PEG2000/750}$ VHH triplet data. Model fitting was done by minimization of the residual sum of squares across all five compartments and the blood clearance rate using the particle swarm algorithm [74, 75]. r^2 values were calculated to evaluate the goodness of fit. This model consists of 5 compartments: compartment 1 is the blood compartment, with a single bolus input and exchange of nanoparticles/VHHs with compartment 2 (kidney compartment), compartment 3 (liver compartment), and compartment 4 (head 1 compartment). Compartment 4 also exchanges with compartment 5 (head 2 compartment). In this model, the two main paths for clearance are the kidney and liver compartments. Kidneys and liver are the two main organs which are responsible for nanoparticle elimination [76]. The intake and clearance of nanoparticles from blood to kidneys/liver are the main characteristics that differentiate the in vivo kinetics of different nanoparticles and VHHs.

The signal from spleen was not analyzed because of low signal strength. This 5-compartment model was modified based on a 4-compartment model with blood, liver and kidney compartment as well but only one head compartment. Based on small sample corrected Akaike information criterion (AICc) value [77] and model fitting, the 5-compartment model was selected over the 4-compartment model. Two compartments were used to better describe the nanoparticles/VHHs in vivo distribution and kinetics in head to guide the timing of future brain MRI studies.

Chapter 3: Pharmacokinetics of Single Domain Antibodies and Conjugated Nanoparticles Using a Hybrid Near Infrared Method

3.1 Abstract

Iron oxide nanoparticles and single domain antibodies from camelids (VHHs) have been

increasingly recognized for their potential uses for medical diagnosis and treatment. However,

there have been relatively few detailed characterizations of their pharmacokinetics (PK). The

aim of this study was to develop imaging methods and pharmacokinetic models to aid the

future development of a novel family of brain MRI molecular contrast agents. An efficient

near-infrared (NIR) imaging method was established to monitor VHH and VHH conjugated

nanoparticle kinetics in mice using a hybrid approach: kinetics in blood were assessed by

direct sampling, and kinetics in kidney, liver, and brain were assessed by serial in vivo NIR

imaging. These studies were performed under "basal" circumstances in which the VHH

constructs and VHH-conjugated nanoparticles do not substantially interact with targets nor

cross the blood brain barrier. Using this approach, we constructed a five-compartment PK

model that fits the data well for single VHHs, engineered VHH trimers, and iron oxide

nanoparticles conjugated to VHH trimers. The establishment of the feasibility of these methods

lays a foundation for future PK studies of candidate brain MRI molecular contrast agents.

3.2 Introduction

Neurological disorders affect millions of people worldwide, but at present our ability to assess

these disorders objectively and quantitatively is limited [1]. Improvements in the assessment of neurological disorders would allow for disease progression monitoring and provide direct assessment of candidate therapeutics [2-5]. The long-term goal of this project is to develop MRI molecular contrast agents which will cross the blood brain barrier (BBB) and label relevant extracellular and intracellular biomarkers in the brain parenchyma. In the process of discovering and optimizing necessary components of these contrast agents, we have synthesized nanoparticles which consist of an iron oxide nanoparticle (IONP) core conjugated with Polyethylene glycol (PEG) plus camelid VHH antibody fragments for specific targeting.

IONPs have been widely used for medical applications including cancer diagnosis and treatment [15, 16], treatment of iron deficiency anemia [15], enhanced blood pool and tumor MRI imaging [17, 18], MRI molecular imaging [19-22] and magnetic resonance angiography (MRA) [23]. Sillerud et al. synthesized a novel MRI contrast agent by conjugating superparamagnetic oxide nanoparticles (SPIONs) with anti-amyloid-beta precursor protein (AβPP) antibodies to specifically target amyloid-beta plaques [24]. Iron oxide nanoparticles have also been functionalized with single-chain antibodies (scFv) against activated platelets for T1 and T2- weighted MRI of thrombi [19]. IONPs are considered relatively safe and do not induce cytotoxicity below 100 μg/ml in vitro [25]. MRI Molecular contrast agents based on iron oxide nanoparticles have good biocompatibility, at least in part because human blood and tissues are naturally rich in iron [26, 27]. The FDA has approved an IONP, Ferumoxytol, for treatment of iron-deficiency anemia in patients with chronic kidney disease [28]. Ferumoxytol is also used off-label as a contrast agent for MR angiography in patients with impaired renal function as well [29] and no major safety concerns have been reported. In a widely cited publication, Kim et al [18] demonstrated that homogenous size iron oxide nanoparticle cores

for MR imaging could be synthesized at large scales. Their extremely small 3nm iron oxide nanoparticles (ESIONs) were shown to have a high r1 relaxivity of 4.78 mM-1s-1 at 3T and low r2/r1 ratio of 6.12, which maximizes the T1 contrast effect. ESIONs were tested using in vivo MRI. After tail vein injection of ESION (2.5 mg Fe/kg), blood vessels were brightened on the T1 weighted MR images, confirming that ESIONs can enhance T1 relaxation and be used as a T1 MRI contrast agent. The iron oxide core of this prototype nanoparticle contrast agent was coated with PEG [30]. PEG is a common coating material which is used to prevent nanoparticle fouling in blood by reducing protein binding, and used to prolong circulation times by reducing clearance by the reticuloendothelial system (RES) [31].

Camelids, which include llamas, alpacas, and camels, produce functional antibodies devoid of light chains called heavy chain-only antibodies (HCAbs) [63, 64]. The heavy chain of this kind of antibody is folded into three domains: the N-terminal domain that is variable in sequence, followed by a hinge region and two constant domains. HCAbs recognize their cognate antigen by one single domain, the VHH. VHHs have a very small size compared to other antibodies or functional antibody fragments. The molecular weight of a VHH is approximately 15kDa, which is around 1/10 of a conventional IgG's molecular weight, and about 50% of that of a single chain variable fragment (ScFv) [49, 50]. VHHs have been used for in vivo imaging and therapeutics [49, 50]. For example, Li et al. labeled anti-Aβ42 and anti-Tau VHHs with Alexa488 fluorescent dye and visualized extracellular Aβ and intracellular neurofibrillary tangles using 2-photon-microscopy [65]. Vandesquille et al. conjugated a VHH (R3VQ) targeting Aß with gadolinium to allow MRI detection of Aβ in post-mortem mouse brain [66]. Rincon et al. used VHHs to lower Aβ levels with AAV-based delivery of anti-BACE1 VHH into the CNS of a cerebral amyloidosis mouse model [67]. VHHs against SARS-CoV-2 which

25

could bind spike protein receptor binding domain have been recently developed as potential therapeutics for coronavirus outbreaks [68-71]. A humanized divalent VHH targeting von Willebrand factor (Caplacizumab) has been recently approved by the FDA for treatment of acquired thrombotic thrombocytopenic purpura [72, 73]. Importantly, VHHs show low immunogenicity risk profile before humanization [74]. For human therapeutic purposes, VHHs have been humanized to further lower the risk of immunogenicity [75]. For example, the safety of Caplacizumab has generally been good [76].

Pharmacokinetics (PK) is the study of drug absorption, distribution, metabolism and excretion [58]. Pharmacokinetic and biodistribution characteristics are important parameters to consider when designing and testing novel nanoparticles to achieve an appropriate level of nanoparticles in the target tissue site. Nanoparticles with either extremely short or extremely long circulation time are generally considered non-optimal; nanoparticles with extremely short circulation time may not have enough time to penetrate target tissue sites, while nanoparticles with extremely long circulation time could cause off-target tissue toxicity and reduce signal-to-noise ratio due to background signal [59-62]. Thus, it is helpful to measure PK characteristics at an early phase in the project development so that this information can be used to optimize nanoparticle design.

Multiple approaches have been used to acquire PK and biodistribution data from in vivo experiments. Plasma and tissue sampling followed by inductively coupled plasma mass spectrometry (ICP-MS) are often used for in vivo distribution and PK studies. In prominent examples of this approach, Lankveld et al. assessed silver nanoparticles using ICP-MS to determine the silver content in organs for their tissue distribution study [77]. Xue et al. also used ICP-MS to study the tissue distribution of iron oxide nanoparticles in mice [78]. This

approach, however, is invasive and requires sacrificing animals at multiple time points which introduces inter-animal variations in data. Instead, various non-invasive imaging methods including PET, SPECT/CT, and MRI have been used to help trace distribution and clearance patterns [79-81]. While MRI may be an imaging modality of choice for diagnostic studies, it is expensive, requires lengthy anesthesia times for animals, and has relatively poor time resolution for use in PK studies. PET and SPECT are also relatively expensive imaging methods and raise radiation safety concerns. Near infrared (NIR) imaging has been proposed as an alternative method to study pharmacokinetics and tissue distribution to facilitate nanoparticle development [59]. Compared with the aforementioned methods, NIR is a less expensive, faster and safer method which can be used to investigate nanoparticles' in vivo behavior in appropriate small animal models[59]. Compartment models have been widely used for oncology, disease diagnosis and imaging studies [82, 83]. This paper combined near infrared imaging and multi-compartment model to study the pharmacokinetics of VHHs and IONPs in vivo.

This study establishes a foundation to understand the PK of VHHs and IONPs. In this study, IONPs conjugated to VHHs and labeled with a NIR fluorescent dye were injected intravenously into mice. The PK of VHHs alone and VHH conjugated IONPs were monitored using a high resolution NIR scanner. Fluorescence signal change in mouse head, kidney, and liver were imaged over a period of two days post injection to qualitatively and quantitatively understand the PK of our nanoparticles. A five compartment PK model was constructed to describe the relationship between in vivo PK and hydrodynamic size following single bolus IV injection. It was found that increasing VHH and nanoparticle size results in a switch from kidney dominant clearance to liver dominant clearance, which is consistent with past findings.

The use of mathematical PK models provides a quantitative method to study the relationship between PK parameters and nanoparticle/VHH sizes and can be used to explore the in vivo pharmacokinetics and distribution of other VHHs and nanoparticles for future studies. This PK model will be incorporated and modified for describing novel VHH-IONP in vivo PK characteristics during ongoing development of future brain MRI molecular contrast agents.

3.3   Materials and Methods

3.3.1   Synthesis of VHH

For this study, we synthesized VHH monomers of a nanobody called NB3 that did not bind any targets in wild-type mice using methods similar to those described in Esparza. et al [68]. In addition, we produced a single polypeptide VHH heterotrimer that consisted of NB3, a (GGGS)$_3$ linker, NB3, a (GGGS)$_3$ linker, and another nanobody called H1 synthesized by Esparza et al. that also does not bind any targets in wild-type mice. The sequence and characteristics of these VHH constructs will be reported separately. These constructs were termed "VHH singlet" and "VHH triplet." Phagemid pHEN2 with VHH triplet or VHH singlet were transferred into the BL21(DE3) competent E. coli cells (C2527I, New England BioLabs) (Figure 3.1). The competent cells were grown in terrific broth medium at 37°C. Isopropyl β-d-1-thiogalactopyranoside (IPTG) at a final 1mM concentration was added to induce VHH expression when the OD600 reached 0.6. Following overnight expression, cells were pelleted by centrifugation and VHHs were extracted through periplasm extraction [68, 84]. The 6xhistidine tagged VHHs were purified by Fast Protein Liquid Chromatography (FPLC) using a HisTrap™ FF Ni-NTA column (Cytiva). To further purify VHHs, they were size fractionated using a Superdex™ 75 10/300 GL column (Cytiva) with Phosphate Buffered Saline (PBS), pH

7.4 at flow rate of 1ml/min.
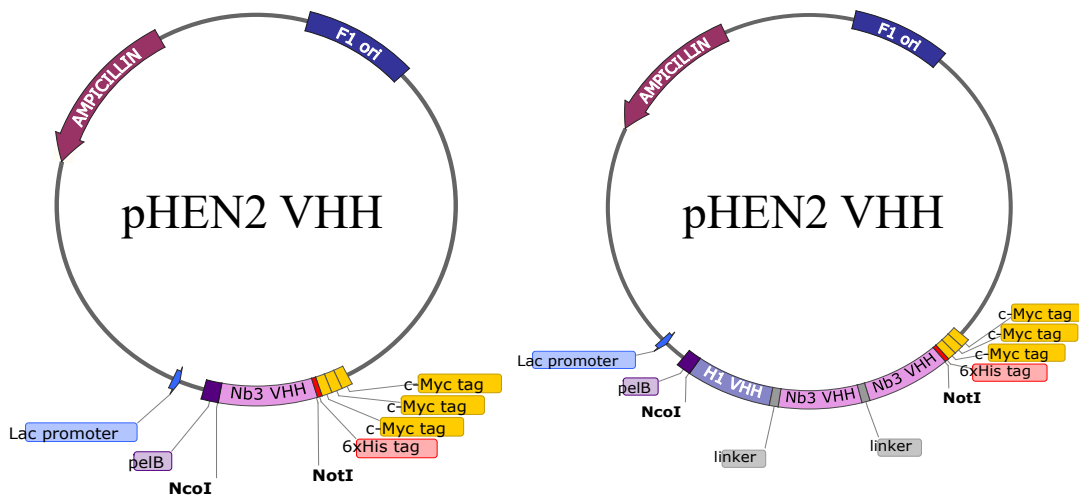
Figure 3.1. Schematic representation of VHH singlet and VHH triplet in pHEN2 phagemid vector. VHH singlet and VHH triplet DNA constructs were inserted into the pHEN2 phagemid vector for protein expression. For VHH triplet, the individual VHHs were linked using $(GGGS)_3$ linkers. This figure was generated using SnapGene software (from Insightful Science; available at snapgene.com).

3.3.2 Conjugation of FNIR dye to VHH constructs

The NIR dye FNIR-Tag-NHS was provided by the Schnermann group [85]. Lysine groups on VHHs were labeled with FNIR dye through standard NHS conjugation. For conjugation of FNIR dye to VHH, a 1:1.5 molar ratio of VHH and FNIR dye were incubated together at room temperature for 2h. Following conjugation, the VHH-dye conjugate was purified from unincorporated label using a 5mL HiTrap® desalting column. Total protein concentration was measured using the Epoch microplate spectrophotometer (BioTek®) by measuring absorption at wavelength 280 nm and corrected using the theoretical extinction coefficient.

Production of IONPs, ligand exchange, and conjugation of VHH constructs
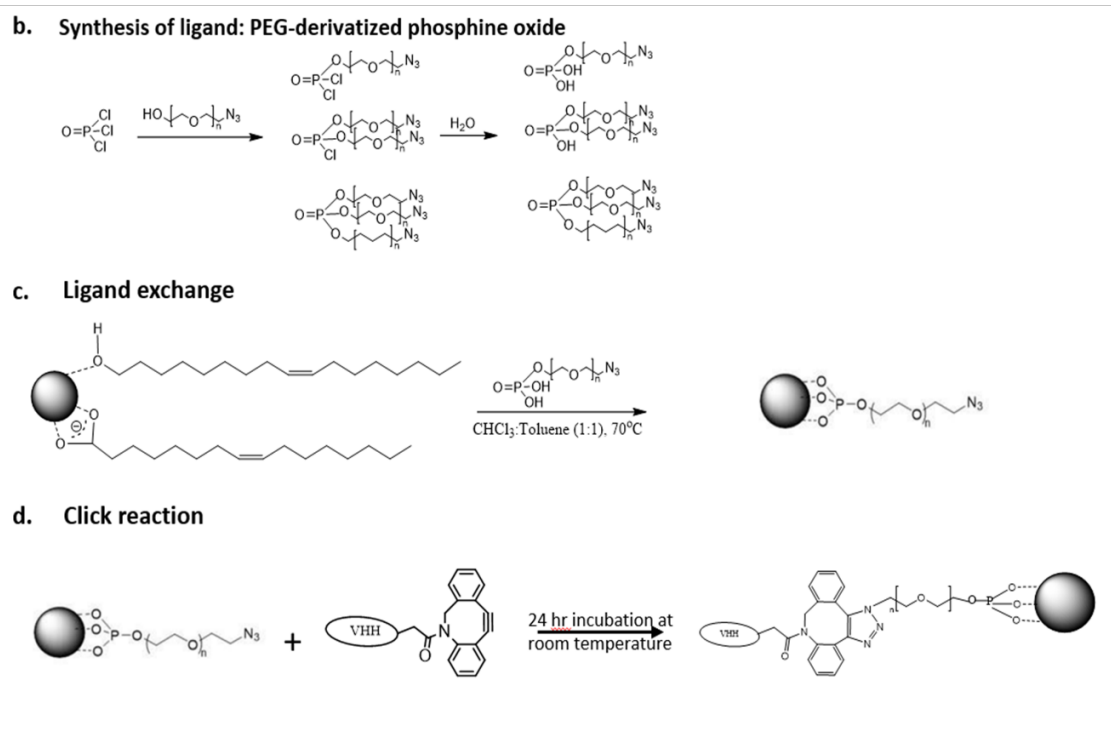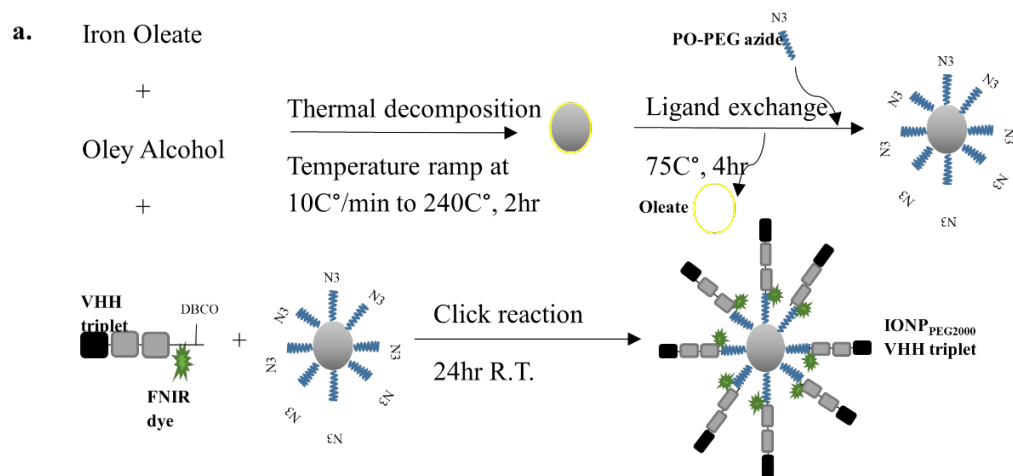
Figure 3.2. Synthesis of IONP$_{PEG2000}$ VHH triplet. a. IONP cores were produced through thermal decomposition, then ligand exchange was performed to coat IONP cores with PEG ligands. VHHs were labeled with FNIR dye and attached to ligand exchanged IONPs through click reaction with terminal azide (N3). b-d. Chemical reactions describing PO-PEG ligand synthesis, ligand exchange reaction which replaced oleic acid with PO-PEG ligands on the surface of the iron oxide core to make the IONP water soluble and click chemistry which conjugated VHH triplet to IONP. The ligand exchange and click reaction of di-substituted PO-PEG ligand and tri-substituted PO-PEG ligand are not shown here.

IONPs were generated by the thermal decomposition and ligand exchanged methods described

by Kim, et al. [18]. Briefly, iron oxide cores were synthesized by decomposition of iron oleate

in oleyl alcohol (Sigma Aldrich) and diphenyl ether (Sigma Aldrich) (Figure 3.2a). The iron

oxide cores were only soluble in organic solvents. To make the iron oxide cores water soluble,

PEG-derivatized phosphine oxide (PO-PEG) ligands were synthesized and exchanged with

oleic acid on the iron oxide core surface [30]. PO-PEG ligands were synthesized by mixing the

phosphoryl trichloride (POCl$_3$) with poly(ethylene glycol) methyl ether (mPEG) in anhydrous

dichloromethane modified based on Na et al. [30]. Then, ligand exchange was performed to

coat iron oxide cores with Poly(ethylene glycol) (PEG) resulting in IONPs soluble in aqueous

solutions (Figure 3.2c). Iron oxide core and the ligands were combined and dissolved in

toluene and chloroform (ACS grade) and the solution refluxed at 75°C for 4hr for the ligand

exchange reaction. When the reaction was complete, the solution was washed with

dichloromethane and hexane following centrifugation to remove unreacted substance. The

pellet contained IONP were dried under vacuum. IONPs were characterized using

Transmission Electron Microscopy (TEM) for core size measurement and infrared

spectroscopy (IR) was performed to confirm the success of ligand exchange by the presence of
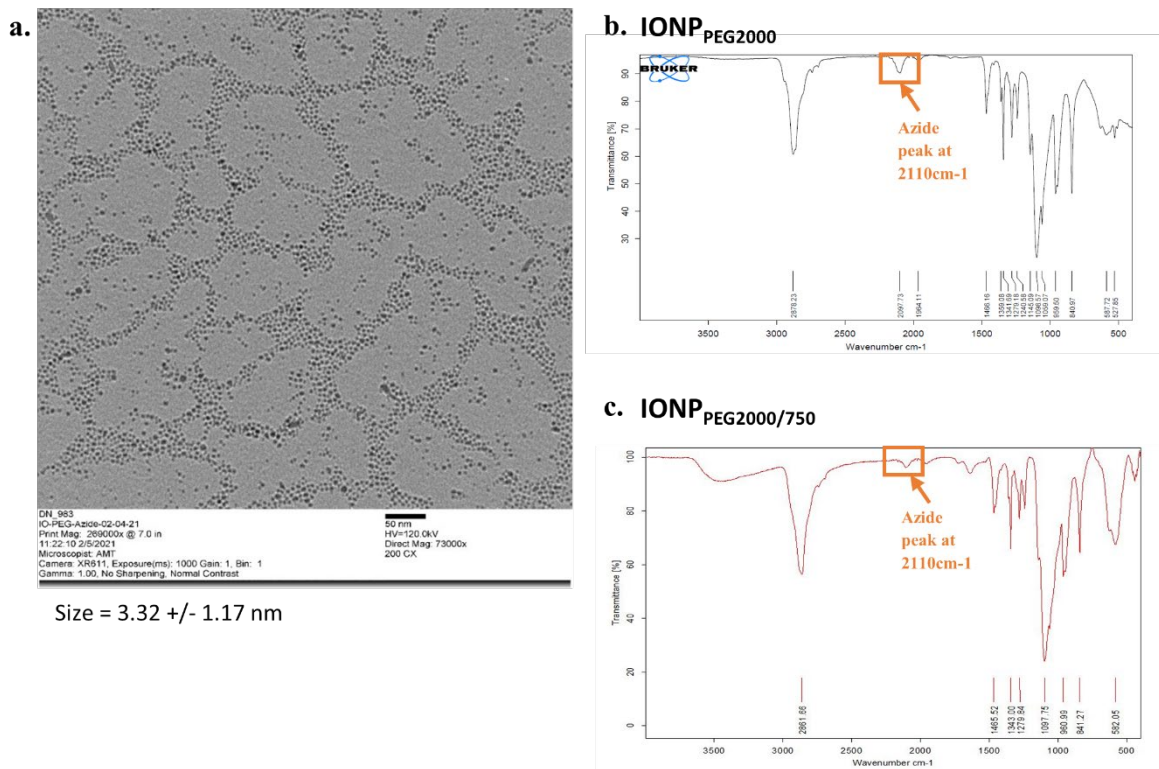
Figure 3.3. Characterization of IONPs. a. Transmission electron microscopy (TEM) image of a representative batch of iron oxide cores with diameter measured at 3.32 +/- 1.17nm. The iron oxide core size was quantified using ImageJ. b. IR measurement of a representative batch of IONP$_{PEG2000}$. Azide peaks at 2110cm-1 before conjugation to VHH triplet. After conjugation, the azide is destroyed, as in Figure S11d. c. IR measurement of a representative batch of IONP$_{PEG2000/750}$. Azide peaks at 2110cm-1 before conjugation to VHH triplet. After conjugation, the azide is destroyed, as in Figure 3.2d.

an azide specific spectral peak (Figure 3.3).

Two different approaches to ligand exchange were used, involving 1) PEG-Azide-2k, MW 2000 Da (Nanosoft Polymers) and 2) a 1:1 ratio of PEG-Azide-2k and PEG methyl ether, MW 750Da (Sigma Aldrich). We developed two types of NPs. The first one was IONP$_{PEG2000}$, which contained only PEG-Azide (MW 2000Da) on the surface while the second type IONP$_{PEG2000/750}$ comprised of both PEG-Azide (MW 2000Da) and methoxy-PEG-ether (MW

32

750Da). Solid state IONP$_{PEG2000}$ and IONPP$_{EG2000/750}$ were dissolved in 0.9% saline + 0.05% tween 80 solution and sonicated for 15 min followed by filtration through a 0.22 μm syringe filter. Then, a Superose™ 6 Increase 10/300 column (Cytiva) was used for size exclusion chromatography (SEC). Fractions corresponding to the eluted peak were collected. Hydrodynamic size of IONP were measured using the Dynapro® Nanostar® cuvette-based Dynamic light scattering (DLS) instrument. FNIR dye and Dibenzocyclooctyne-amine (DBCO) were conjugated to VHH triplets at 1:1.5 molar ratio through standard NHS conjugation as described in **Conjugation of FNIR dye to VHH constructs**. Peak fractions of IONPs were concentrated and conjugated with FNIR dye and DBCO labelled VHH triplets via copper-free click chemistry for 24hr at room temperature [86, 87].

The click chemistry allowed reaction of DBCO conjugated VHH triplets to the azide groups at the terminus of the PEG2000, yielding covalent attachment of VHH triplet-DBCO to PEG-Azide-2k ligand coated IONPs (Figure 3.2d). After 24hr incubation, the click-reaction was resolved through a Superose 6 Increase column for size exclusion separation of unreacted constituents. Fractions at the peak of size exclusion were collected and their size was measured using DLS. The peak fractions corresponding to VHH conjugated IONP were used for in vivo pharmacokinetic studies (Figure 3.4).
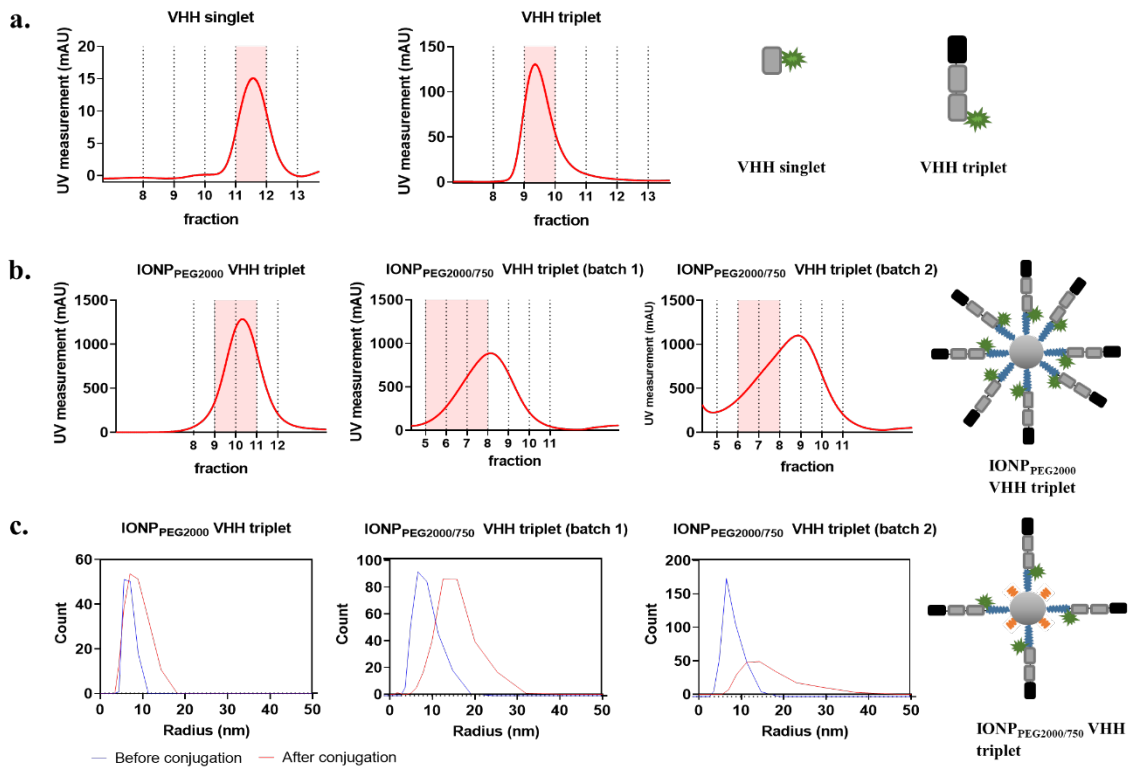
Figure 3.4. FPLC fractions of VHHs and IONPs as well as DLS measurement of IONPs. a. VHH singlet and VHH triplet fractions after passing through the Superdex 75GL size exclusion chromatography column. Elution fraction 11 for VHH singlet and fraction 9 for VHH triplet were collected for in vivo PK experiments (highlighted in pink). b. $IONP_{PEG2000}$ VHH triplet and $IONP_{PEG2000/750}$ VHH triplet fractions after passing through the Superose 6 Increase size exclusion chromatography column. Schematic drawing of $IONP_{PEG2000}$ VHH triplet with PEG2000 colored blue. Elution fraction 9 and 10 for $IONP_{PEG2000}$ VHH triplet, elution fraction 5, 6, and 7 for $IONP_{PEG2000/750}$ VHH triplet (batch1), 6 and 7 for $IONP_{PEG2000/750}$ VHH triplet (batch2) were collected for in vivo PK experiments (highlighted in pink). c. DLS hydrodynamic size measurements of $IONP_{PEG2000}$ and $IONP_{PEG2000/750}$ before (blue) and after (red) conjugation with VHH triplet. Schematic drawing of $IONP_{PEG2000/750}$ VHH triplet, with PEG2000 colored blue and PEG750 colored orange.

3.3.3 Animals

All animal experiments were conducted under protocols approved by the National Institute of

Neurological Disorders and Stroke (NINDS)/ National Institute on Deafness and Other

Communication Disorders (NIDCD) Animal Care and Use Committee in the National

Institutes of Health (NIH) Clinical Center. C57BL/6J female mice were purchased from

Jackson labs at 6-12-weeks of age and used at 7-12 weeks of age. 20 mice were randomized

into 4 groups with four to six mice in each group. Anesthetized mice were injected via tail vein

with VHH singlet (5 mice), VHH triplet (4 mice), IONP$_{PEG2000}$ VHH triplet (5 mice), or IONP$_{PEG2000/750}$ VHH triplet (6 mice) for PK studies. Experiments were performed at the same time each day. The dark color fur coat of the strain of mouse used impedes the penetration of NIR light; therefore, the fur overlaying the regions of interest was removed by applying a topical depilatory cream above the head, on the ventral and dorsal torso and tail of the mice one day prior to IV injection. Delayed skin hyperpigmentation was observed starting 4 days after hair removal.

3.3.4 Injection of nanoparticles

Mice were anesthetized with 60% oxygen/ 40% medical air gas mixture containing 5% isoflurane in an induction box. After a stable anesthesia plane was established, mice were maintained at 1.5-2% isoflurane level. Artificial tears ointment was applied to prevent eye injury due to drying. Mice were placed on an electrical heating pad to maintain body temperature. Nanoparticle conjugates and VHHs with different sizes (12µM VHH singlet, 4.75µM VHH triplet, IONP$_{PEG2000}$ VHH triplet, IONP$_{PEG2000/750}$ VHH triplet) were injected intravenously through single bolus injection at 0.1ml volume into mice through tail vein using 30 Gauge needle. Mice were maintained under anesthesia for approximately 3 minutes. Following the procedure, the mice were allowed to recover on a heating pad until fully ambulatory and then returned to their home cage with immediate access to food and water.

3.3.5 Multidose experiment

VHH triplet was used for the multidose experiment. Five mice were injected, as described above, with 0.1ml VHH triplet 3 times with 5 min interval between each dose. Mice were maintained under anesthesia for approximately 3 minutes during intravenous injection and imaging and allowed to recover between injections.

3.3.6 NIR imaging methods

Mice were anesthetized with 60% oxygen/40% medical air gas mixture with 5% isoflurane for induction of anesthesia and 1.5% isoflurane level for maintenance. Mice were imaged using the Pearl Trilogy Near-Infrared Fluorescent and Bioluminescent small animal imaging system (Licor, Nebraska, USA). The specific parameters for NIR imaging were resolution = 170um, fluorescence channel at 800nm (excitation at 785 nm and emission at 820 nm) for FNIR dye.
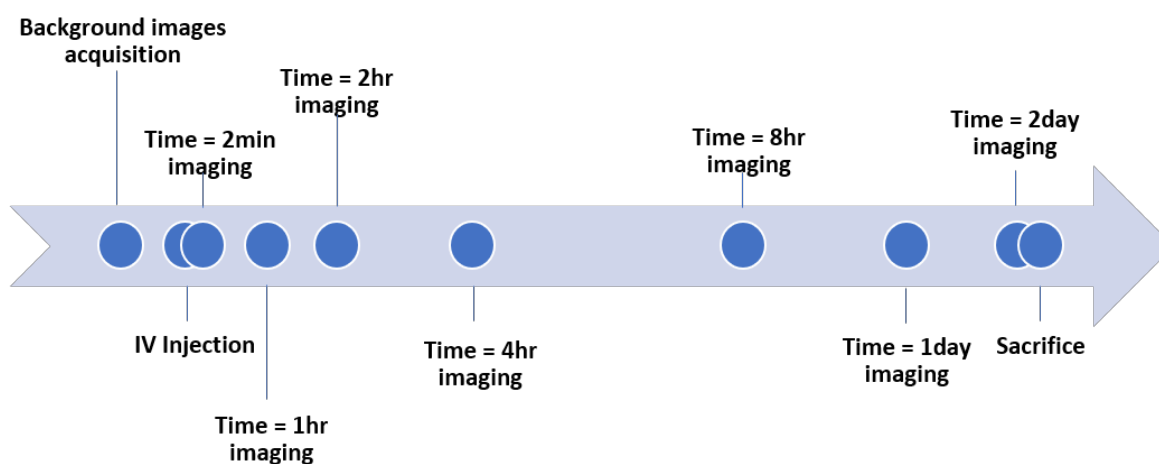
Figure 3.5. The experimental timeline of IV injection of VHHs and IONPs in mice. Background images were taken before injection, then NIR images were taken at 2min, 1hr, 2hr, 4hr, 8hr, 24 hours and 48 hours after injection. Mice were sacrifice after imaging at 48hr post injection.

NIR images were collected before and at time 2min, 1hr, 2hr, 4hr, 8hr, 1day, 2days post IV injection (Figure 3.5) using Pearl. After end-point imaging, mice were euthanized by transcardial perfusion using 1X phosphate-buffered saline (PBS) with heparin under 5% isoflurane.

3.3.7 Image and Data Processing
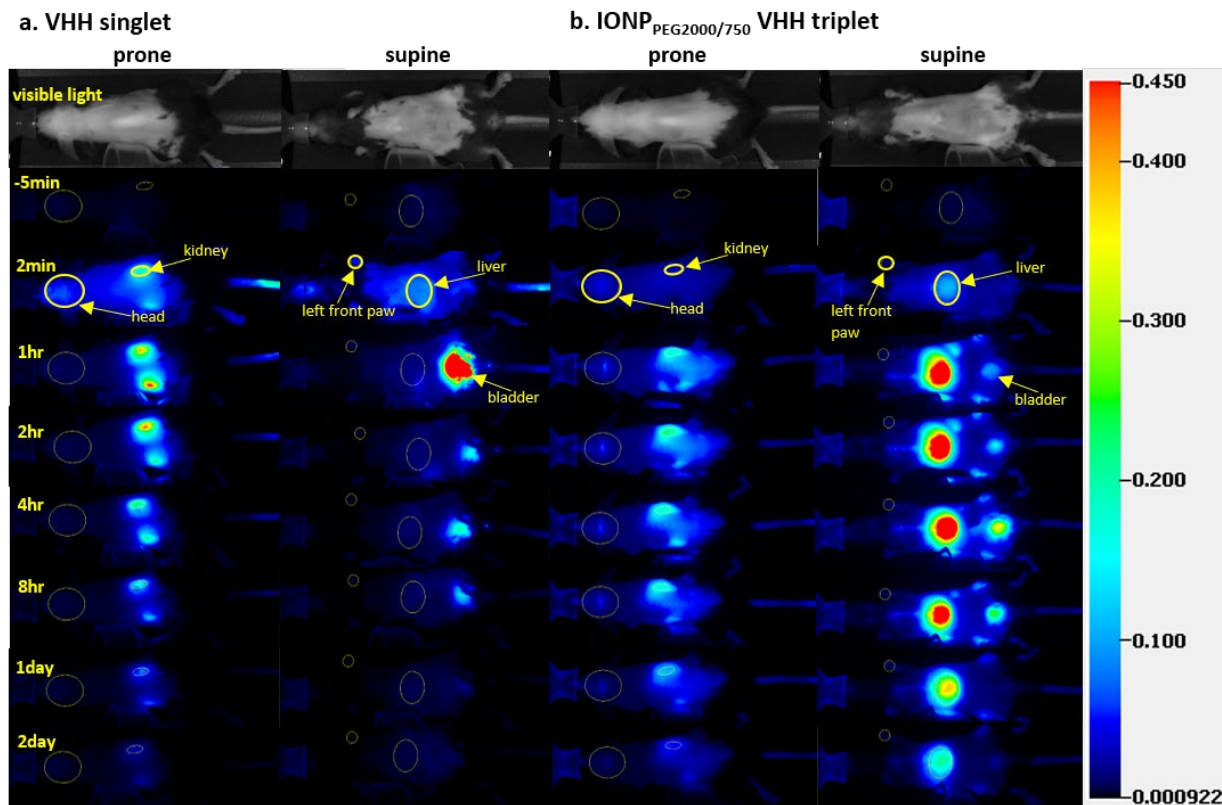
Figure 3.6. Representative in vivo serial fluorescence images and ROI analysis of VHH singlet (a.) and IONP$_{PEG2000/750}$ VHH triplet (b.). ROIs were drawn to track the fluorescence signal change of major ROIs including kidney and head (prone position), left front paw and liver (supine image) over time. Scale bar represents NIR image intensity measured by Pearl. a. In vivo serial fluorescence prone and supine position images before and 2min, 1hr, 2hr, 4hr, 8hr, 1day and 2day after IV bolus injection of VHH singlet. b. In vivo serial fluorescence prone and supine position images before and 2min, 1hr, 2hr, 4hr, 8hr, 1day and 2day after IV bolus injection of IONP$_{PEG2000/750}$ VHH triplet.

Equally sized regions of interest (ROI)s were manually drawn using the software Image Studio (ver 5.2) from Li-Cor. Examples of ROIs are shown in Figure 3.6. Head and right kidney ROIs were drawn from the prone view images while liver and front left paw ROIs were drawn from the supine view images. The average fluorescence intensity of each ROI was calculated and generated by Image Studio (ver 5.2).

3.3.8 Blood clearance measurement

Twelve mice (six for each VHH) were injected with VHHs (VHH singlet, VHH triplet) and

five mice were injected with nanoparticle IONP$_{PEG2000}$ VHH triplet as described in the

Injection of nanoparticles section. After intravenous injection, mice were sacrificed at 1min,

5min, 10min, 15min, 30min and 1hr for mice injected with VHHs and at 1min, 5min, 15min,
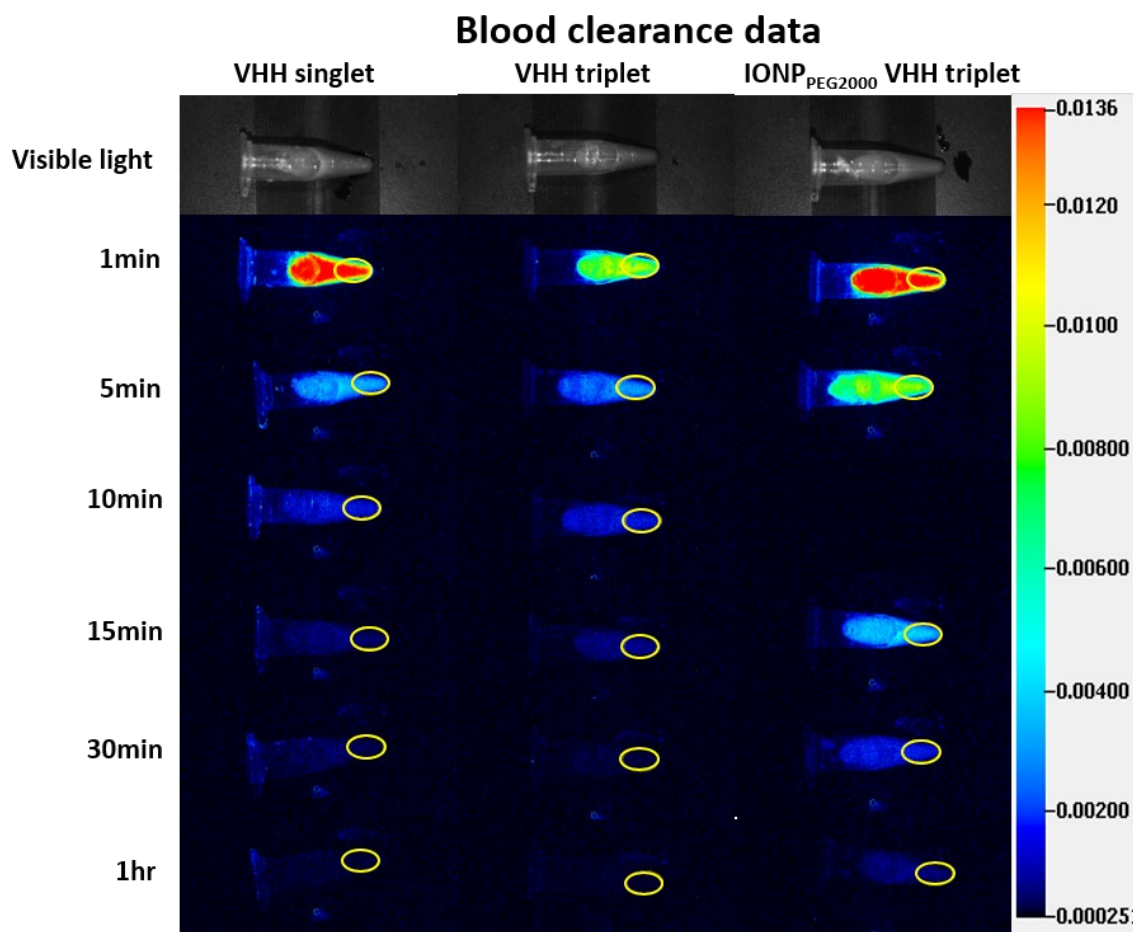
Figure 3.7. In vivo fluorescence images of blood. Scale bar represents NIR image intensity measured by Pearl. Mouse blood was collected at 1min, 5min, 10min, 15min, 30min and 1hr after IV injection of VHH singlet and VHH triplet. Mouse blood was collected at 1min, 5min, 15min, 30min and 1hr after IV injection of IONP$_{PEG2000}$ VHH triplet. ROIs were drawn for NIR signal analysis.

30min and 1hr for mice injected with IONP$_{PEG2000}$ VHH triplet. 0.1 to 0.2ml blood was

collected from the right atrium into heparin-coated 1.5ml microcentrifuge tubes. The

microcentrifuge tubes with blood were imaged using the Pearl system and ROIs were drawn

using the Image Studio software (Figure 3.7).

3.3.9 Mathematical modeling

Mathematical models were built using MATLAB (The Mathworks, Inc.) to predict distribution

and pharmacokinetics based on nanoparticle size. The mathematical models were built based

on kinetic data from VHH singlet, VHH triplet, IONP$_{PEG2000}$ VHH triplet, and IONP$_{PEG2000/750}$

VHH triplet data. Model fitting was done by minimization of the residual sum of squares

across all five compartments and the blood clearance rate using the particle swarm algorithm

[88, 89]. r^2 values were calculated to evaluate the goodness of fit. This model consists of 5

compartments: compartment 1 is the blood compartment, with a single bolus input and

exchange of nanoparticles/VHHs with compartment 2 (kidney compartment), compartment 3

(liver compartment), and compartment 4 (head 1 compartment). Compartment 4 also

exchanges with compartment 5 (head 2 compartment). In this model, the two main paths for

clearance are the kidney and liver compartments. Kidneys and liver are the two main organs

which are responsible for nanoparticle elimination [90]. The intake and clearance of

nanoparticles from blood to kidneys/liver are the main characteristics that differentiate the in

vivo kinetics of different nanoparticles and VHHs. The signal from spleen was not analyzed

because of low signal strength. This 5-compartment model was modified based on a 4-

compartment model with blood, liver and kidney compartment as well but only one head

compartment. Based on small sample corrected Akaike information criterion (AICc) value [91]

and model fitting, the 5-compartment model was selected over the 4-compartment model. Two

compartments were used to better describe the nanoparticles/VHHs in vivo distribution and

kinetics in head to guide the timing of future brain MRI studies.

3.4 Results

3.4.1 VHH and VHH-conjugated nanoparticle characterization

VHH singlet and VHH triplet products had characteristics consistent with expectation. Twenty-two 1ml elution fractions were collected from a Superdex 75 size exclusion chromatography column. Peak fractions of purified VHH singlet and VHH triplet were collected for FNIR conjugation. VHH singlet peaked at fraction 11 and VHH triplet peaked at fraction 9 (Figure 3.4a). Based on the protein size standards, VHH singlet and VHH triplet eluted from the columns as expected based on their calculated sizes of 12.7kDa and 36.1kDa respectively.

Based on the DLS data, the IONP$_{PEG2000}$ particles had a hydrodynamic radius of 6.4-6.7nm before and 7.0-7.6nm after conjugation with VHH triplet (Figure 3.4c). The 9th and 10th fractions from a Superose 6 Increase SEC column (optimized for larger particles) were used for IV injection and PK studies (Figure 3.4b). The IONP$_{PEG2000/750}$ VHH triplet constructs had hydrodynamic sizes of 8.3-9.1nm (batch 1) and 8.0-9.1nm (batch 2) before, and 11.9-13.9nm (batch 1) and 12.2-14.5nm (batch 2) after conjugation with VHH triplet. The 5th, 6th and 7th fractions from batch 1 and the 6th and 7th fractions from batch 2 from the Superose 6 Increase column were used for IV injection and PK studies (Figure 3.4b).

3.4.2 In vivo pharmacokinetic study using NIR

We optimized methods for NIR-based pharmacokinetic studies, and then used these methods to acquire consistent in vivo pharmacokinetic data in mice. The NIR fluorescence images acquired using the Pearl system showed very low background fluorescence signal at 800 nm, confirming that in the NIR, the intrinsic autofluorescence at this wavelength of light in the
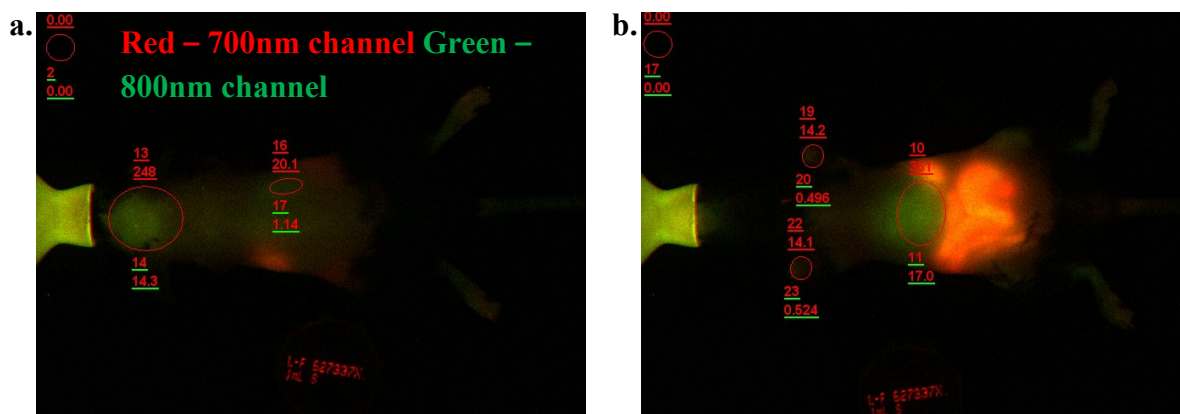
Figure 3.8. Representative image of background autofluorescence in a mouse imaged using the 700nm and 800nm channel with the Pearl system. a. Mouse background image in the prone position at 700nm (red) and 800nm (green) channel. b. Mouse background image in supine position at 700nm (red) and 800nm (green) channel. Autofluorescence at 700 nm is substantially higher than at 800 nm.

animals was negligible. Autofluorescence at 700 nm was higher, so we focused on 800 nm channel measurements for these experiments (Figure 3.8). It has been reported that the use of different NIR dyes can affect biodistribution of NIR-labeled VHHs [92] and monoclonal antibodies [93] . We tested IR-680RD dye (IRDye®), IR-800CW dye (IRDye®) and FNIR dye conjugated nanoparticles and confirmed that the dyes can affect the apparent biodistribution (Figure 3.9a). Mice had lower background autofluorescence at 800nm channel than the 700nm channel, so IR-800CW dye and FNIR dye were preferred over IR-680RD dye (Figure 3.9a). Comparing the IR-800CW dye and the FNIR dye, the signal quality and consistency was higher for the FNIR dye (Figure 3.9b). The stability of FNIR dye was tested by conjugating

a. 700nm channel

IONP-680RD

IONP-680RD

b. 800nm channel

IONP-800CW

IONP-800CW

c. **800nm**

IONP-

IONP-FNIR
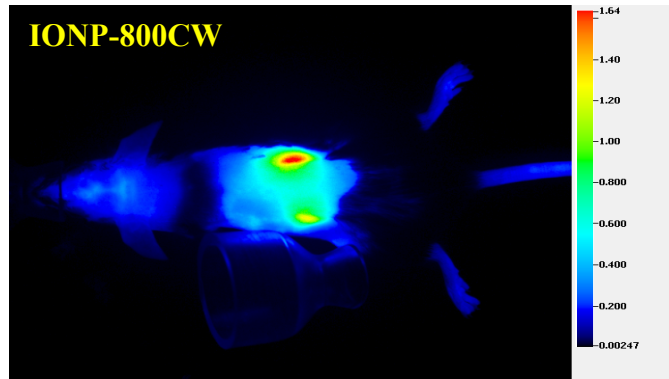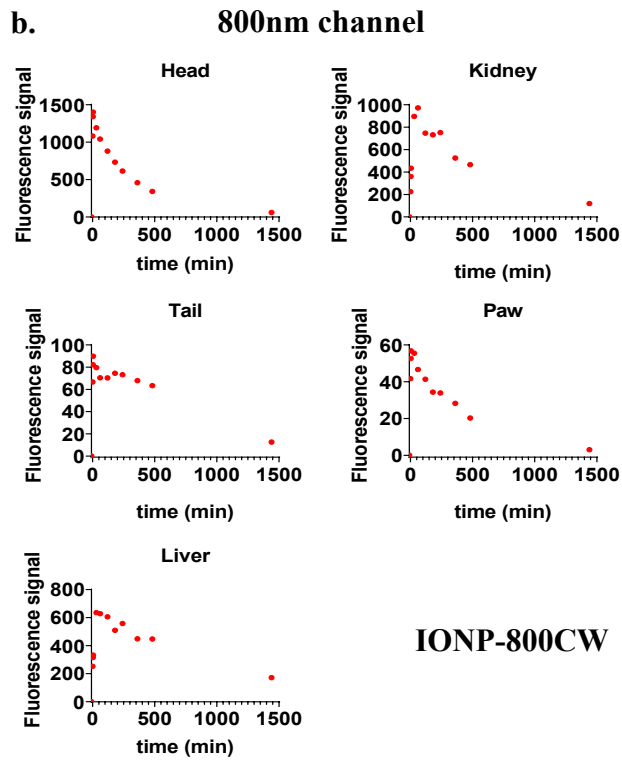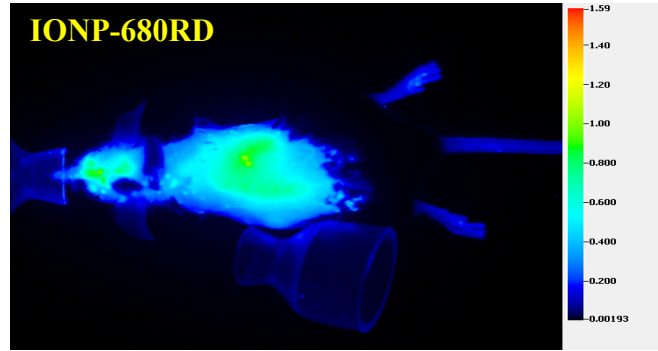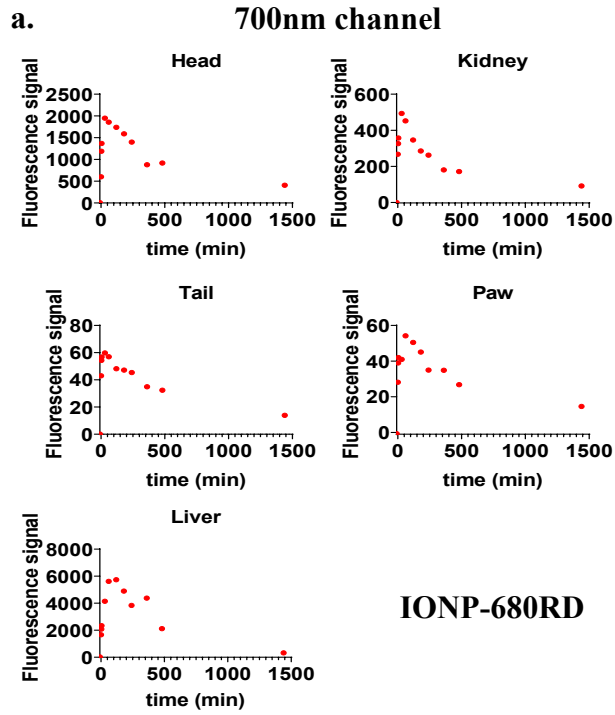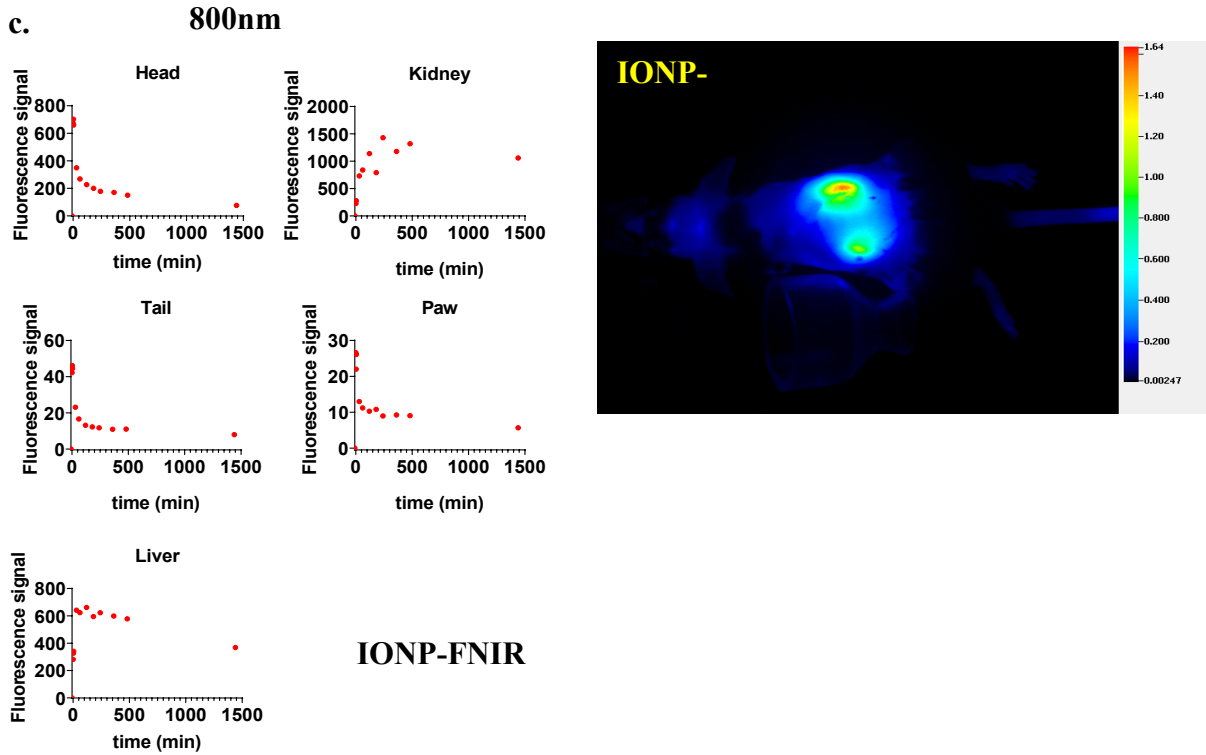
Figure 3.9. Effect of different NIR dyes on *in vivo* PK. Color bar represents NIR image intensity measured using the Pearl system. a. Representative data of mouse major ROI kinetics (Head, Kidney, Tail, Paw and Liver) and representative NIR images of mice 1hr after injection of IONP-IR-680RD dye. b. Representative data of mouse major ROI kinetics (Head, Kidney, Tail, Paw and Liver) and representative NIR images of mice 1hr after injection of IONP-IR-800CW dye. c. Representative data of mouse major ROI kinetics (Head, Kidney, Tail, Paw and Liver) and representative NIR images of mice 1hr after injection of IONP-FNIR dye.

a.

b.

- VHH singlet-FNIR Day0
- VHH singlet-FNIR Day14
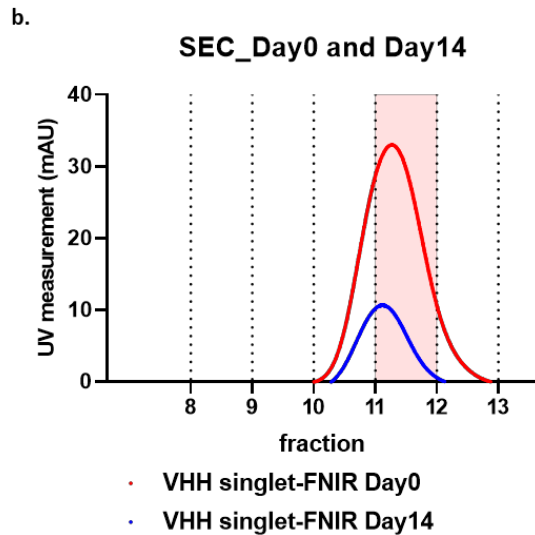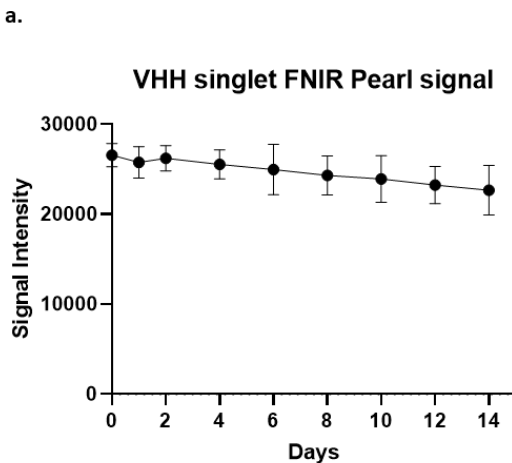
Figure 3.10. Stability of FNIR dye NIR signal. a. FNIR was conjugated to VHH singlet and the NIR signal was measured over 14 days using the Pearl system (n = 3). The FNIR dye signal was measured in the 800nm channel using the Pearl system. VHH singlet FNIR conjugate was kept in PBS at room temperature wrapped with aluminum foil to protect from light. The concentration of the VHH singlet FNIR conjugates were 6.85µM. Error bars represent standard deviations. b. FNIR was conjugated to VHH singlet and the size of VHH singlet-FNIR conjugate was measured with the Superdex 75 size exclusion column. VHH singlet-FNIR peaked at fraction 11 on both day 0 and day 14 after conjugation. The peak fractions on day 0 and day 14 were collected for NIR measurement as shown in a.

FNIR dye with VHH singlet. FNIR dye presented very good NIR signal stability (Figure 3.10a) and the VHH singlet-FNIR conjugate was stable in size over 14 days (Figure 3.10b).

NIR images of in vivo mice injected with four different FNIR dye conjugates (2 VHHs and 2 IONPs) showed that the conjugates had different biodistributions in head, kidney and liver and were cleared from mice at different rates (Figure 3.6). Regions of interest (ROIs) of major organs including head, kidney and liver were drawn on the images acquired before, 2min, 1hr, 2hr, 4hr, 8hr, 1day and 2day after IV injection at both prone and supine positions of mice (Figure 3.6a for VHH singlet, Figure 3.6b for $IONP_{PEG2000/750}$ VHH triplet). The reliability of ROI drawing method was calculated on 5 representative mice injected with VHH singlet (Figure 3.11). ROIs were drawn on the images two times on two different days. The Pearson correlation of the results from the two ROI drawings were very close to 1, indicating almost
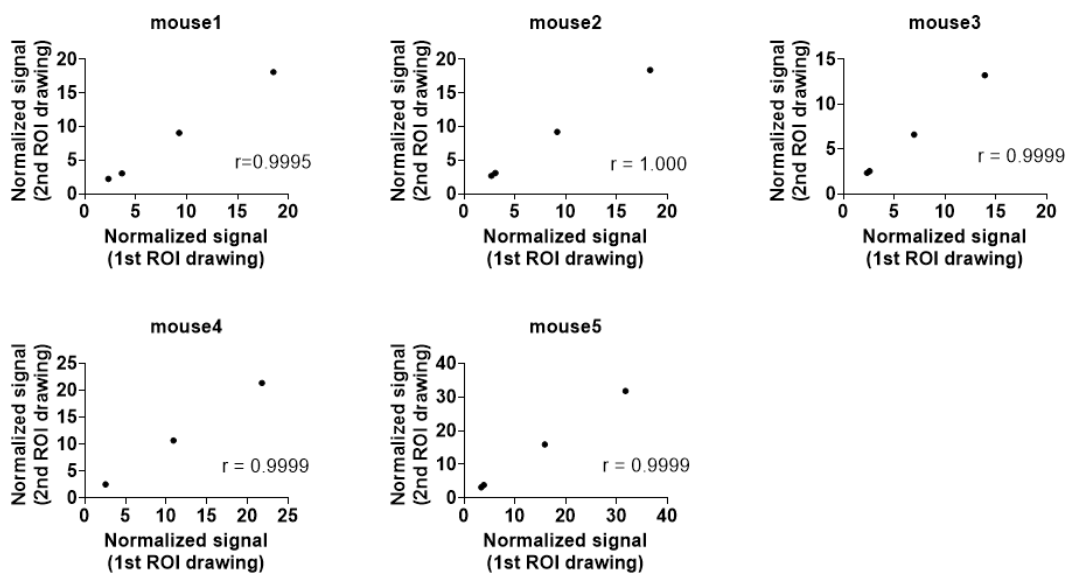
Figure 3.11. The test-retest reliability of ROI drawing. On a representative mouse injected with VHH singlet imaged 1hr after injection, major ROIs including head, kidney, liver and left front paw were drawn two times to assess the test-retest reliability of ROI drawing. The Pearson correlations were calculated to be 0.9995, 1.000, 0.9999, 0.9999, 0.9999 for the 5 mice, indicating that the 1st and 2nd ROI drawings give almost perfect reliability.

perfect reliability of the ROI drawing method. The fluorescence intensities of each organ were measured for PK analysis. Kidney intensities were multiplied by two to represent both kidneys. To analyze the relative NIR signal changes across mice injected with different FNIR dye conjugates which had different absolute NIR intensities, the main ROI fluorescence signals were normalized using left front paw signals at 2min post injection as internal controls values. We found this approach to be more reliable than using intrinsic fluorescence of the injected material or local tail fluorescence values. For VHH singlet, the pharmacokinetic plots of kidney and liver showed that kidneys and liver had similar uptake, but kidneys had much
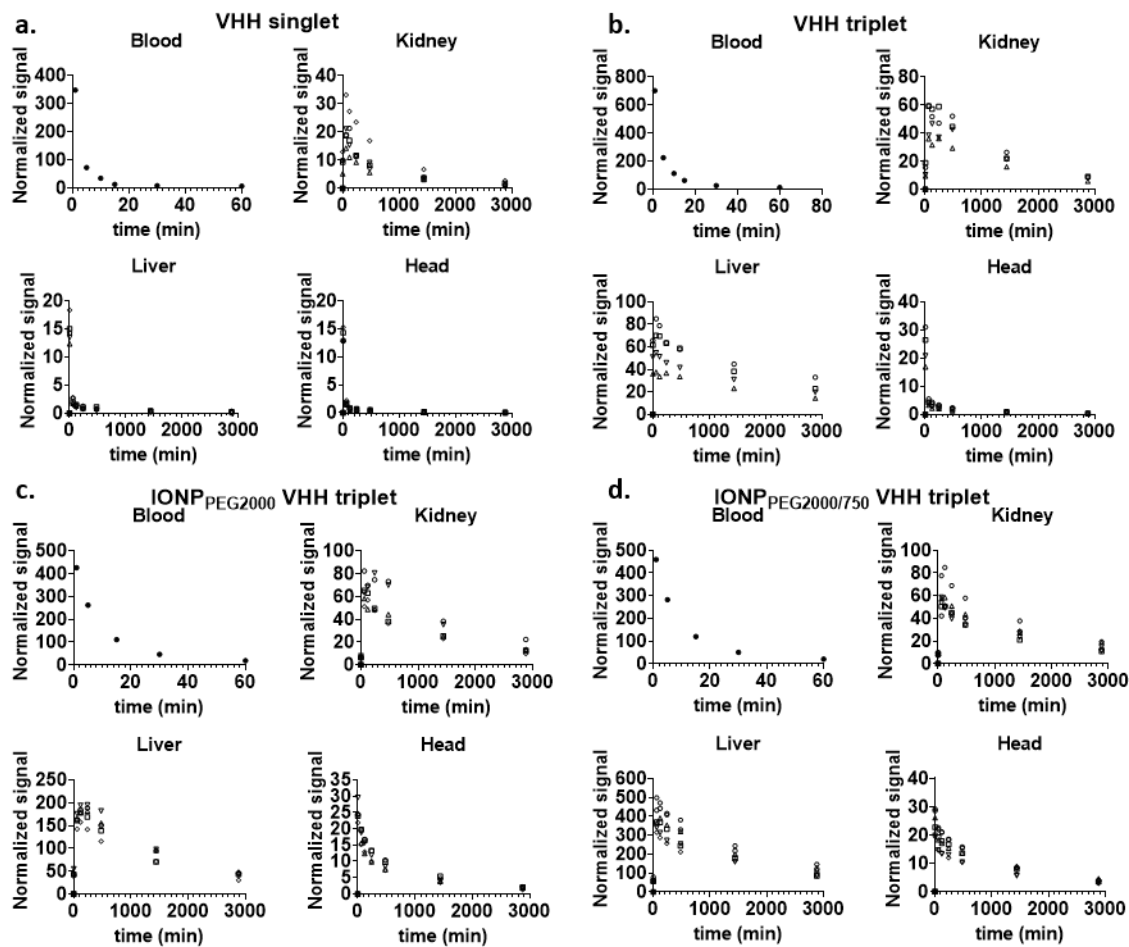
Figure 3.12. Major ROIs in vivo fluorescence signal changes over time. NIR signal change over time of major ROIs including blood, kidney, liver and head. a. VHH singlet (5 mice), b. VHH triplet (4 mice), c. IONP$_{PEG2000}$ VHH triplet (5 mice) and d. IONP$_{PEG2000/750}$ VHH triplet (6 mice) were injected by IV bolus and the NIR signal change were monitored in major ROIs.

slower fluorescence intensity decrease rate than liver, indicating that kidneys were the major organ for VHH singlet clearance (Figure 3.12a). For VHH triplet, the pharmacokinetic plots of kidney and liver showed that kidneys and liver had similar uptake and clearance rates, indicating that kidneys and liver both contribute to the clearance (Figure 3.12b). For IONP$_{PEG2000}$VHH triplet and IONP$_{PEG2000/750}$ VHH triplet, the pharmacokinetic plots of kidney and liver showed that liver had much larger uptake of nanoparticles than kidneys, indicating that liver was the main organ for the IONP-VHH conjugate clearance (Figure 3.12c&d). There

46

were only modest differences in kinetics between the two different PEG coatings that were used to make the IONPs water soluble and serve as linkers for VHH conjugations. Particles coated with PEG2000 vs. particles coated with a 1:1 ratio of PEG2000 to PEG750 had similar kinetics with predominant liver uptake and biphasic clearance from the head compartment. The relationship between dose and kinetics was also explored using VHH triplet as an example
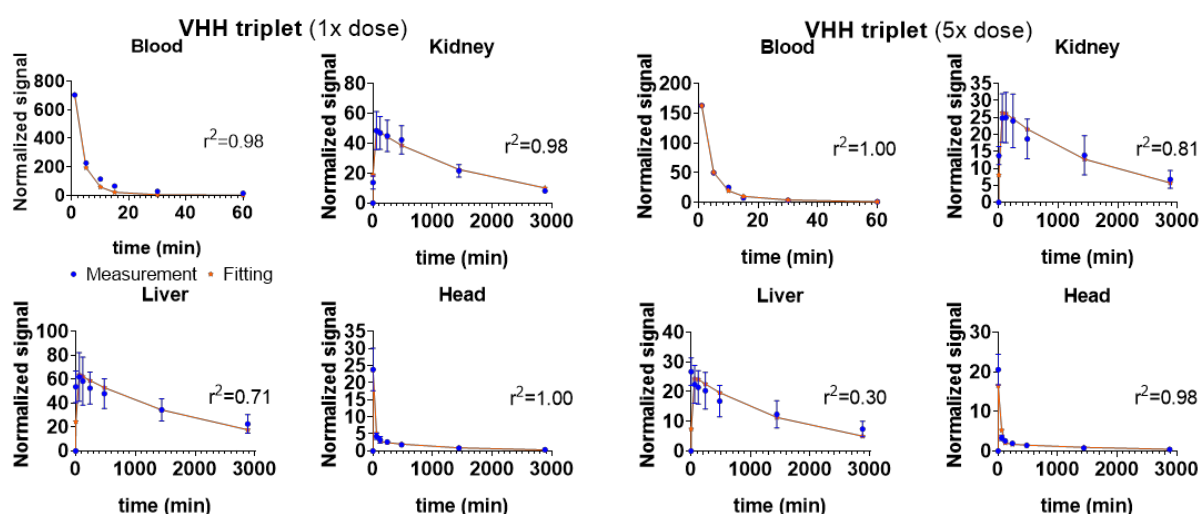
Figure 3.13. Dose-linearity testing: Fitting (red lines) of the 5-compartment model solutions to the VHH triplet (1x dose) and VHH triplet (5x dose) measured data (blue symbols). The fitting-based kidney ratio and liver ratio are 37.18 and 33.11 for VHH triplet (5x dose) (n = 6), 25.74 and 40.80 for VHH triplet (1x dose) (n = 4). Kidney ratio and liver ratio for VHH triplet (5x dose) and VHH triplet (1x dose) are on the same order and similar to each other. Error bars represent standard deviations.

(Figure 3.13). In this experiment, a higher dose VHH triplet at a concentration of 24.23 μM was intravenously injected into 6 mice and NIR images were taken at the same time points as in other experiments. Lower dose (4.75μM) and higher dose (24.23μM, ~5x lower dose) VHH triplet showed similar signal kinetics over all compartments. Higher dose and lower dose VHH triplet had very similar calculated kidney ratio and liver ratio, indicating dose-linearity of kinetics for VHH triplet.

All mice injected with VHH singlet, VHH triplet, IONP$_{PEG2000}$VHH triplet and IONP$_{PEG2000/750}$ VHH triplet appeared healthy. No overt behavioral abnormalities were noted and veterinary intervention was not required.

3.4.3 Blood clearance measured by NIR

A limitation of the NIR fluorescence imaging approach was that we were unable to consistently assess the PK in blood. We initially tested the assumption that PK in peripheral tissues such as paw and tail would reflect PK in blood, but this turned out not to be correct; clearance from blood was substantially faster than peripheral tissues such as paw. Signal in ROIs containing heart and tongue muscle were too low to use for consistent model fitting [80, 81] (Figure 3.6). Therefore, we adopted a hybrid approach, and measured PK in blood by direct sampling of blood from mice separate groups of mice sacrificed at multiple time points. Blood was sampled at 1min, 5min, 10min, 15min, 30min and 1hr after IV injection and quantified using ROIs drawn on the NIR images of the ex vivo blood (Figure 3.7). Then, the blood clearance curves were fitted using a single exponential equation (Figure 3.14). The NIR fluorescence images of ex vivo blood indicated fast blood clearance rate of VHHs and slower rate of VHH-IONP. Most of the materials were cleared out of the blood within the first 1hr post injection. The fitted half-lives were 7.09min, 2.86min, and 1.94min for IONP$_{PEG2000}$ VHH triplet, VHH triplet and VHH singlet respectively.
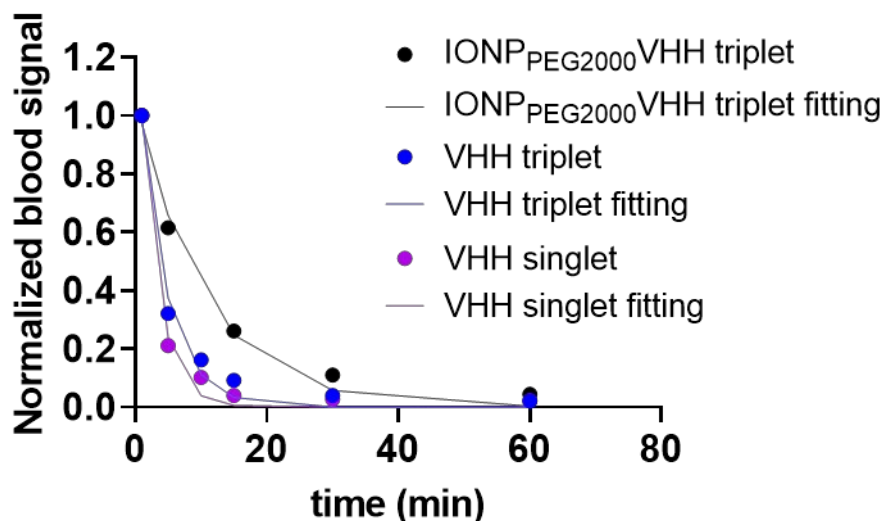
Figure 3.14. Blood clearance data and single exponential fitting. The NIR signals of VHH singlet, VHH triplet and IONP$_{PEG2000}$ VHH triplet in mouse blood after IV bolus injection. The NIR signals were measured at 1min, 5min, 10min, 15min, 30min and 1hr post injection for VHH singlet and VHH triplet. The NIR signals were measured at 1min, 5min, 15min, 30min and 1hr post injection for IONP$_{PEG2000}$ VHH triplet. The NIR blood signals were normalized to signals at 1min post IV injection and fitted using the single exponential equation $y = a * e^{-\frac{x}{\tau}}$. the time constant τ best fit values were 2.80min, 4.13min and 10.24min for VHH singlet, VHH triplet and IONP$_{PEG2000}$ VHH triplet.

3.4.4 Mathematical modeling

This mathematical PK model described the in vivo PK of FNIR-VHHs and FNIR-IONP-VHHs by segmenting the body into five main compartments and the five compartments were related through mass transfer (Figure 3.15). X1, X2, X3, X4 and X5 were the amounts of conjugates in blood, kidney, liver, head 1, and head 2 compartments. k12, k21, k13, k31, k14, k41 were the forward and reverse first-order transfer rate constants for the intercompartment change between blood compartment and kidney, liver, and head compartments. k45 and k54 were the forward and reverse first-order transfer rate constants for intercompartment change between head 1 and head 2 compartments. K10 was the first-order rate constant for clearance. The
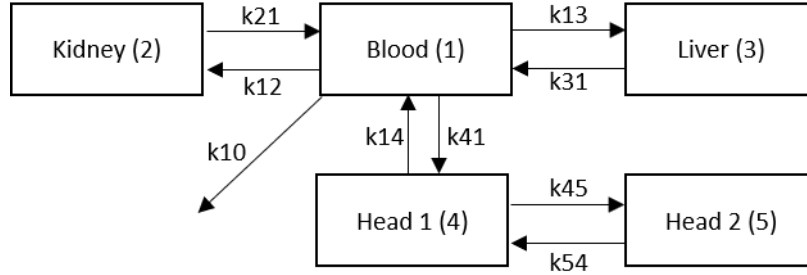
Figure 3.15. Schematic graph for the 5-compartment mathematical model. This schematic graph describes the in vivo kinetics of VHHs/IONPs, including uptake, clearance and intercompartment exchanges. This model is characterized by a system of five ordinary differential equations (ODEs). k12, k21, k13, k31, k14, k41 are the forward and reverse first-order transfer rate constants for the intercompartment change between blood compartment and kidney, liver, and head compartments. k45 and k54 are the forward and reverse first-order transfer rate constants for intercompartment change between head 1 and head 2 compartments. k10 is the first-order rate constant for clearance from blood.

initial condition of blood compartment was used to describe the bolus IV injection to the blood compartment and set to be the normalized conjugate fluorescence intensity (normalized by left front paw signal intensity). The initial conditions of kidney, liver, paw and head compartments were set to be 0, based on the assumption that the nanoparticles/VHHs enter these organs only through the blood. The five ordinary differential equations were established to describe the mass transfer of VHHs/IONPs between the five compartments and their clearance.

$$\frac{dX1}{dt} = -(k_{12} + k_{13} + k_{14} + k_{10})X_1 + k_{21}X_2 + k_{31}X_3 + k_{41}X_4 \tag{3.1}$$

$$\frac{dX2}{dt} = -k_{21}X_2 + k_{12}X_1 \tag{3.2}$$

$$\frac{dX3}{dt} = -k_{31}X_3 + k_{13}X_1 \tag{3.3}$$

$$\frac{dX4}{dt} = -(k_{41} + k_{45})X_4 + k_{14}X_1 + k_{54}X_5 \tag{3.4}$$

$$\frac{dX5}{dt} = -k_{54}X_5 + k_{45}X_4 \tag{3.5}$$
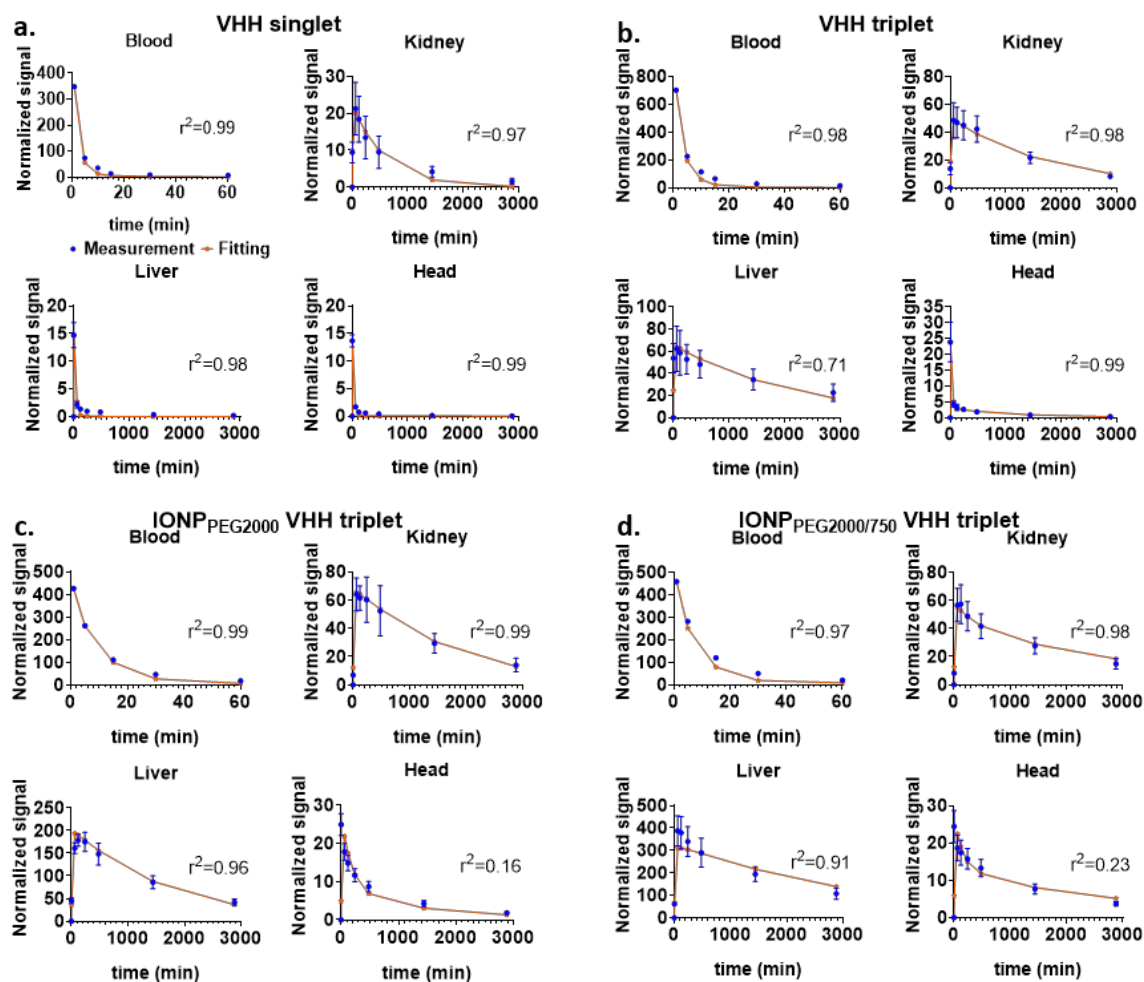
Figure 3.16. Fitting of the 5-compartment model solutions to the experimentally measured fluorescence data. Fitting of the model simulated solutions (red line) and the measured normalized NIR signals (blue dot) of major organs after IV injection of VHH singlet (a.), VHH triplet (b.), IONP$_{PEG2000}$ VHH triplet (c.) and IONP$_{PEG2000/750}$ VHH triplet (d.). Error bars represent standard deviations.

The normalized averaged PK data were fitted using the 5-compartment model. Figure 3.16 shows the optimal model fitting for the two VHH constructs and the two VHH conjugated IONPs. The fitting corresponded well with the normalized data. A 4-compartment model with only one head compartment was tested first (Figure 3.17). However, with only one head compartment, the fitting did not match the trend of head signal change as well (Figure

51
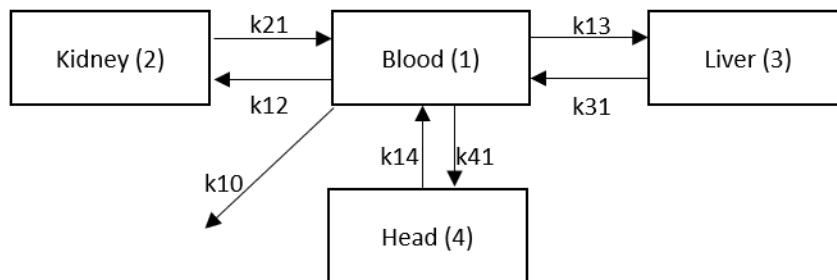
$$\frac{dX1}{dt} = -(k_{12} + k_{13} + k_{14})X_1 + k_{21}X_2 + k_{31}X_3 + k_{41}X_4$$

$$\frac{dX2}{dt} = -(k_{21})X_2 + k_{12}X_1$$

$$\frac{dX3}{dt} = -(k_{31})X_3 + k_{13}X_1$$

$$\frac{dX4}{dt} = -k_{41}X_4 + k_{14}X_1$$

Figure 3.17. Schematic graph and equations for the 4-compartment mathematical model. This schematic graph describes the in vivo kinetics of VHHs/IONPs, including uptake, clearance and intercompartment exchanges. This model is characterized by a system of four ordinary differential equations (ODEs). k12, k21, k13, k31, k14, k41 are the forward and reverse first-order transfer rate constants for the intercompartment change between blood compartment and kidney, liver, and head compartments. k10 is the first-order rate constant for clearance.

3.18&3.19). A second head compartment was added to better fit the head signal change (Figure 3.16). Small sample corrected Akaike Information criteria (AICc) values were -35.90, -16.85, -20.47, and -41.29 for 4 compartment fitting and -41.59, -22.62, -27.48, -39.09 for 5-compartment model fitting of VHH singlet, VHH triplet, IONPPEG2000 VHH triplet and IONPPEG2000/750 VHH triplet respectively. Because models with lower AIC values are preferred, the 5-compartment model was selected. No additional kidney or liver compartments were added because the benefit in terms of fitting was limited, and not justified based on the increased complexity of the model. Similarly, there was no additional benefit of adding kinetic parameters representing direct clearance from kidney (k20) or liver (k30) in terms of model

fitting and these rate constants could not be independently constrained by the acquired data. Therefore, these kinetic parameters were not included in the final models. For VHHs/nanoparticles which do not appreciably cross the BBB, PK of paw and head compartments were similar (Figure 3.20), so the paw compartment was not included in the model separately.
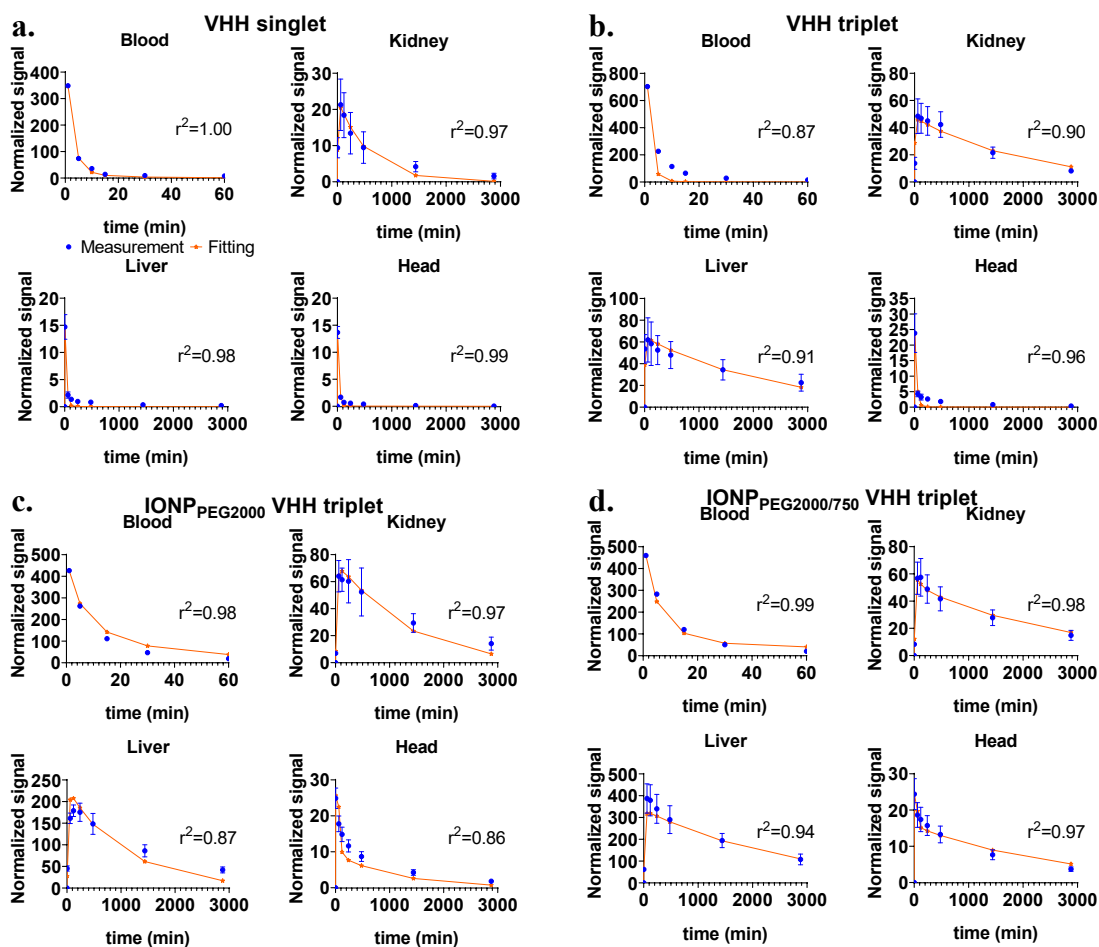
Figure 3.18. Fitting of the 4-compartment model solutions to the experimentally measured fluorescence data. Fitting of the model simulated solutions (red lines) and the measured normalized NIR signals (blue symbols) of major ROIs after IV injection of VHH singlet (a.), VHH triplet (b.), IONP$_{PEG2000}$ VHH triplet (c.) and IONP$_{PEG2000/750}$ VHH triplet (d.). The data is the same as that shown in Figure 3.16. Error bars represent standard deviations.
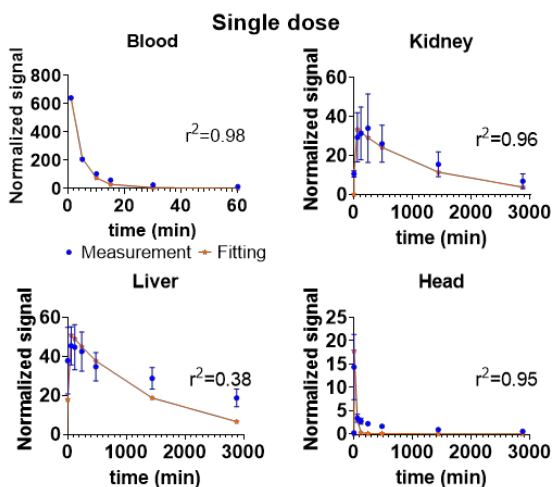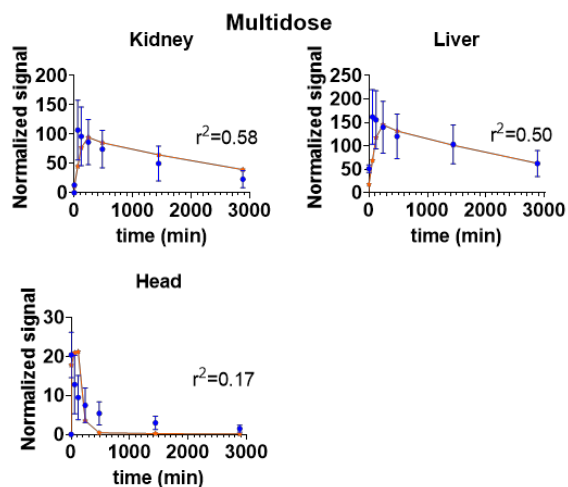
Figure 3.19. Prediction of multidose regimen using 4-compartment model using fitted parameters from single dose experiment. a. NIR signal change over time after single IV bolus injection (n=3 mice, blue dot) and the fitting solution (red line) calculated by the 4-compartment model. b. Experimentally measured fluorescence signal (n=5 mice, blue dot) and prediction of multidose signal (red line) based on the 4-compartment model single dose fit. Three bolus IV injections with time interval of 5 min between doses was performed for the multidose experiment. Error bars represent standard deviations.
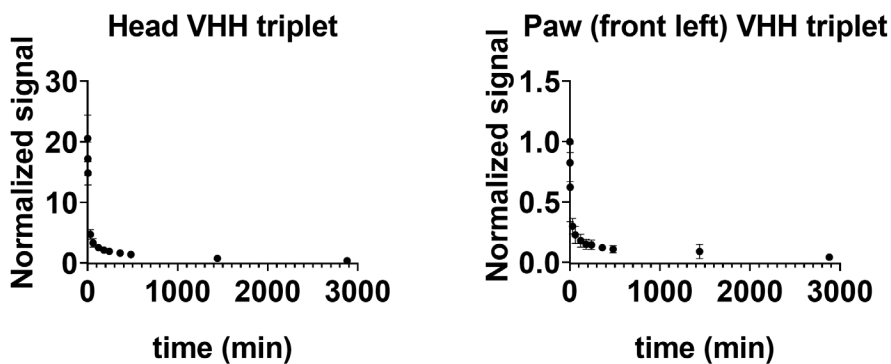
Figure 3.20. Representative PK data of head and front left paw after VHH triplet injection. The head and front left paw show similar PK (n = 6). Error bars represent standard deviations.

Table 3.1. 5-compartment model fitted parameters for VHH singlet, VHH triplet, IONP$_{PEG2000}$ VHH triplet and IONP$_{PEG2000/750}$ VHH triplet.

	k12	k21	k13	k31	k14	k41	k45	k54	k10
VHH singlet	0.0206	0.0018	0.0317	0.0502	0.0302	0.0847	0.3678	0.9212	0.3000
VHH triplet	0.0173	0.0007	0.0225	0.0006	0.0232	0.0625	0.0027	0.0010	0.2000
IONP$_{PEG2000}$ VHH triplet	0.0156	0.0019	0.0466	0.0019	0.0063	0.0058	7.51 E-05	0.9870	0.0300
IONP$_{PEG2000/750}$ VHH triplet	0.0155	0.0032	0.0836	0.0024	0.0072	0.0063	0.0011	0.0050	0.0150

Table 3.2. 5-compartment model fitting r^2 values of blood, kidney, liver and head ROIs. Kidney and liver uptake/clearance ratios are also calculated for each molecule.

	r^2 blood	r^2 kidney	r^2 liver	r^2 head	Kidney ratio	Liver ratio
VHH singlet	0.98881	0.9718	0.9802	0.9942	11.2928	0.6317
VHH triplet	0.98027	0.9829	0.7086	0.9975	25.7424	40.8006
IONP$_{PEG2000}$ VHH triplet	0.9949	0.9918	0.9592	0.1556	8.3823	24.1638
IONP$_{PEG2000/750}$ VHH triplet	0.9749	0.9831	0.9150	0.2268	4.8673	35.4626

Table 3.1 shows the optimal sets of fitting parameters for the two VHHs and the two IONPs. Table 3.2 shows the r^2 values and calculated kidney and liver uptake/clearance ratios, which were calculated by the equations:

$$Kidney\ ratio = \frac{k_{12}}{k_{21}} \tag{3.6}$$

$$Liver\ ratio = \frac{k_{13}}{k_{31}} \tag{3.7}$$

Comparing the values of kidney ratio and liver ratio, the kidney intake/clearance ratio was much larger than liver ratio for VHH singlet, the kidney and liver ratios were similar for VHH triplet, and the liver ratio was much larger than kidney ratio for both VHH conjugated nanoparticles. As expected, as the size increased from VHH singlet to IONP$_{PEG2000/750}$ VHH

triplet, the fitted liver ratio increased compared with the kidney ratio, replacing the kidney ratio's dominant position. This is consistent with previous findings that when molecular size is below the renal filtration, molecules are mostly filtered out of the body through the kidneys. As molecular size increases and passes the renal filtration cutoff, liver plays a more substantial role in clearance.

3.4.5 Multidose experiment and model fitting

As a test of the accuracy of the model, we used single dose-based kinetic parameters to predict the kinetics after multiple doses. An experiment with both single dose and multidose IV injection was performed using VHH triplet. Single dose PK measurements was performed by intravenously injecting 0.1ml VHH triplet into 3 mice and an additional group of 5 mice received 3 doses of the same 0.1ml VHH triplet with time interval of 5 min between doses. The normalized averaged single dose mice data was fitted using the 5-compartment model. The 5-compartment model fit the single dose data well, with r^2 value of 0.9947, 0.9747, 0.5998, and 0.9995 for blood, kidney, liver, and head compartment respectively. Then the predicted multidose kinetics were calculated based on the model with no additional free parameters through superposition. Finally, the single dose model-based predicted multidose

a. Single dose measurement and fitting
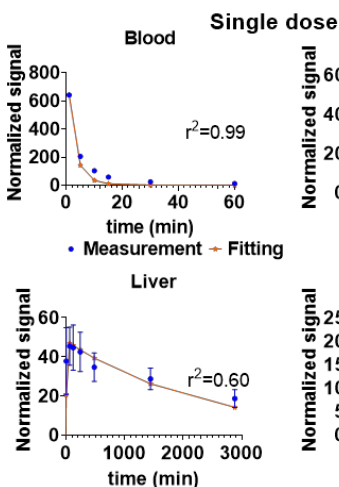
b. Model calculated vs measured multidose PK (5min interval 3 doses)
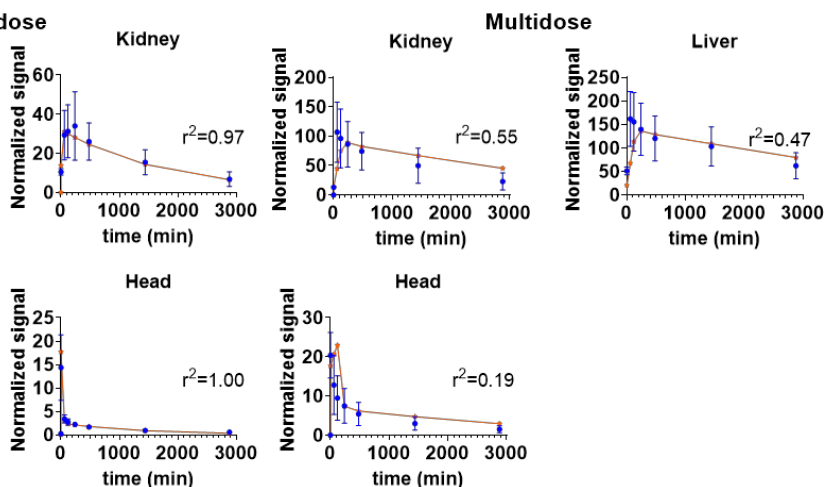
Figure 3.21. Prediction of multidose regimen using 5-compartment model fitted using parameters from single dose experiment. a. NIR signal change over time after single IV bolus injection (n=3 mice, blue dot) and the fitting solution (red line) calculated based on the 5-compartment model. b. Experimentally measured fluorescence signal (n=5 mice, blue dot) and prediction of multidose signal (red line) based on the 5-compartment model single dose fit with no free parameters. Three bolus IV injections with time interval of 5min between doses was performed for the multidose experiment. Error bars represent standard deviations.

kinetics were compared with the measured multidose kinetics (Figure 3.21a). The model-based predicted multidose kinetics closely followed the trend of the experimentally measured multidose kinetics (Figure 3.21b). Thus, the multidose data was moderately well fit by the model based on PK parameters derived from the single dose data, with r^2 values of 0.5529, 0.4701, and 0.1855 for kidney, liver, and head compartment.

3.5 Discussion

In summary, we found that the kinetics of VHHs and VHH-conjugated iron oxide nanoparticles were clearly related to their size. The smallest sized VHH singlets were cleared mostly by the kidneys. As the size increased, the liver became progressively more dominant in the uptake and clearance of VHHs/nanoparticles. These findings are consistent with the hypothesis that the NIR imaging for PK study can provide information about relative

nanoparticle/VHH concentration changes in mouse tissues and are in line with previous knowledge about renal filtration. It is known that the threshold of glomerular filtration for macromolecules and nanoparticles is between 5 and 8nm with progressively decreasing filtration as molecular size increases [94-96]. The PK model constructed in this study had 5 compartments, blood, kidney, liver, head, and head extracellular compartment. For model fitting, blood compartment kinetic data were needed. However, NIR signal from the blood compartment could not be directly measured using the Pearl system in vivo. Ex vivo experiments were therefore performed to understand the blood NIR signal change after IV injection of VHHs and to help with the model fitting. Thus, this approach should be considered a hybrid, with direct sampling of blood, and serial NIR imaging-based sampling of other compartments.

This study found that the relative value of uptake/clearance of liver and kidney ratios based on the fitted PK parameters can be used as reference to understand the relationship between VHH/nanoparticle sizes and in vivo behavior. Because we are most interested in nanoparticle/VHH's kinetics in head for future nanoparticle/VHH brain targeting experiments, a second head compartment was added to the model. This model describes the nanoparticle/VHH kinetics in head more accurately than a model with a single head compartment. We demonstrated the robustness of the fitted PK model by testing linearity (Figure 3.13) and multidose conditions (Figure 3.21).

The VHHs and nanoparticles characterized in this study are prototypes for the design of the final contrast agents. Because we have not yet achieved BBB crossing, the binding of the VHHs and nanoparticles to their targets in the brain is not described in this paper. Instead, to facilitate development of the final contrast agents with optimal delivery capacity and biosafety,

this study focused on understanding the relationship between in vivo pharmacokinetic (PK) characteristics and size of these prototype VHHs and nanoparticles.

It was found that in the NIR range of around 650nm to 900nm wavelength, biological tissues have the lowest absorption coefficient and minimum tissue autofluorescence [97, 98]. Fluorescence dyes with excitation/emission wavelength in the near-infrared range have deeper penetration depth than visible light and provide higher signal to background ratio with decreased background noise and modest autofluorescence [99-101]. The advantage of our study is that it uses NIR to capture images from individual mice post IV injection over time. The time-series images collected from individual mice reduce variations between mice and improve data consistency. Also, the number of mice used was greatly reduced compared with the conventional methods for PK data collection (e.g. ICP-MS measurement of iron content). For a conventional ICP-MS based PK study, multiple animals need to be sacrificed to collect data at each time point [77, 78]. In our NIR imaging-based PK experiment, 20 mice were used to collect the main data: 5 mice for each of 4 VHH or VHH-nanoparticle constructs. To get the same amount of data, a conventional PK study would have required 140 mice (5 mice x 4 constructs x 7 time points) in total. NIR imaging also has the advantages of fast imaging speed, low cost, and modest regulatory oversight requirements compared to other imaging methods used for PK studies such as PET, SPECT, and MRI. A limitation of NIR imaging approaches in the past has been the quality of the dyes available. Compared with commercially available dye IR-800CW, the FNIR we used has advantages including reduced aggregation and dramatically increased NIR emission brightness [85]. FNIR dyes have been used to label monoclonal antibodies to visualize the biodistribution and clearance following IV injection in mice [93].

60

Modeling pharmacokinetics with mathematical models helps with decision making in nanoparticle development. Pharmacokinetic modeling has been widely used to guide drug and nanoparticle development [102, 103]. Compartment models are designed to simplify the complex processes related to drug distribution and elimination in the body [90]. In compartment models, drug tissue concentration is assumed to be uniform within a given hypothetical compartment. Tissues with similar PK characteristics are lumped into one hypothetical compartment. Compartment models have been used to understand drugs and nanoparticles in vivo PK [104-106]. Gadkar, K., et al. constructed a two-compartment model to guide antibody selection for Aβ reduction [102]. Uno, Y., et al. constructed a three-compartment model to estimate the interstitial concentration of talaporfin sodium [105]. Sim, H., et al. established a two-compartment model to study the relationship between tumor growth and drug uptake kinetics [107]. In this study, we established a multi-compartment model based on NIR images which describes the PK of VHHs and nanoparticles in blood as well as other tissue compartments. This multi-compartment model will be used to guide future nanoparticle development and the compartments can be adjusted based on the study focus.

One limitation of this study is that the signal from NIR images does not reflect the absolute concentrations in the compartments of interest. The presence of skin and soft tissues reduces image quality by optical attenuation and scattering [100, 101]. We propose that fluorescence signals provide information about the relative concentration kinetics in major ROIs, rather than exact concentration values. In addition, NIR methods are less amenable to assessing smaller compartments such as spleen or bone marrow. Clearly, NIR approaches are best suited for relatively short-term studies in small animals such as mice with little intrinsic skin pigmentation; in larger animals there is too much attenuation between the tissues of interest

and the detectors. Longer term PK studies would be difficult because of the challenges of maintaining hair removal for more than a few days without compromising health.

Another substantial limitation is that we only characterized PK in relation to construct size. There are many other properties of IONPs including hydrophobicity, surface charge, coating or conformation of nanoparticles/VHHs that could affect their PK and biodistribution [15, 17, 31, 78]. We found minimal differences between IONPs coated with PEG2000 vs a 1:1 ratio of PEG2000 to PEG750. Thus, there does not seem to be a major effect of the length of PEG coating in this case. Furthermore, the nanoparticles tested in this study are not our final product, and the binding properties of next generation nanoparticles will certainly influence the in vivo PK and will require modification of the model.

We acknowledge that we have not performed blood measurements for both IONP-VHH constructs; we collected blood data for the IONP$_{PEG2000}$ VHH triplet but not the IONP$_{PEG2000/750}$ VHH triplet. Based on the findings that organ PK was essentially the same for these two IONP-VHH constructs, we used the blood data from IONP$_{PEG2000}$ VHH triplet to constrain PK models for both constructs. This relies on the assumption that the blood clearance of the two IONPs were similar. Both models fit well, so this assumption seems reasonable.

There were several additional limitations. The precise stoichiometric relationships of iron oxide: PEG: VHH conjugates have not been determined. We plan to use thermogravimetric analysis (TGA) to assess the nanoparticle stoichiometry in the future [108]. Also, opsonization/fouling of the nanoparticles in blood was not assessed in this study [109, 110]. Our preliminary data (unpublished) indicate that similar PEG-coated IONPs remain stable in size over 24 hours at 37C° in human plasma, suggesting minimal fouling. Furthermore, we have not collected urine or feces, thus excretion was not directly measured. Finally, we have

not systematically assessed toxicity. Toxicity of IONPs is concentration and exposure time dependent [111, 112]. In general, iron oxide nanoparticles are considered very safe, but potential risks of iron can be related to oxidative stress and potential risks of foreign proteins can include immune responses [26, 113]. Cationic iron can increase the production of reactive oxygen species (ROS) which may react and damage cell membrane and DNA. The cytotoxicity of our IONPs will be explicitly assessed in the future. We have not performed multidose experiments with long enough intervals between doses to assess for potential immune-related toxicity of the llama VHH proteins.

For future experiments, we will study the PK and distribution of the nanoparticles with adjusted components including VHHs targeting specific brain proteins and BBB components. PK and clearance of updated nanoparticle designs will be measured using the NIR imaging method and will be fitted using the PK compartment model developed in this paper. More complex, possibly nonlinear, models including information about binding kinetics and binding capacities will also be developed. Such experiments will incorporate genetically manipulated mice expressing human brain proteins and BBB components. Thus, for experiments involving complex genetically manipulated animals, methods that reduce the number of mice needed are especially relevant. Differences between genetically manipulated mice and appropriately matched controls will help reveal whether there are differences in in vivo kinetics and clearance indicating target engagement of nanoparticles with biomarkers in brain. The mathematical PK models will be used to design experiments involving injecting the optimized nanoparticles into mice and imaging the signal change in brain using MRI at time points after injection selected based on the PK modeling. Similarly, the radiological-pathological correlations between in vivo imaging findings and ex vivo histology results will be studied at

time points selected based on the model results.

3.6 Conclusions

This study investigated the PK of two VHHs and two VHH-conjugated iron oxide nanoparticles for their in vivo biodistribution and clearance in mice. A near-infrared method was established to monitor and record VHHs and VHH-IONPs kinetics in vivo. These results build a foundation for efficient understanding of VHHs and VHH-IONPs biodistribution and pharmacokinetics using near-infrared imaging.

Chapter 4: Selection of Single Domain Anti-Transferrin Receptor Antibodies for Blood-Brain Barrier Transcytosis Using a Neurotensin Based Assay and Histological Assessment of Target Engagement in a Mouse Model of Alzheimer's Disease-Related Amyloid-Beta Pathology

4.1 Abstract

Background: The blood-brain barrier (BBB) presents a major obstacle in developing specific diagnostic imaging agents for many neurological disorders. In this study we aimed to generate single domain anti-mouse transferrin receptor antibodies (anti-mTfR VHHs) to mediate BBB transcytosis as components of novel MRI molecular contrast imaging agents.

Methods: Anti-mTfR VHHs were produced by immunizing a llama with mTfR, generation of a VHH phage display library, immunopanning, and in vitro characterization of candidates. Site directed mutagenesis was used to generate additional variants. VHH fusions with neurotensin (NT) allowed rapid, hypothermia-based screening for VHH-mediated BBB transcytosis in wild-type mice. One anti-mTfR VHH variant was fused with an anti-amyloid-beta (Aβ) VHH dimer and labeled with fluorescent dye for direct assessment of in vivo target engagement in a mouse model of AD-related Aβ plaque pathology.

Results: An anti-mTfR VHH called M and variants had binding affinities to mTfR of <1nM to

1.52nM. The affinity of the VHH binding to mTfR correlated with the efficiency of the VHH-NT induced hypothermia effects after intravenous injection of 600 nmol/kg body weight, ranging from undetectable for nonbinding mutants to -6°C for the best mutants. The anti-mTfR VHH variant M1P96H with the strongest hypothermia effect was fused to the anti-Aβ VHH dimer and labeled with Alexa647; the dye-labeled VHH fusion construct still bound both mTfR and Aβ plaques. However, after intravenous injection at 600 nmol/kg body weight into APP/PS1 transgenic mice, there was no detectible labeling of plaques above control levels. Thus, NT-induced hypothermia did not correlate with direct target engagement in cortex.

Conclusions: There was a surprising dissociation between NT-induced hypothermia, presumably mediated by hypothalamus, and direct engagement with Aβ-plaques in cortex. Alternative methods to assess anti-mTfR VHH BBB transcytosis will need to be developed for anti-mTfR VHH screening and the development of novel MRI molecular contrast agents.

4.2   Background

Alzheimer's disease (AD) is one of the most important causes of dementia in the elderly[6]. About 6.2 million Americans are living with AD, and it's predicted that the number will increase to 13.8 million by 2050 [7]. With no effective therapies to cure or inhibit significant AD symptom progression[8], AD severely decreases patients' quality of life and creates an enormous burden on the health care system and society [6, 9]. Currently, clinical AD diagnosis is based on cognition and the relative impact of impairments on daily activities [10]. However, multiple neurodegenerative and vascular pathologies can coexist and produce cognitive and behavioral symptoms which could overlap with each other [11]. This makes it difficult to accurately identify pathology based solely on clinical symptoms. The accuracy of clinical diagnosis of AD at the National Institute of Aging and National Institute of Aging sponsored

AD centers varies depending on the clinical and neuropathologic criteria used [12]. The sensitivity of AD diagnosis ranges from 70.9% to 87.3%, whereas specificity ranges from 44.3% to 70.8%, which need to be improved. AD has a very long prodrome stage before clinically observable symptoms [114]. Early diagnosis is preferred to help with early intervention and the development of preventive therapeutics to slow AD development [10]. Detection of patients in the preclinical stages of AD can also help to provide diagnostic information, monitor disease progression, and even monitor the effect of newly developed treatment methods. Imaging methods including MRI and PET have been developed to aid the diagnosis of AD [13, 14]. However, PET imaging for AD provides limited resolution and requires radiation exposure. Structural MRI lacks specificity and does not allow direct visualization of Aβ or tau, the histological hallmarks of AD. There is an unmet need for developing methods like molecular contrast MRI which have better resolution than PET and better specificity than structural MRI imaging.

The blood-brain barrier (BBB) represents a significant obstacle in delivering diagnostic and therapeutic agents to the central nervous system (CNS), preventing uptake of more than 98% of potential neurotherapeutics to brain [32-35]. The BBB consists of endothelial cells held together by tight junctions which hinder paracellular passage. Most molecules do not transfer from blood to brain through the BBB, which protects the brain from toxicity and maintains brain homeostasis. Several methods have been developed to improve the transport of diagnostic and therapeutic agents into the CNS. For instance, the BBB may be temporarily opened by administration of hypertonic agents or focused ultrasound. Alternatively, very high doses of an agent can be given so that even if a small fraction enters the brain the desired effect will be achieved. In some cases, direct injection of agents into the cerebrospinal fluid can be

employed [35]. However, these methods are invasive and have a risk of causing infection, toxicity, and neurological dysfunction [34, 35].

BBB crossing based on receptor mediated transcytosis (RMT) is potentially especially promising. The use of protein shuttles has the potential to facilitate the transport of therapeutic agents across the BBB using specific endogenous receptor systems. Candidate receptor systems including transferrin receptors (TfR), low-density lipoprotein receptors, insulin receptors and neuropeptide receptors are highly expressed on the BBB where they mediate receptor-mediated transcytosis [34]. Among the different receptors, TfR has been widely used for transporting macromolecules across the BBB [36, 37]. Based on the study of Yu et al., there is a nonlinear relationship between an antibody's affinity for TfR and its uptake in brain. At tracer doses, antibodies with higher affinity to TfR have higher uptake into the brain, while at therapeutic doses, antibodies with lower affinity to brain have higher uptake into the brain [40]. The effect of TfR affinity on brain uptake has been confirmed by the study of Wiley et al [115]. Transferrin conjugated gold nanoparticles with high avidity to TfR remain strongly attached to brain endothelial cells and reduced accumulation in brain parenchyma compared with nanoparticles with lower avidity to TfR [115]. Thus, to achieve optimal brain uptake, it is important to optimize anti-TfR concentration and antibody affinity to TfR. Jefferies et al. identified a monoclonal antibody OX-26 specific for transferrin receptors [38]. This antibody was tested and was confirmed to be able to facilitate TfR-mediated transcytosis across BBB [39]. Yu et al. generated a bispecific antibody that binds to TfR for transcytosis and also to the enzyme β-secretase for inhibiting Aβ production[40]. However, the existing anti-TfR antibodies have relatively large size, especially when conjugated to additional components for RMT or other payloads such as imaging contrast agents. Also, it is expensive to engineer and

synthesize monoclonal antibodies, which are typically produced in mammalian cell culture. Thus, there is an unmet need for smaller, less expensive, and easier to engineer system for BBB transcytosis.

Camelids produce functional antibodies devoid of light chains called heavy chain-only antibodies (HCAbs) [48, 49]. HCAbs recognize their cognate antigens by one single domain, the variable domain (VHH). The VHH in isolation is very small compared with other antibodies. The molecular weights of VHHs are typically ~15kDa, which is about 1/10 of the molecular weight of a conventional IgG and about half the molecular weight of a single chain variable fragment (Scfv) [49, 50]. VHHs have affinities at the same order of magnitude as conventional IgGs, often in the nanomolar or subnanomolar range [53]. Because of their small size, VHHs can also bind to epitopes not recognized by conventional antibodies and can have better tissue penetration capacities [51, 52]. Caplacizumab was the first VHH approved by FDA for treatment of acquired thrombotic thrombocytopenic purpura in humans [116]. There are several more VHHs which are in clinical trials, with safety profiles similar to other antibody therapeutics in humans [117, 118]. Importantly, VHHs have been found that can facilitate BBB penetration and allow brain target binding. The use of VHHs for BBB transcytosis and target engagement is promising. Specifically, Stanimirovic et al. identified an insulin-like growth factor 1 receptor binding VHH which crosses the BBB by receptor mediated transcytosis [54, 55]. Danis et al. identified and optimized VHHs to mitigate brain accumulation of pathological tau in a tauopathy mouse model [56]. Dupre et al., identified VHHs which could be used to detect tau in transgenic mice brain tissues [57]. However, the extent to which VHHs that engage in receptor mediated transcytosis using the TfR can carry diagnostic and therapeutic payloads across the BBB still has not been assessed. Here we tested

the hypothesis that VHHs that bind to TfR and cross the BBB through RMT in mice could be coupled with additional VHHs that bind to amyloid plaques as a proof of concept for a platform which could be generalized to other neurological diseases.

Current methods to evaluate BBB crossing require substantial resources and can be time-consuming [40, 41]. An efficient way to screen for BBB crossing in vivo would be helpful since in vitro models may not be fully predictive of in vivo results. Neurotensin (NT) is a 13 amino acid peptide first identified by Carraway and Leeman in 1973 from bovine hypothalamic extracts [42]. NT is expressed in CNS as well as in peripheral tissues, mostly in the gastrointestinal tract. NT is involved in regulating appetite, nociception, and thermoregulation in the CNS, and alters nutrient absorption, gastrointestinal motility, and secretion in the peripheral gastrointestinal tract [43]. It was found that NT induces rapid and transient hypothermia in mice and rats when injected to CNS [44, 45]. The hypothermia was likely to be due to effects in hypothalamus. Young & Kuhar found that NT receptors had moderate to high densities in hypothalamus [119]. Injection of NT to medial, lateral preoptic area and anterior parts of hypothalamus induced the hypothermia effect [119]. Meanwhile, intravenously injected NT does not typically cause hypothermia [46]. On the other hand, when NT-conjugated mouse TfR (mTfR)-binding VHHs were injected intravenously to mice, the NT-mTfR VHH conjugates induced hypothermia in mice, presumably because they get across the BBB and bind to NT receptors in hypothalamus [41, 47]. These properties of the NT system make it an apparently attractive assay platform for rapid testing of VHH BBB transcytosis.
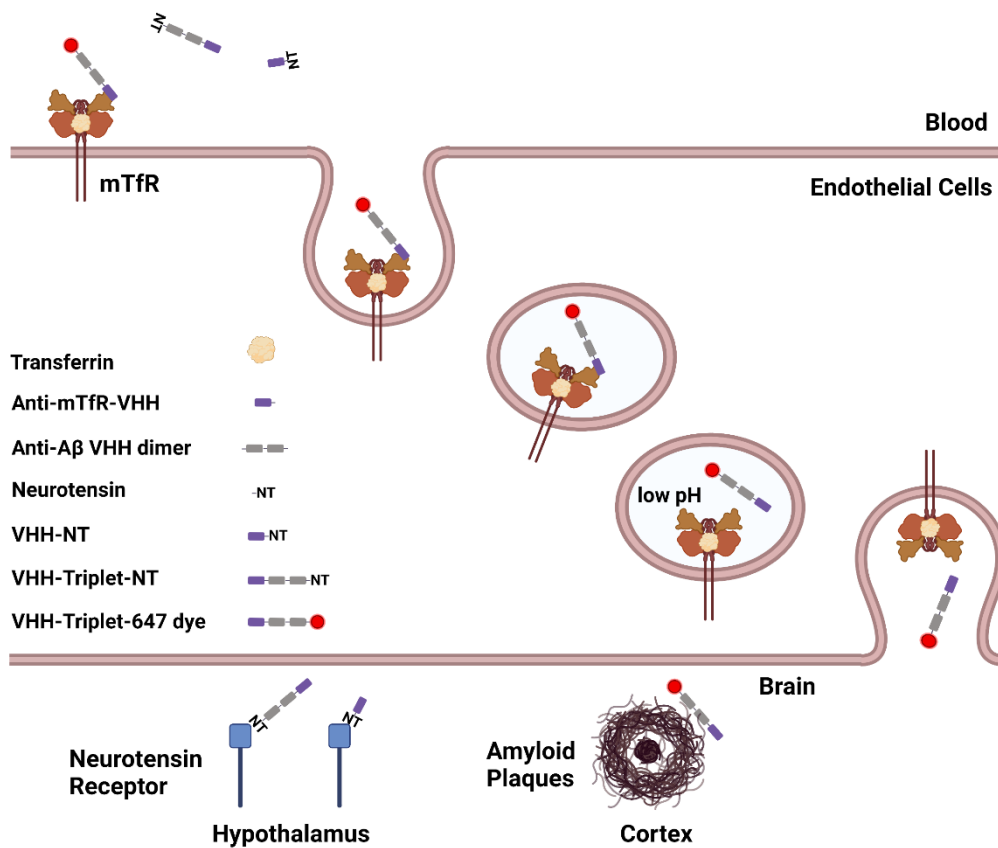
Figure. 4.1. Schematic of the modular system for VHH-mediated BBB transcytosis and target engagement. Module 1: anti-mTfR VHH for RMT across BBB. Module 2: neurotensin peptide (NT) for rapid assessment of in vivo target engagement via measurement of hypothermia. Module 3: anti-Aβ VHH dimer for disease-relevant target engagement in brain parenchyma. Module 4: 647 dye for visualization of VHH constructs in situ. The anti-mTfR VHH was combined with NT for anti-mTfR VHH screening through monitoring hypothermia effect. The anti-mTfR VHH were combined with VHH dimer and NT or 647 to test the effect of anti-mTfR VHH together with other components of the module. This schematic figure also shows the TfR mediated transcytosis across BBB. The anti-mTfR VHH conjugates binds to TfR on the endothelial cells which comprise a major portion of the BBB. Then the TfR-VHH complex is endocytosed across the endothelial cells in the endosomes. VHHs dissociate from the TfR-VHH complex with decreased pH level in endosome and are released on the brain side of the BBB. There were two different targets in the brain parenchyma in this study, the NT receptor in hypothalamus and amyloid plaques in cortex and hippocampus. (Figure generated using BioRender.com)

Here, we independently generated additional mTfR-binding VHHs and used a similar NT based modular system to screen these VHHs for mTfR-mediated BBB transcytosis (Figure. 4.1). We hypothesized that this modular screening system can be used to identify and optimize anti-mTfR VHHs for BBB transcytosis and brain target binding.

This screening system includes four modules. The first module is an anti-mTfR VHH for receptor mediated transcytosis across the BBB; the second module is the neurotensin peptide for assessment of target engagement in vivo through measurement of hypothermia. The third module is a dimer of anti -Aβ VHHs for disease-relevant brain target engagement. The fourth module is a fluorescence dye for visualization of VHH constructs in situ. We tested different VHH variants and found one variant which showed good BBB penetration based on this screening system. The VHH variant with the best BBB transcytosis ability fused to a tandem VHH dimer called Nb3-Nb3 which binds to amyloid plaques in brain parenchyma. This VHH triplet was conjugated to a fluorescent dye and post-mortem confocal microscopy was performed to directly evaluate brain target engagement.

4.3 Methods

4.3.1 Immunization of llama with mouse transferrin receptor

A single adult male llama (Lama glama) was immunized under contract agreement through Triple J Farms (Kent Laboratories, Bellingham, WA) following the method previously described [68]. Briefly, subcutaneous injections of 100 µg ectodomain (Cys89-Phe763) mTfR (50741-M07H, SinoBiological) were performed with protein emulsified with complete Freund's adjuvant on day 0, followed by additional 100 µg immunizations emulsified with incomplete Freund's adjuvant on days 14, 28, and 42. On day 49, peripheral blood was drawn for peripheral blood mononuclear cell (PBMC) isolation. Triple J Farms operates under established National Institutes of Health Office of Laboratory Animal Welfare Assurance certification number A4335-01 and United States Department of Agriculture registration number 91-R-0054.

4.3.2 Generation of VHH immune phage display library

The generation of an immune phage display library and isolation of mTfR binding VHH clones

was performed using the methods previously described [68]. Briefly, total RNA extracted from

PBMCs was used for synthesis of first-strand complimentary DNA (cDNA) using the

SuperScript IV First-Strand Synthesis kit (#1891050, Invitrogen). The heavy-chain variable

domain was then amplified from the cDNA using Q5 high-fidelity DNA polymerase (New

England Biolabs) with the described primers (CALL001: 5′-

GTCCTGGCTGCTCTTCTACAAGG-3′ and CALL002: 5′-

GGTACGTGCTGTTGAACTGTTCC-3'). The heavy-chain specific amplicon was isolated

using electrophoresis with low-melting point agarose extraction with the QIAquick Gel

Extraction kit (Qiagen). A secondary amplification was performed using a modification of the

primers (VHH-Esp-For: 5′-

CCGGCCATGGCTGATGTGCAGCTGCAGGAGTCTGGRGGAGG-3′ and VHH-Esp-Rev:

5′-GTGCGGCCGCTGAGGAGACGGTGACCTGGG T-3′) used by Pardon et al. to facilitate

cloning into the phagemid pHEN2 [120]. The amplified sequences were cleaved with the

restriction endonucleases NcoI and NotI (New England Biolabs) and subsequently ligated into

compatibly cleaved pHEN2 phagemid at a 3:1 (insert:phagemid) ratio overnight at 16°C

followed by purification. The resulting ligation mixture was electroporated into TG-1 phage-

display competent cells (#60502-1, Lucigen) and plated onto 2xYT agar containing 100 μg/mL

carbenicillin and 2% (w/v) glucose at 37°C overnight. The resulting library contained > 107

independent clones. Phage was produced for screening using the M13KO7 helper phage

(#18311019, Invitrogen) followed by precipitation by addition of one-fifth volume 20%

polyethylene glycol 6000 / 2.5 M sodium chloride solution on ice and centrifugation to purify

the phage particles.

4.3.3 Immunopanning and clone screening

Selection of mTfR specific VHH was performed using direct binding of phage to immobilize

mTfR. Standard radioimmunoassay (RIA) tubes were coated with 500 µL mTfR solution at 5

µg/mL in sodium carbonate buffer, pH 9.6 overnight at 4°C. The coating solution was

removed, and the RIA tube filled with a 2% (w/v) non-specific blocking solution (bovine

serum albumin or nonfat dry milk) in 1x Phosphate Buffered Saline (PBS). Amplified phage

(~1011 phage) was mixed with blocking solution to a final volume of 500 µL and then

transferred into the RIA tube to allow for association at room temperature and 600 rpm mixing.

The RIA tube was then washed 20 times with 1x PBS and then the bound phage eluted with

100 mM triethylamine solution for 20 mins. The eluted phage solution was neutralized with

1:10 volume 1 M Tris-HCl, pH 8.0. The eluted phage was amplified in TG-1 cells and a

second round of immunopanning was performed.

Following the second round of immunopanning, individual colonies were selected and cultured

in 96-well blocks containing 2xYT containing carbenicillin at 37°C with 300 rpm shaking for

4-6 hours. Expression of VHH was induced by addition of isopropyl-beta-D-thiogalactoside

(IPTG) to a final concentration of 1 mM and incubation overnight at 37°C. The culture blocks

were centrifuged to pellet the cells and frozen at -80°C for 1 hour following removal of the

culture supernatant. The culture block was then equilibrated to room temperature and 500 µL

1xPBS added to each well followed by shaking at 1500 rpm to resuspend the cell pellets and

allow for release of VHH from the cells. The culture block was centrifuged for 20 min at

2000xg. Nunc Maxisorp plates were coated with mTfR at 1 µg/mL as described above and

blocked with 1% bovine serum albumin (BSA). The clarified VHH supernatants were incubated on the mTfR plates for 1 hour at room temperature. The assay plate was washed and peroxidase conjugated goat anti-alpaca VHH domain specific antibody (#128-035-232, Jackson ImmunoResearch) at 0.8 µg/mL was transferred to the plate and incubated for 1 hour at room temperature. Following a final wash, the assay was developed by addition of tetramethylbenzidine (#T5569, Sigma-Aldrich) and absorbance was measured at 650 nm on a Biotek Synergy 2 plate reader. Clones with absorbance values greater than two standard deviations above background were considered of interest and subsequently sequenced.

4.3.4 Amyloid beta specific VHH production

Paraschiv et al. previously reported the isolation of amyloid beta binding VHH clones [121]. We selected the sequence for the named Nb3 clone for use in this study. The Nb3 amino acid sequence was imported into SnapGene software (GSL Biotech LLC) and reverse translation performed using preferred codon usage for expression in E. coli. Additional sequence, including a (Gly-Gly-Gly-Ser)$_3$ between VHH domains, was incorporated for cloning into pHEN2 as a tandem dimer as part of the heterotrimer clones synthesized with TfR binders. To reduce the potential for recombination events, the DNA sequence was manually curated to adjust the codon usage and reduce the frequency of repetitive sequence within the Nb3-Nb3 dimer. The affinity of the Nb3-Nb3 dimer was measured using bio-layer intergerometry as described below.

4.3.5 Bio-layer interferometry (BLI) assessment of VHH binding kinetics

The binding kinetics of the selected VHH clone against mTfR and Aβ was assessed by BLI. For measurements of mTfR kinetics, biotinylated VHH was diluted into assay buffer at 1 µg/mL and immobilized onto streptavidin coated biosensors (#18-5019, Sartorius) to a

minimum response value of 1 nm on the Octet Red96 System (Sartorius). For measurements of amyloid beta, beta-amyloid(1-40)-Lys(biotin-LC) (AS-23517, Anaspec), was diluted into assay buffer at 1 µg/mL and immobilized onto streptavidin coated biosensors (#18-5019, Sartorius) to a minimum response value of 1 nm on the Octet Red96 System (Sartorius). Purified mTfR or VHH clones were diluted into assay buffer at the specified concentrations. The immobilized antigen biosensors were allowed to associate at 37C° followed by dissociation in the baseline buffer well location. All assays included a background correction condition to allow for sensor normalization. The ForteBio Data Analysis suite was used to normalize the association curves following background subtraction and Savitzky-Golay filtering. Curve fitting was applied using global fitting of the sensor data and a steady state analysis calculated to determine the association and dissociation constants. All assay steps were prepared in Greiner 96-well plates (#655209) in a volume of 300 µL. Assay buffer was defined as 0.1% BSA (w/v) in 1xPBS.

4.3.6 Synthesis and expression of VHH constructs

Based on the methods described in **Immunopanning and clone screening** and **BLI assessment of VHH binding kinetics** sections, we synthesized several neurotensin-fused VHH monomers with different binding affinities to mouse transferrin receptor. In addition, we produced single polypeptide VHH heterotrimers that consisted of $M1_{P96H}$, a (Gly-Gly-Gly-Ser)$_3$ linker, Nb3, a (Gly-Gly-Gly-Ser)$_3$ linker, and Nb3 using the method described in **Amyloid beta specific VHH production**. The VHH dimer Nb3-Nb3 binds to amyloid plaques in brain parenchymal of APP/PS1 mice. These constructs were termed "M1$_{WT}$-NT", "M1$_{P96H}$-NT", "M1$_{AA}$-NT", "M1$_{R100dH}$-NT" and "M1$_{P96H}$-triplet". The VHH naming convention for P96H and R100dH are based on the Kabat nomenclature and refer to the specific amino acid residue

modification positions within the VHH sequence [122]. Another neurotensin fusion with a VHH generated against human TfR, which does not bind mouse TfR called "H1-NT," was used as control. All VHH constructs were designed using SnapGene Software and synthesized (Twist Bioscience) with corresponding restriction endonuclease sites for direct cloning into pHEN2. Sequence confirmed pHEN2 clones with the various constructs were transferred into BL21(DE3) competent E. coli cells (C2527I, New England Biolabs). Transformed cells were grown in terrific broth medium containing carbenicillin at 37°C and 300rpm shaking in baffled flasks. Once the culture density reached an optical density equal to 0.6, IPTG was added to a final concentration of 1mM to induce protein expression. For monomer VHH expression the post-induction incubation temperature was maintained at 37°C but reduced to 30C for the $M1_{P96H}$-triplet. Following overnight expression, cells were pelleted by centrifugation and VHHs were extracted through osmotic shock and recovery of the periplasmic fraction [68, 84]. Clarified periplasmic fraction was purified using HisPur™ Ni-NTA Resin (88222, Thermo Fisher Scientific) column chromatography. The eluted VHH proteins were further purified by size-exclusion chromatography (SEC) over a Superdex75 10/300 column on an AKTA Pure (Cytiva). Protein purity was assessed by SDS-PAGE on a 10% Bis-Tris MES acrylamide gel and found to be >95% pure.

$M1_{P96H}$-triplets and H1-triplets were fluorescently labeled with using Alexa Fluor™ 647 succinimidyl ester dye to allow fluorescence confocal microscopy of tissue sections. The triplets were incubated with the succinimidyl ester dye for 1 hour in 50mM sodium carbonate buffer, pH 9.6 and purified by desalting using a 5mL HiTrap desalting column in-line with the AKTA Pure. The binding fidelity of the VHH heterotriplet was assessed by ELISA against mTfR. The fluorescence dye labeled $M1_{P96H}$-triplet and H1-triplet were named "$M1_{P96H}$-triplet-

647" and "H1-triplet-647"

4.3.7 Endotoxin removal

Removal of contaminating endotoxin was achieved using High-Capacity Endotoxin Removal Resin (88270, Pierce) from the VHH preparations. A volume of 0.25ml endotoxin removal resin was added to 1ml of VHH sample. The VHH and resin were mixed for 2hr at room temperature to allow for absorption of endotoxin. The mixture was centrifuged to pellet the resin and the supernatant collected. A volume of 0.25ml fresh endotoxin removal resin was added to the first-pass solution and mixed for another 2hr at room temperature. Following a final centrifugation to pellet the resin, the solution was collected for endotoxin level testing. Endotoxin levels were measured using the Chromagenic Endotoxin Quant kit (A39552, Pierce) according to the manufacturers protocol to ensure a level of endotoxin <0.5 endotoxin units/mg of total protein.

4.3.8 Binding assessment of histidine mutations by ELISA

To determine the effect on histidine mutation introduction, an ELISA was performed with the post VHH binding wash buffer at normal and reduced pH. Nunc Maxisorp plates were coated with mTfR at 1 µg/mL in 50mM sodium carbonate, pH 9.6 overnight at 4°C. The plates were blocked with 1% BSA in 1xPBS buffer and then triplicate dilutions of each VHH prepared in 0.5% BSA in 1xPBS buffer and transferred to the plate. Binding at room temperature for 2 hours was followed by three cycles of 5-minute washes with either 1xPBS, pH 7.2 or 1xPBS, pH 5.5. Following the pH dependent wash step, the bound VHH was detected with peroxidase conjugated goat anti-alpaca VHH domain specific antibody (#128-035-232, Jackson ImmunoResearch) at 0.8 µg/mL incubated for 1 hour at room temperature. Following a final wash, the assay was developed by addition of tetramethylbenzidine (#T5569, Sigma-Aldrich),

the reaction was terminated by addition of 50 µL 1M hydrochloric acid and absorbance was measured at 450 nm on a Biotek Synergy 2 plate reader.

4.3.9 Animals

All animal experiments were conducted under protocols approved by the National Institute of Neurological Disorders and Stroke (NINDS)/ National Institute on Deafness and Other Communication Disorders (NIDCD) Animal Care and Use Committee in the National Institutes of Health (NIH) Clinical Center. C57BL/6J female mice were purchased from Jackson labs at 6-7 weeks of age and used at 7-12 weeks of age. Fifteen mice were divided into five groups with three mice in each group to test the five VHH-NT fusions. Anesthetized mice were injected via tail vein with VHH-NT fusions: $M1_{WT}$-NT, $M1_{P96H}$-NT, $M1_{AA}$-NT, $M1_{R100dH}$-NT and H1-NT for screening. Experiments were performed at the same time each day. Three mice were injected with VHH triplet-NT to assess the ability of VHH triplet-NT to get across the BBB. To confirm the result from the five VHH-NT fusions, a blinded replication experiment was performed with additional fifteen mice randomized using a random number generator into five groups with three mice in each group.

APP_{SWE}/PSEN1dE9 (MMRRC Strain #034832) positive transgenic mice were purchased from Jackson labs [123, 124], maintained on a hybrid (C57BL/6xC3H) background, and raised under protocols approved by the National Institute of Neurological Disorders and Stroke (NINDS)/ National Institute on Deafness and Other Communication Disorders (NIDCD) Animal Care and Use Committee in the National Institutes of Health (NIH) Clinical Center. Ten transgenic mice ages between 13-15 months, eight males and two females, were randomly assigned to two groups. Five mice were injected with $M1_{P96H}$-triplet-647 and five mice were injected with H1-triplet-647.

Injection of VHH-NTs and VHH-triplet-647s

Mice were anesthetized with 60% oxygen/ 40% medical air gas mixture containing 5% isoflurane in an induction box. After a stable anesthesia plane was established, mice were maintained at 1.5-2% isoflurane level. Artificial tears ointment was applied to prevent eye injury due to drying. Mice were placed on an electrical heating pad to maintain body temperature at 37°C. The VHH-NTs, $M1_{WT}$-NT, $M1_{P96H}$-NT, $M1_{AA}$-NT, $M1_{R100dH}$-NT and H1-NT were injected into wild-type C57BL/6J mice through the tail vein using a 30 Gauge needle in a single bolus at a dose of 600nmol/kg body weight in 1xPBS. The VHH-triplet-647s, $M1_{P96H}$-triplet-647 and H1-triplet-647, were injected intravenously through single bolus injection at a dose of 1000nmol/kg body weight. Mice were maintained under anesthesia for approximately 2-3 minutes. Following the procedure, the mice were allowed to recover on a heating pad until fully ambulatory and then returned to their home cage with immediate access to food and water.

4.3.10 Temperature measurement

Infrared thermometry was used for temperature measurement using an infrared thermometer (Model# 62 MAX+, Fluke). Abdominal fur was removed by application of topical depilatory cream prior to temperature measurement for precise data collection. Baseline temperature was measured three times before intravenous (IV) injection with a time interval of 30min between measurements. Then, mouse temperatures were measured at the time intervals of 30min, 1hr, 1.5hr, 2hr, 2.5hr, 3hr, 3.5hr, 4hr, 4.5hr and 5hr after injection. All temperature measurements were performed by investigators blinded to the identity of the injected VHH sample. Mice were briefly anesthetized (<20 seconds) with isoflurane for each temperature measurement. In preliminary experiments we confirmed that this brief anesthesia did not affect temperature.

4.3.11 Confocal microscopy of mice brains injected with triplet-647

Two hours post IV injection mice were sacrificed under isoflurane anesthesia by cardiac perfusion with 1X PBS + Heparin (10 units Heparin per milliliter 1X PBS). Following perfusion, mice were decapitated using a pair of sharp surgical shears and the brain was carefully excised from the cranium. Brains were fixed in 4% PFA for 24hrs then equilibrated in 30% sucrose for 48 hours. Then, mouse brains were sectioned at 50 µm thickness using a freezing sliding microtome. Staining was performed to visualize amyloid plaques using the Congo Red derivative X34.[125] Tissue was rinsed with 1xPBS two times. Then, tissues were incubated in 40%EtOH/60%PBS at pH10 containing 10 µM X34 (SML1954-5MG, Sigma) for 10min. After X34 incubation, tissue was rinsed with milliQ water five times then differentiated in 40%EtOH/60%PBS at pH10 for 2min. After differentiation, the tissue was rinsed with miliQ water for 10min then mounted onto positively charged slides (EF15978Z, Daigger®). The mounted tissue sections were allowed to dry overnight at room temperature and cover slipped using fluoromount-G (00-4958-02, Invitrogen™).

To objectively evaluate the effect of intravenous injection of $_{M1P96H}$-Triplet-647 and H1-Triplet-647 on APP/PS1 mice, brain sections at around 2.5mm posterior to bregma were selected for confocal fluorescence imaging. The brain sections were equally divided into 10 parts in both horizontal (x) and vertical (y) directions (Figure. 4.2). X and y coordinates were
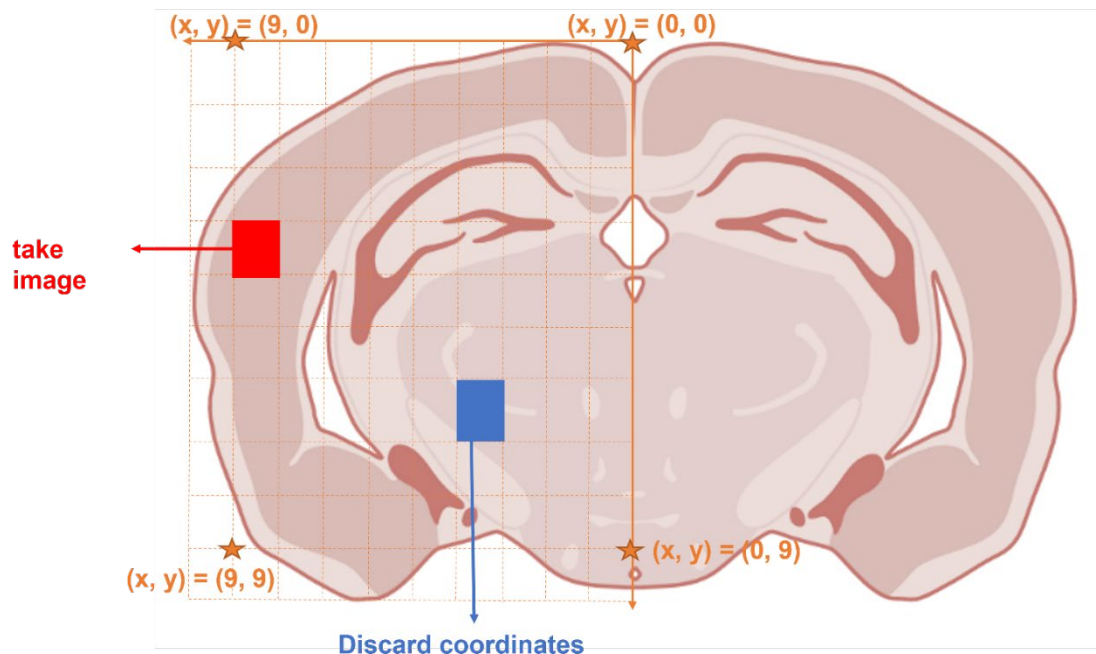
Figure 4.2. Schematic graph for the manual unbiased random selection method for confocal image acquisition. This schematic graph shows the logic of picking coordinates for confocal images acquisition. The right hemisphere of the brain was equally divided into ten parts in both x and y directions. (x, y) coordinates were randomly generated using a random number generator. The microscope stage was moved to the target (x, y) coordinates using the stage rulings. When (x, y) coordinates fell into the areas of cortex, images were taken and cropped to include only cortical areas. When (x, y) coordinates fell out of the cortex the coordinates were discarded and no images were taken. Source of the mouse brain: biorender.com

randomly selected using by random numbers from 1 to 10. When (x, y) coordinates fell onto a cortical area, stacks of images were taken which covered 16μm depth (z direction) starting from the top of the brain section. When (x, y) coordinates fell outside of the cortex, the microscope was moved to the next randomized (x, y) coordinates without taking images. Brain sections were imaged using a Zeiss LSM 510 microscope. Stacks of images were acquired with eight images per stack and 2μm optical thickness at 20x magnification using a Zeiss Plan-

Apochromat 20x/0.8NA lens. Images were acquired using laser wavelength at 633nm to visualize the VHH triplets conjugated with 647 dye and 405 nm wavelength laser to visualize the X-34 dye. For 647 channel images, laser at wavelength 633nm was used with a LP650 filter and laser power set to be at transmission 100%. For X34 channel images, laser at wavelength 405nm was used with a BP420-480 filter and laser power set to be at transmission 15%. The images were exported in lsm file format for image analysis using ImageJ.

Fluorescent confocal microscopy - Naïve brain as controls

Naïve APP/PS1 positive mouse brain sections stained only with X-34 for fluorescence confocal microscopy were used as a negative control. Naïve APP/PS1 positive mouse brain sections stained with both X34 and ex vivo M1$_{P96H}$-Triplet-647 for fluorescence confocal microscopy were used as a positive control. For ex vivo M1$_{P96H}$-Triplet-647 staining, naïve brains were sectioned and washed in 1XPBS. Sections were incubated in 3% normal donkey serum for 30min to block non-specific binding. After blocking, tissue sections were incubated overnight at 4C° in M1$_{P96H}$-Triplet-647 at a concentration of 10ug/ml in blocking solution. Tissues were then washed in 1xPBS three times followed by X34 staining as described.

4.3.12 Automated image analysis

To quantitatively analyze the confocal microscope images, thresholding and particle analysis were performed to remove background signals and isolate target structures of interest. The percent area of X34 stained amyloid plaques was quantified with thresholding at (0, 30) followed by Particle analysis. To remove low signal background, 647 channel image thresholding was set at 0-1000. Then the 647 channel images was analyzed with particle analysis. The parameters for particle analysis were set to be 0-1000 pixels for size and 0.1-1.0 for circularity. The parameters for thresholding and particle analysis were determined through

testing of different parameters to capture the qualitative morphology of amyloid plaques as assessed by experienced investigators. Amyloid plaque levels were represented as % area of X34 coverage and VHH triplet-647 entry into the brain parenchyma was represented as % area of Alexa 647 dye coverage in the areas with X34 staining. Because there is mouse-to-mouse variability in plaque size and X34 staining intensity, we analyzed the ratio of the Triplet-647 coverage to X34 coverage.

4.3.13 Statistical analysis

Unpaired student t-test were performed to evaluate the differences between the transcytosis ability of M1$_{P96H}$-triplet-647 and H1-triplet-647 to amyloid plaques in APP/PS1 transgenic mice brains. Graphs were created using Prism. Sample sizes were based on availability of transgenic mice and previous experiments. No formal power calculations were performed.

4.4 Results

4.4.1 Endotoxin removal

VHHs contamination by endotoxins is a byproduct of expression in E. Coli cells [126]. Endotoxin can induce systemic inflammation and cause disruptive BBB changes [127]. It was found that the excess endotoxin level in VHH-NT fusions can cause additional hypothermia
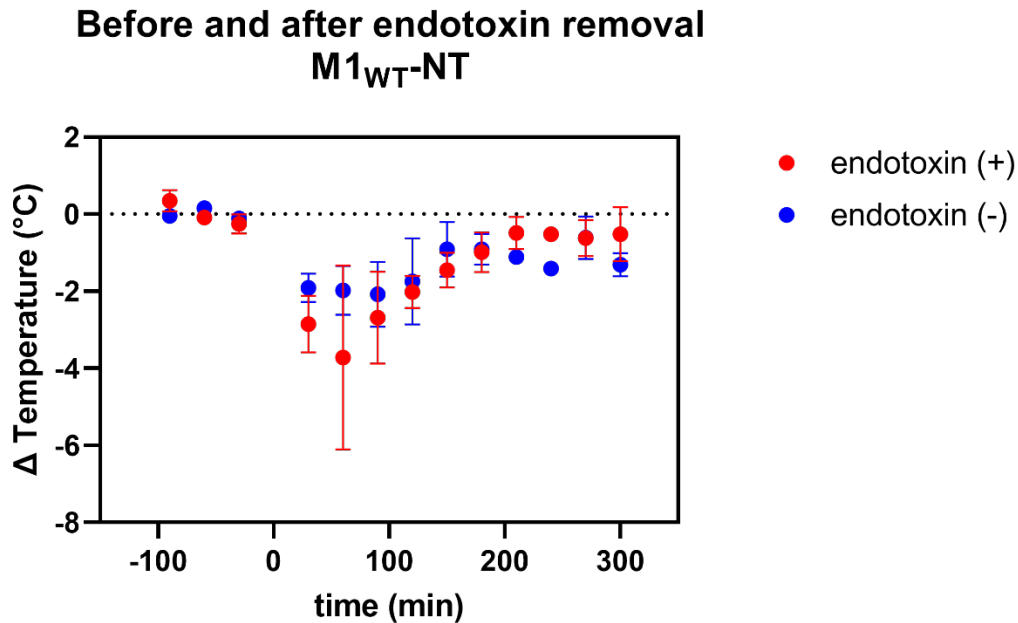
Figure 4.3. The hypothermia effect of M1$_{WT}$-NT before and after endotoxin removal. Endotoxin removal from in M1$_{WT}$-NT preparations from E. coli decreased hypothermia effects at time 30min, 1hr and 1.5hr after IV injection of the M1$_{WT}$ -NT (n= 3 per group). The maximum hypothermic effect of 600nmol/kg body weight of M1$_{WT}$ -NT was approximately 2C° less after endotoxin removal.

(Figure. 4.3). To avoid potential hypothermia effects caused by endotoxin, endotoxin was removed after purification. After endotoxin removal, the level of endotoxin level in VHHs was less than 0.1 endotoxin unit/ml (EU/ml) within normal range [128].

4.4.2 Anti-mTfR VHH variant screening based on binding affinity measurement
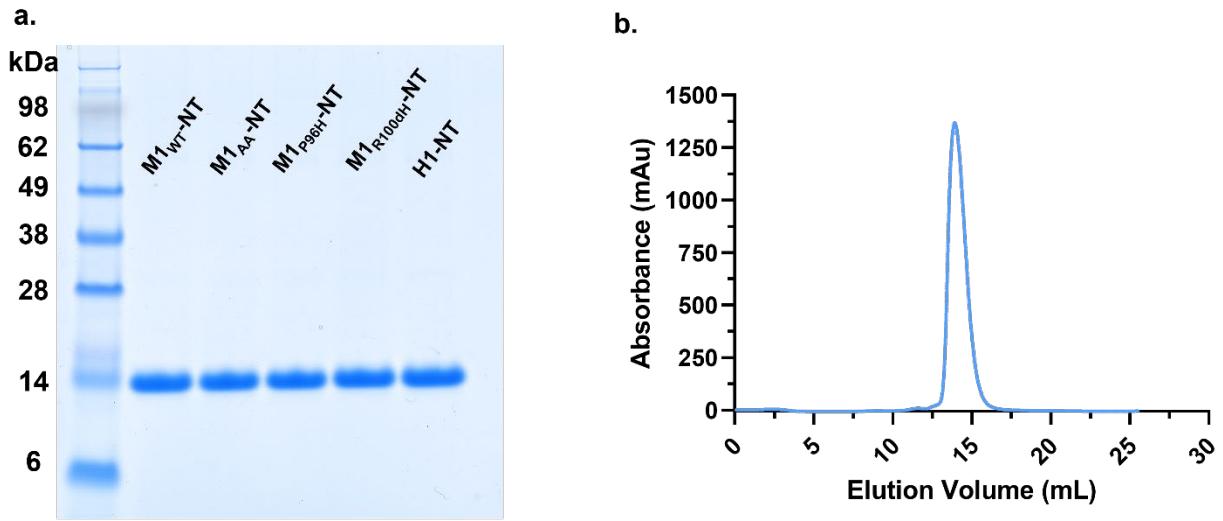
Figure 4.4. Post purification assessment of the five VHH-NT fusions M1$_{WT}$-NT, M1$_{P96H}$-NT, M1$_{AA}$-NT, M1$_{R100dH}$-NT and H1-NT. The purity of the monomer VHH by (a.) SDS-PAGE gel and exemplar (b.) size-exclusion chromatography over a Superdex75 column for M1$_{WT}$-NT indicating >95% purity and homogeneity of the material.
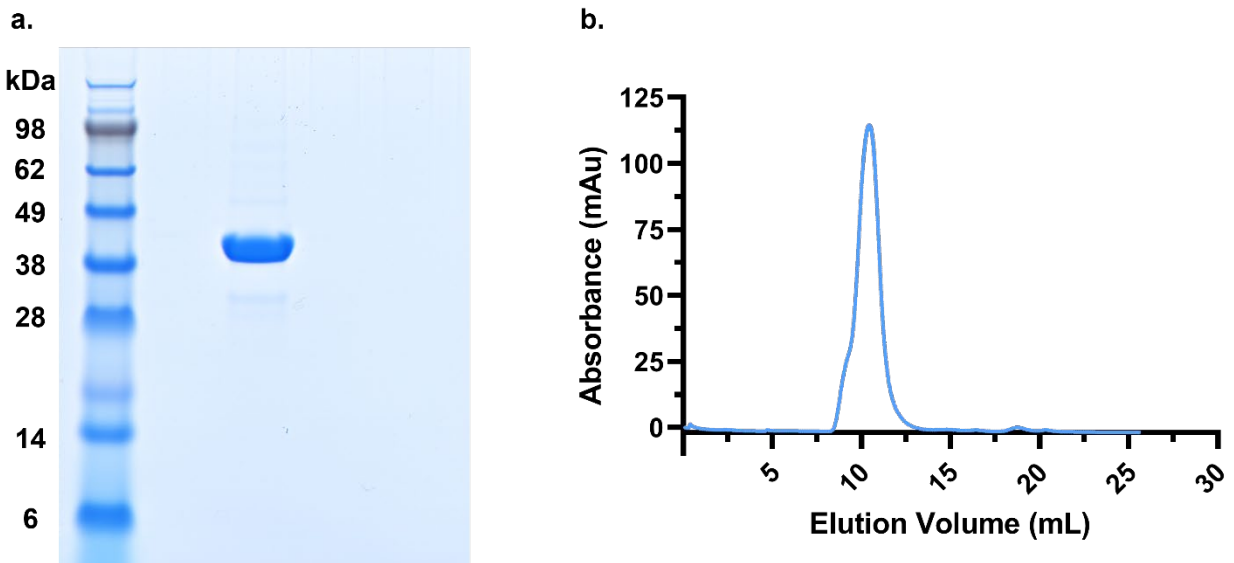
Figure 4.5. Post purification assessment of M1$_{P96H}$-triplet-NT. The purity of the triplet VHH by (a.) SDS-PAGE gel and exemplar (b.) size-exclusion chromatography over a Superdex75 column for M1$_{P96H}$-Triplet-NT indicating >95% purity and homogeneity of the material.

VHH monomer-NT (M1-NT and H1-NT) and VHH-heterotrimer-NT (M1$_{P96H}$-triplet-NT) had characteristics consistent with expectation. Figure 4.4 and 4.5 showed the SDS-PAGE gel and exemplar size-exclusion column results of the VHH monomer-NT and VHH-heterotrimer-NT

86

after purification (Figure 4.4 and 4.5). VHH monomer-NTs had size around 14kDa (Figure 4.4) and VHH heterotrimer-NTs had size between 38-49kDa (Figure 4.5).

Histidine mutations could potentially impart pH dependence of binding [129]. Histidine protonation at lower pH-values can increase dissociation rate of antibodies to their receptors. Maeda et al. found that the dissociation rate was less rapid in the intracellular acidic compartments once histidine was deleted from human epidermal growth factor [130]. In this study, we generated different M1 variants based on the effect of histidine on VHH dissociation
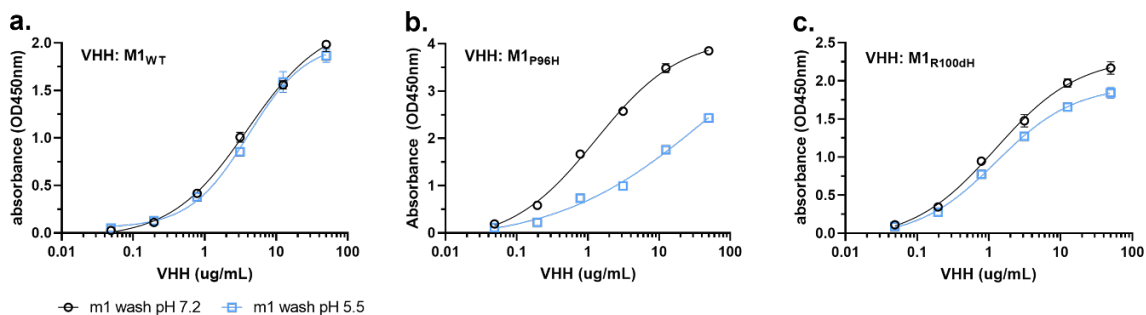
Figure 4.6. Histidine mutations impart a pH dependent dissociation effect in M1 VHH variants. M1 variants (a.) $M1_{WT}$, (b.) $M1_{P96H}$ and (c.) $M1_{R100dH}$ were incubated on mTfR coated ELISA plates, followed by a stringent wash with 1x PBS buffer at pH 7.2 or pH 5.5. Following pH dependent washing, the bound VHH was detected with an anti-alpaca-peroxidase antibody and the reaction terminated by addition of 1M HCl. Error bars represent the standard deviation of the mean values at each data point.

rate. Figure 4.6 shows the mTfR ELISA on M1 variants: $M1_{P96H}$, $M1_{WT}$ and $M1_{R100dH}$ (Figure 4.6). Comparing M1 variant binding to mTfR under normal physiological pH (pH = 7.2) and acidic pH (pH = 5.5), lower pH did not alter the dissociation of $M1_{WT}$ to mTfR but substantially impacted the dissociation of $M1_{P96H}$ to mTfR.

87
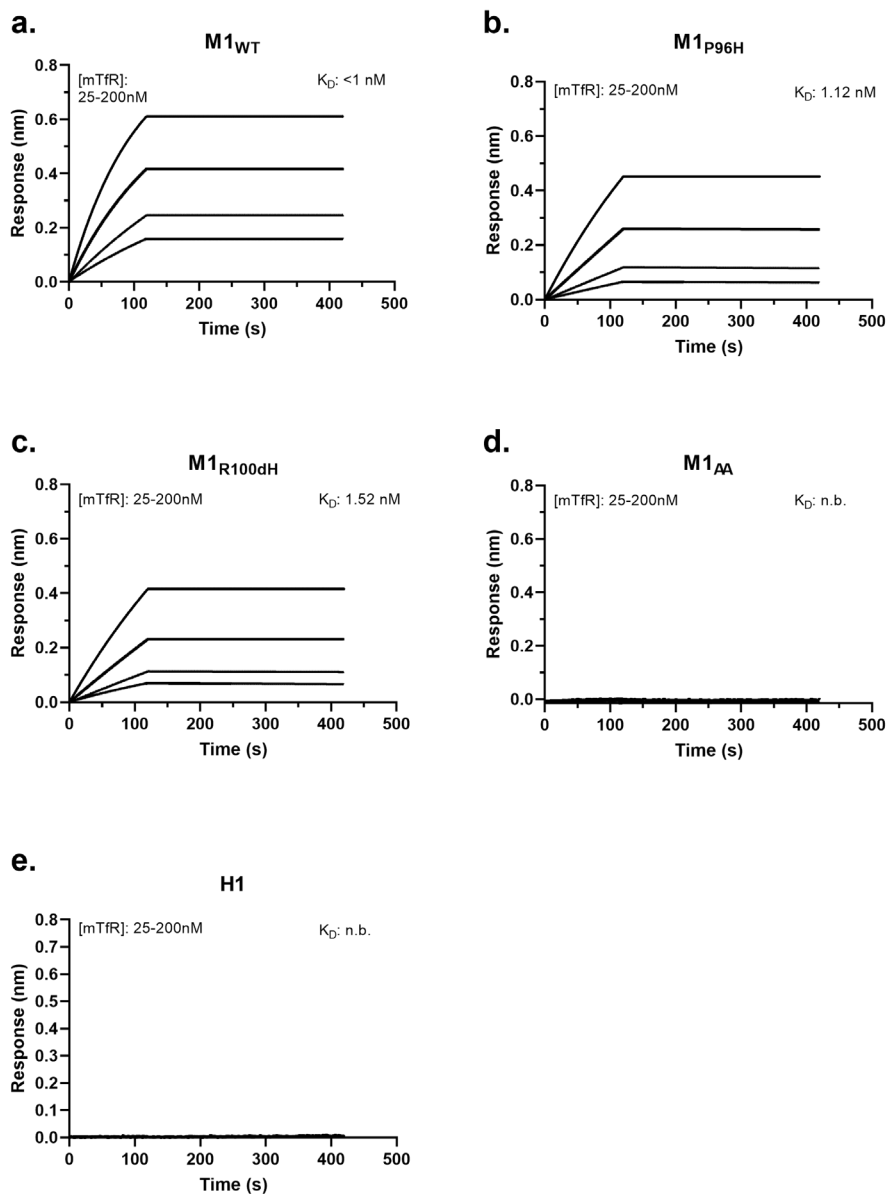
Figure 4.7. Affinity binding curves of the five M1-NT variants: M1$_{WT}$-NT (a.), M1$_{P96H}$-NT (b.), M1$_{R100dH}$-NT (c.), M1$_{AA}$-NT (d.) and H1-NT (e.) binding affinity (K$_D$) to mTfR. Using biolayer interferometry on an Octet Red96 system, association and dissociation rates were determined by immobilizing biotinylated VHH onto streptavidin-coated optical sensors. The M1-NT variant association and dissociation curves to mTfR were plotted and the affinity of each to mTfR was calculated. (n.b. = no binding)

Then the affinity of M1 variants to mTfR was measured using Octet. Based on Octet

measurement, the affinity (K$_D$) of M1$_{WT}$-NT, M1$_{P96H}$-NT, and M1$_{R100dH}$-NT to mTfR were

<1nM, 1.12nM, 1.52nM. While the affinity (K$_D$) of M1$_{AA}$-NT and H1-NT to mTfR was not

detectable. Figure 4.7 shows the association and dissociation curves of the $M1_{WT}$-NT, $M1_{P96H}$-NT, $M1_{AA}$-NT, $M1_{R100dH}$-NT and H1-NT to mTfR. $M1_{WT}$-NT, $M1_{P96H}$-NT, and $M1_{R100dH}$-NT bond to mTfR well while $M1_{AA}$-NT and H1-NT showed no binding.

4.4.3 M1 variant screening for BBB transcytosis using neurotensin fusion and hypothermia assessment

To assess BBB transcytosis ability, several M1 variants were fused to NT and screened based on the extent of hypothermia effects. Three M1 variant NT fusions, including $M1_{WT}$-NT, $M1_{R100dH}$-NT and $M1_{P96H}$-NT were injected to WT mice. NT alone was injected into WT mice
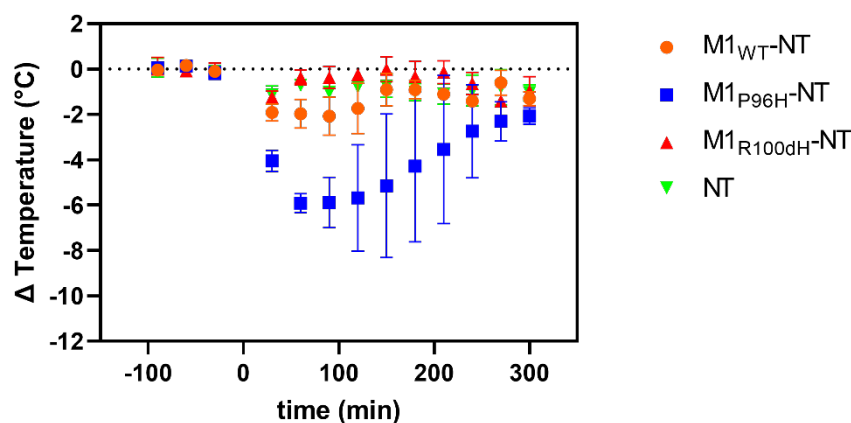
Figure 4.8. The use of NT fusion to VHHs for VHH screening via hypothermia as an indication of CNS target engagement. The M1 variants with different affinities to mTfR have different hypothermic effects. Among the three M1 variants injected to mice at the same dose 600nmol/kg body weight (n = 3 per group), $M1_{P96H}$-NT produced the most prominent hypothermia effect, with a maximum temperature drop of about 6°C and duration for about 4hrs.

at the same molarity as an initial negative control. At a dose of 600nmol/kg body weight, the M1 variants with different binding affinities to mTfR show different hypothermia effects (Figure 4.8). $M1_{WT}$-NT reduced temperatures by approximately 2°C, with an effect that lasted approximately 2 hours. $M1_{P96H}$-NT, at the same dose, decreased temperature by 6°C with effects that lasted more than 4 hours, indicating that $M1_{P96H}$-NT appeared to improve CNS penetration. NT alone did not show any hypothermia effect, indicating that peripherally

administered NT alone does not appear to cross the BBB into the CNS. M1$_{R100dH}$-NT gave less

than 2°C of hypothermia effect. Mouse body temperatures were stable at baseline.

To confirm and extend these findings, a blinded experiment was performed. The previous three
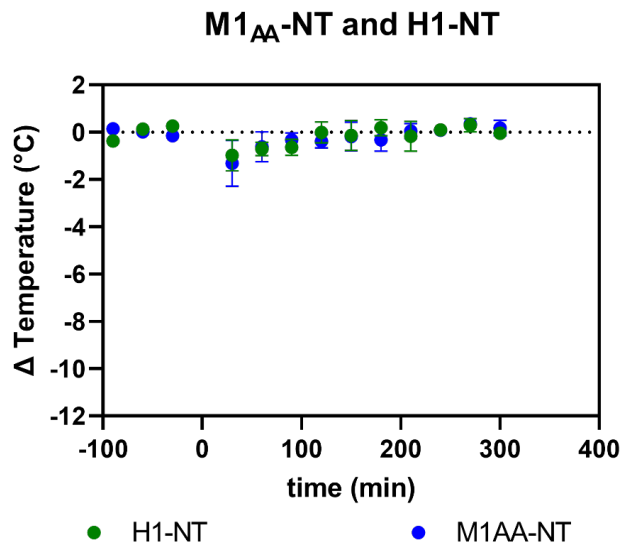
Figure 4.9. Lack of hypothermic effect with mTfR non-binding VHH-NT fusions. M1$_{AA}$-NT and H1-NT were injected at doses of 1400nmol/kg body weight. M1$_{AA}$-NT and H1-NT lack prominent hypothermia effects (n=3 per group).

M1 variants, plus a fourth mutant M1$_{AA}$-NT that has minimal TfR binding and a different

VHH that binds to human TfR called H1 were tested by an investigator blinded to the identity

of the injected materials. M1$_{AA}$-NT and H1-NT were tested at a higher molarity in a previous

experiment and showed no obvious hypothermia effects (Figure 4.9). The blinded experiment

results were consistent with the previous finding: M1$_{P96H}$-NT clearly reduced the temperature

the most, with a maximum drop of about 4°C. The other M1-NTs and H1-NT did not reduce

the temperature substantially (Figure 4.10). These results indicate that temperature

measurement experiments facilitated the identification of an anti-mTfR VHH variant which
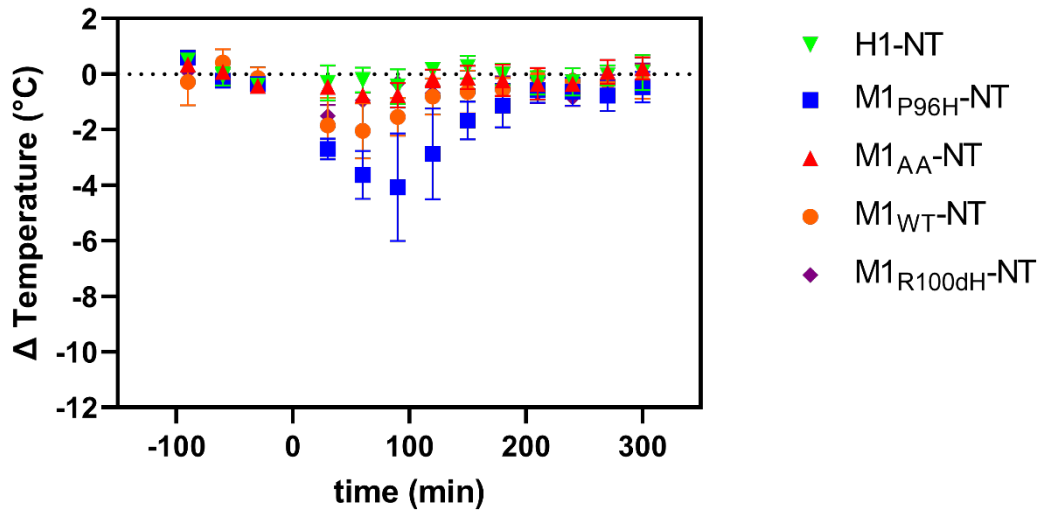
Figure 4.10. Hypothermic effect of M1 VHH-NT fusions in a randomized, blinded cohort. Five VHH-NT fusions M1$_{WT}$-NT, M1$_{P96H}$-NT, M1$_{AA}$-NT, M1$_{R100dH}$-NT and H1-NT were blinded by an independent investigator. Each blinded VHH-NT fusion was injected in a randomized fashion at a dose of 600nmol/kg body weight (n=3 per group) and body temperature measured over the indicated time interval. Following complete data collection of the temperature measurements, the results were unblinded. Consistent with previous finding, M1$_{P96H}$-NT gave the most prominent hypothermia effect.

induced substantial CNS effects.

4.4.4   M1$_{P96H}$-NT dose effect

To understand whether the amount of M1$_{P96H}$-NT injected to mice affects the extent of

hypothermia effects, we injected M1$_{P96H}$-NT to WT mice at four different doses: 67nmol/kg

body weight, 200nmol/kg body weight, 600nmol/kg body weight, and 1800nmol/kg body

weight. Twelve mice were used in this experiment, with three mice at each dose (Figure 4.11).

At the two lower doses, there was minimal hypothermia effects. With increased M1P96H-NT

concentration, the maximum temperature drop increased to about 8C° and also the duration of

hypothermia was extended to as long as 5 hours. Thus, these was an apparently monotonic
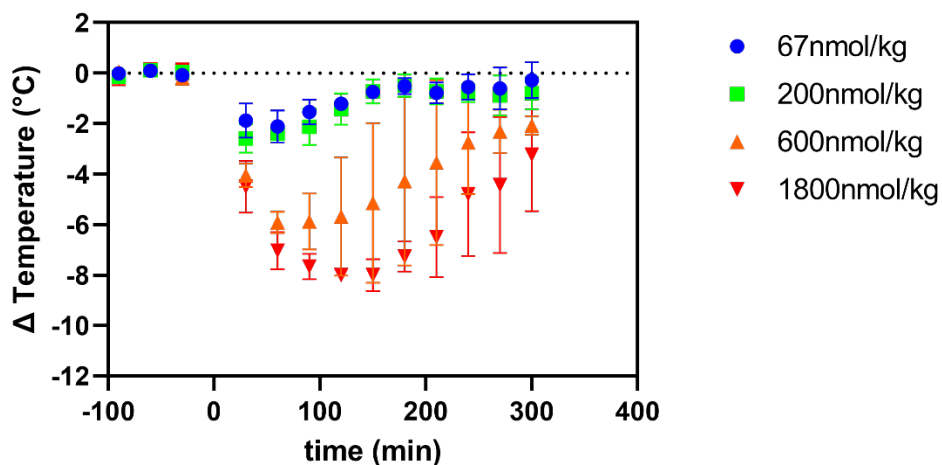
Figure 4.11. M1$_{P96H}$-NT dose effect in WT mice after IV injection. This figure shows the dose effect of M1$_{P96H}$-NT in WT mice after tail vein injection (n = 3 per group). The hypothermia effect was stronger and lasted longer time with dose increased from 67nmol/kg body weight to 1800nmol/kg body weight.

dose-response relationship between intravenous M1$_{P96H}$-NT and hypothermia.

4.4.5 Temperature effect of M1$_{P96H}$-Triplet-NT

Based on the octet results and temperature measurement, M1$_{P96H}$ was chosen as the variant to
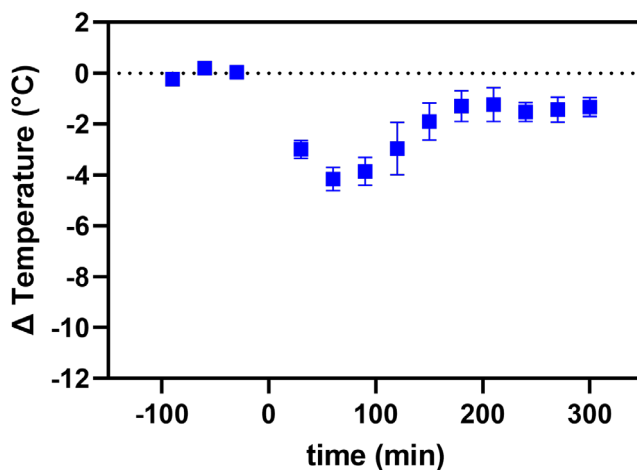
Figure 4.12. Measurement of M1$_{P96H}$-Triplet-NT hypothermia effect. M1$_{P96H}$-Triplet-NT was injected at dose of 600nmol/kg body weight (n = 3) and caused a temperature drop of about 4C°.

use to assess ability to cross the BBB after conjugating to a payload. As a proof of concept, we

92

used the anti-Aβ VHH dimer Nb3-Nb3 as the payload fused in a single polypeptide with

M1$_{P96H}$ and NT and named M1$_{P96H}$-Triplet-NT, the M1$_{P96H}$-Triplet NT, was injected

intravenously into three WT mice. Body temperature was measured as described in the

Temperature measurement section. Figure 4.12. shows the temperature change after tail vein

injection of M1$_{P96H}$-Triplet-NT. There was about 4°C temperature drop after the intravenous

injection and the hypothermia effect peaked at about 1 hour post injection. This result

confirmed that after fusing to an anti-Aβ VHH dimer payload, the M1$_{P96H}$-Triplet-NT was still

able to get across the BBB and exert a CNS effect.

4.4.6 Affinity measurement of VHH-Triplet

To confirm that fusion with Nb3-Nb3 did not affect the binding ability of M1$_{P96H}$ and Nb3-

Nb3 dimer to their targets, the affinity of M1P96H-triplet to mTfR and to Aβ were measured to be

1.63nM and 9.98nM using Octet (Figure 4.13). The affinity of the M1$_{P96H}$-triplet to mTfR was
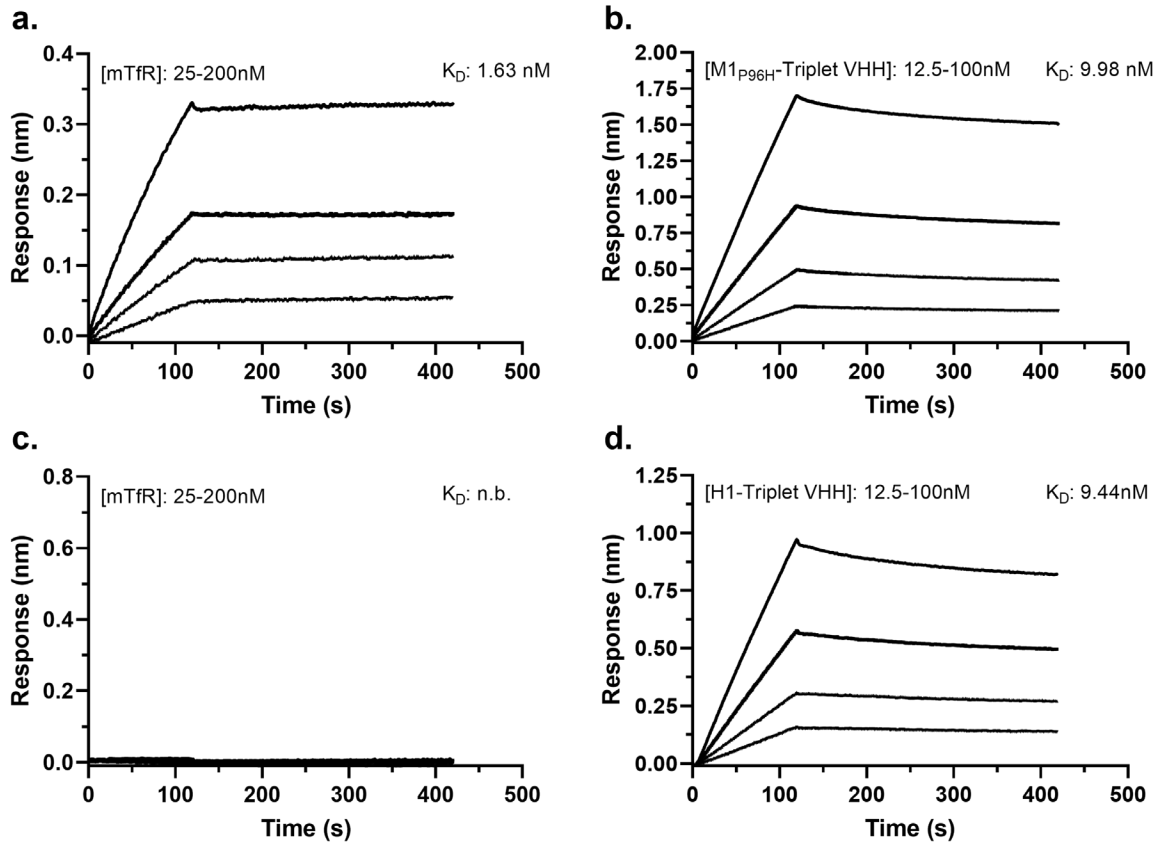
Figure 4.13. Affinity binding curves of M1$_{P96H}$-triplet-NT and H1-triplet-NT binding affinity (K$_D$) to mTfR and Aβ. Using biolayer interferometry on a Octet Red96 system, association and dissociation rates were determined by immobilizing biotinylated VHH (a, c) or biotinylated amyloid beta (b, d) onto streptavidin-coated optical sensors. M1$_{P96H}$-triplet-NT association and dissociation curve to (a) mTfR and (b) Aβ. The affinity of M1$_{P96H}$-triplet-NTwas measured to be 1.63nM to mTfR and 9.98nM to Aβ. H1-triplet-NT association and dissociation curve to (c) mTfR and (d) Aβ. The affinity of H1-triplet-NT was measured to be 9.44nM to Aβ and no binding to mTfR. (n.b. = no binding)

on the same order before and after the fusion. The affinity of H1-Triplet-647 to mTfR and Aβ

was also assessed using Octet and measured to be no binding to mTfR and 9.44nM to Aβ

(Figure 4.13). It was verified that the fusion of $_{M1P96H}$ and H1 to VHH dimer Nb3-Nb3 did not

change their binding affinities.

To ensure that the dye labeling did not affect $_{M1P96H}$-triplet binding to mTfR, a mTfR ELISA

on M1$_{P96H}$-triplet before and after Alexa 647 dye labelling was performed. The binding curves
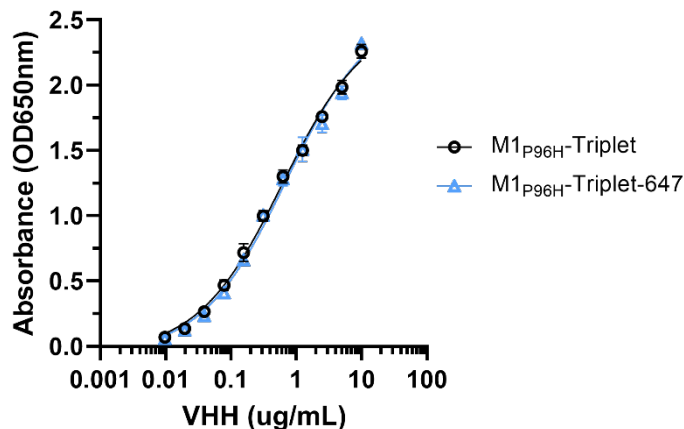
Figure 4.14. mTfR ELISA on $M1_{P96H}$-Triplet before and after 647 labelling. VHH was incubated with mTfR absorbed to ELISA plates and detected using an anti-alpaca-peroxidase antibody to determine the impact of fluorophore conjugation. The near overlapping binding curves indicate a lack of effect following fluorophore labelling. Error bars represent the standard deviation of the mean values at each data point.

before and after labeling overlapped with each other (Figure 4.14), indicating that the Alexa

647 dye labeling did not affect the binding.

4.4.7 Direct assessment of brain target engagement after intravenous injection of VHHs using confocal microscopy

VHH-Triplets were injected to APP/PS1 positive transgenic mice to directly assess brain target

(Aβ) engagement. Ten transgenic mice were randomized into two groups, with five mice in

each group. Five mice were injected with $M1_{P96H}$-Triplet-647 and five mice were injected with

H1-Triplet-647 as a negative control which does not bind to mTfR. Because the hypothermia

effect was most prominent in the first two hours post injection in previous experiments using

NT fusions, transgenic mice were sacrificed two hours post IV injection. Figure 4.15 shows

exemplar confocal images of brains injected with $M1_{P96H}$-triplet-647 or H1-triplet-647. From

the exemplar images, it appeared that most of the 647 signals were similar to background, with
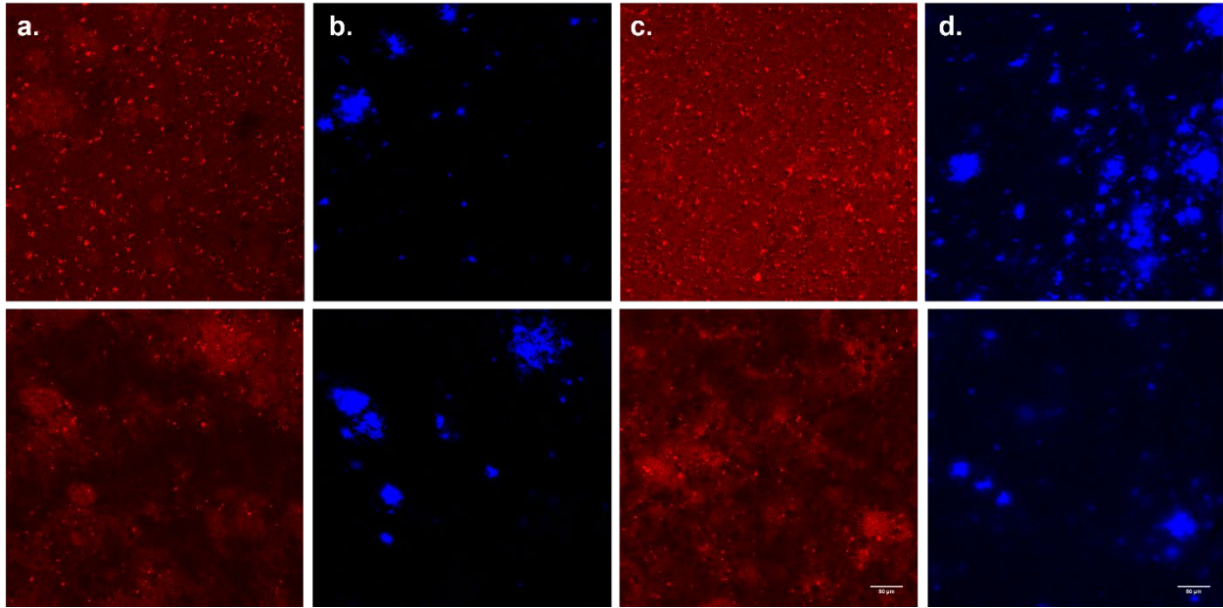
Figure 4.15. Representative immunofluorescent confocal microscopy of mice brains 2 hours after intravenous injection. 647 channel (a.) and X34 channel (b.) microscopy of mice brains injected with H1-Triplet-647. 647 channel (c.) and X34 channel (d.) microscopy of mice injected with M1$_{P96H}$-Triplet-647.

some areas that had morphology consistent with amyloid plaque labeling. However, surprisingly, the confocal imaging patterns were similar in both M1$_{P96H}$-triplet-647 and H1-triplet-647 injected mice, suggesting a modest amount of non-specific BBB crossing and Aβ plaque binding plus background autofluorescence, rather than the expected extensive mTfR-mediated transcytosis and Aβ plaque binding.

To confirm that the lack of anti-Aβ plaque binding after IV injection by M1$_{P96H}$-triplet-647 was not caused by the inability of the Nb3-Nb3 to label Aβ in the context of the M1$_{P96H}$-triplet-647 fusion construct, an ex vivo labeling experiment was performed. We labeled brain sections from a naïve APP/PS1 positive mouse with M1$_{P96H}$-Triplet-647 using modest concentrations and no antigen retrieval. Figure 4.16 shows that the Nb3-Nb3 dimer part of M1$_{P96H}$-Triplet-647 was able to bind to amyloid plaques, with substantially enhanced fluorescence signals in areas of plaques. Thus, the modest plaque labeling after intravenous injection with M1$_{P96H}$-triplet-
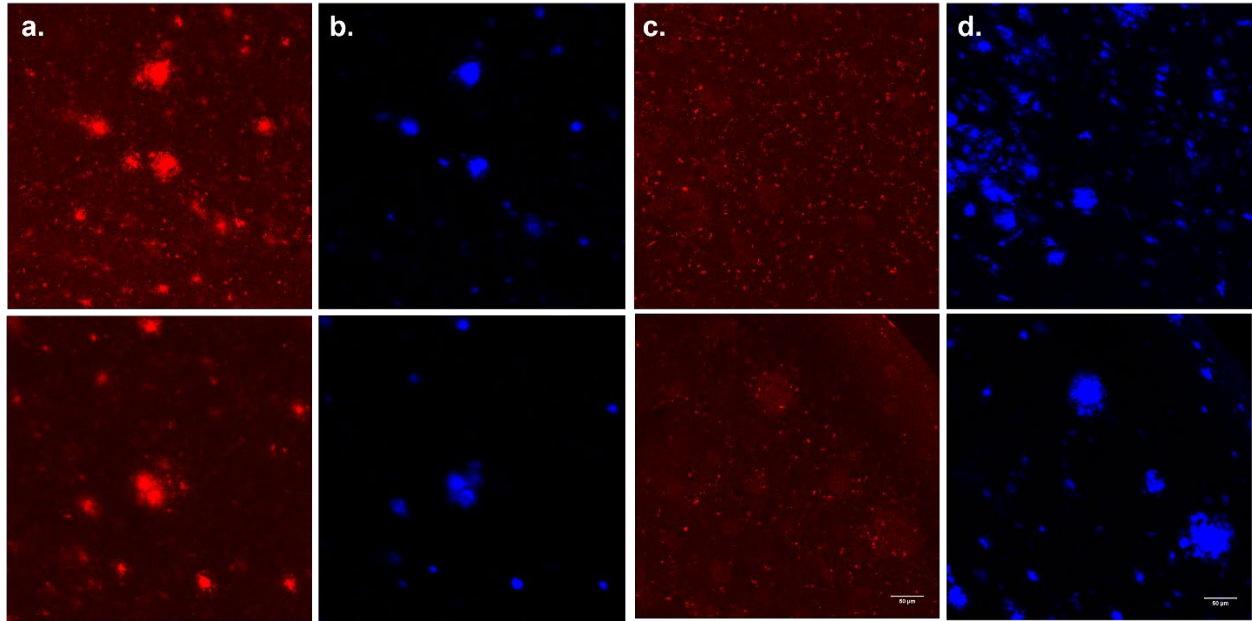
Figure 4.16. Representative immunofluorescent confocal microscopy of ex vivo APP/PS1 positive mouse brain sections. 647 channel (a.) and X34 channel (b.) microscopy of the ex vivo brain sections labeled with M1$_{P96H}$-Triplet-647. 647 channel (c.) and X34 channel (d.) microscopy of the ex vivo brain sections without M1$_{P96H}$-Triplet-647 labeling.

647 is not likely to be attributed to lack of plaque binding affinity. Autofluorescence was relatively modest in the 647 channel in sections labeled with only X34 (Fig. 4.16c-d).

Because of the possibility of subconscious bias in selecting regions for imaging and to assess for more subtle quantitative differences between M1$_{P96H}$-triplet-647 and H1-triplet-647 plaque labeling, we performed randomized, blinded, automated analyses of the brain sections to objectively compare the confocal imaging results. Eleven or twelve confocal stacks of images were acquired at randomly selected x, y coordinates in cortex (Figure 4.2). Confocal images of brain sections were processed using ImageJ for quantitative assessment.

The % area of X34 coverage, % area of Triplet-647 coverage and the % area ratio of Triplet-647/X34 coverage were averaged across the eleven to twelve images stacks acquired for each mouse brain. The average values of % area of each mouse brain was plotted in Figure 4.17. Comparing mouse brains injected with M1$_{P96H}$-triplet-647 or H1-triplet-647, the average
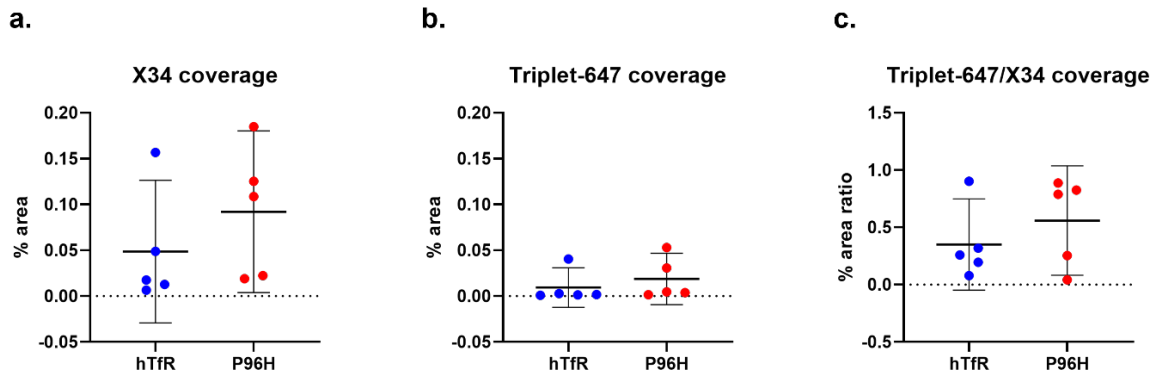
Figure 4.17. % area and % area ratio of X34 channel images and 647 channel images. a. The % area of X34 coverage in the X34 images. There was no significant difference for mice injected with H1-triplet-647 or M1$_{P96H}$-triplet-647; unpaired student t-test, p= 0.3341 b. The % area of Triplet-647 coverage in 647 channel images. There was no significant difference for mice injected with H1-triplet-647 or M1$_{P96H}$-triplet-647; unpaired student t-test, p = 0.4815. c. The % area ratio of Triplet-647/X34 coverage. There was no significant difference for mice injected with H1-triplet-647 or M1$_{P96H}$-triplet-647; unpaired student t-test, p = 0.3788. 647 channel images and the ratio of 647 channel/X34 channel images.

values of % area of Triplet-647 coverage/% area X34 coverage had no significant difference (Figure 4.17c). There was also no significant difference for % area X34 coverage or % area Triplet-647 coverage (Figure 4.17a, b).

4.4.8 Alternative Confocal Image Processing – thresholding and intensity measurement
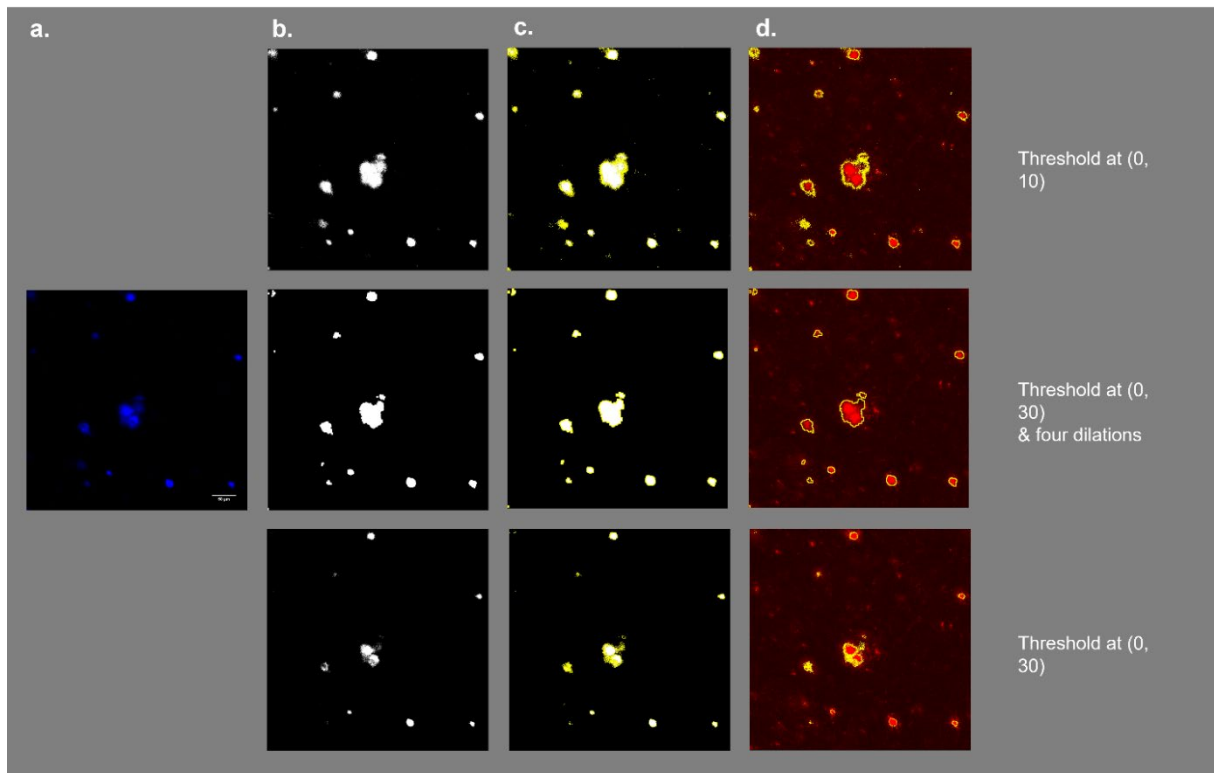
Figure 4.18. Averaged mean fluorescence in the 647 channel of plaques containing regions. a. The threshold for X34 images was set to be at (0, 10) There was no significant difference between the mean signals from mice injected with H1-triplet-647 and mice injected with M1$_{P96H}$-triplet-647; unpaired student t-test, p = 0.6404. b. The threshold for X34 images was set to be at (0, 30), then the image was eroded for four times. There was no significant difference between the mean signals from mice injected with H1-triplet-647 and mice injected with M1$_{P96H}$-triplet-647; unpaired student t-test, p = 0.5527. c. The threshold for X34 images was set to be at (0, 30). There was no significant difference between the mean signals from mice injected with H1-triplet-647 and mice injected with M1$_{P96H}$-triplet-647; unpaired student t-test, p = 0.4829.

To ensure the finding was not affected by the specific analysis method, confocal images of brain sections were analyzed in several alternative ways using ImageJ (Figure 4.18). First, X34 images were alternatively thresholded at (0, 10) and (0, 30) and were converted to binary images. Because amyloid-beta pathology can extend beyond the boundaries of X34 positive fibrillar plaque cores, the X34 images thresholded at (0, 30) were also processed with dilation in ImageJ to add pixels from the edges of plaques. These plaque and peri-plaque regions

99
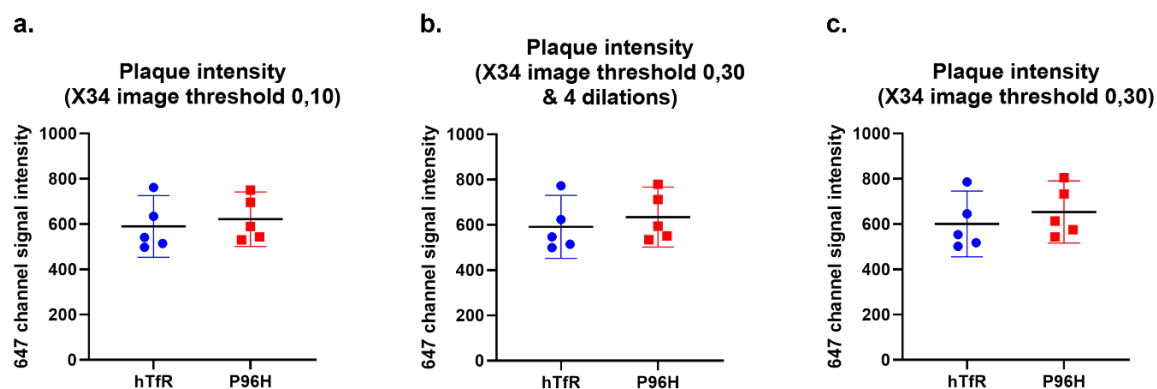
Figure 4.19. Quantitative analysis procedure for confocal images with thresholding followed by automated plaque selection and mean 647 channel signal calculation. An APP/PS1 positive naïve brain slice with ex vivo M1$_{P96H}$-Triplet-647 labeling was used as the example. Column a. shows a representative confocal microscope image of cortex X34 staining. Column b. shows the X34 labeled images after thresholding. Column c. shows automated selection of regions of plaques based on the thresholded images. Column d. shows the application of selected areas (from thresholded X34 images) to the 647 channel images.

identified on the X34 images were applied to the 647 channel images to calculate the mean 647 signal of these regions. The mean 647 signals were averaged across image stacks acquired for each mouse brain The average values of mean 647 signals of each brain were plotted in Figure 4.19. There was no significant difference of the mean 647 signal between the two groups in any of these analyses. These findings confirmed that there was no detectible receptor mediated transcytosis of $_{M1P96H}$-triplet-647 into the cortex, despite good evidence for a CNS effect for the same construct when fused to neurotensin.

4.5 Discussion

In this study, a modular system was designed to efficiently test the ability of anti-mTfR VHHs to cross the BBB using NT-induced hypothermia as a readout. Because only NT in the CNS can induce hypothermia effects [41, 47, 119, 131], experimentally measured hypothermia was used to infer the VHHs' ability to cross the BBB through transferrin receptor mediated transcytosis followed by VHH-NT fusion binding to neurotensin receptors. Using this NT-

based screening system, this study successfully identified an anti-mTfR VHH variant, M1$_{P96H}$, which has good binding properties to the mouse TfR and appeared to mediate BBB transport efficiently. To attempt to validate the ability of this anti-mTfR VHH to carry cargos across BBB, this anti-mTfR VHH was fused with an anti-Aβ VHH dimer and fused to NT. The M1$_{P96H}$-Triplet-NT retained substantial hypothermia effects after intravenous injection, confirming the BBB transcytosis ability of this triplet-NT fusion. However, the modular system for VHH screening does not appear to translate effectively into target binding in the cortex. To assess brain target engagement, M1$_{P96H}$-triplet was conjugated to the fluorescent Alexa 647 dye and the dye conjugates were injected intravenously into APP/PS1 positive transgenic mice. A similar VHH triplet dye conjugate, H1-triplet which does not binding mTfR was used as a control. Surprisingly, there was no significant difference of the amyloid plaque binding between these two VHH triplet dye conjugates. This result was not likely due to failure of plaque binding, because the VHH triplet dye conjugates bound plaques well in ex vivo experiments. Thus, the likely explanation for our findings was that the VHH triplet dye conjugates did not effectively cross the BBB in the cortex; the hypothermia effect induced by NT did not correspond to target engagement in cortex. The finding indicates that the use of NT as a rapid screening platform for anti-mTfR VHHs does not necessarily predict generalized cargo delivery across the BBB.

The lack of correspondence between NT induced hypothermia after intravenous injection and brain target engagement could be possibly explained by the concept that the BBB is not a unitary phenomenon, and the permeability of BBB may be different from brain region to brain region. The hypothalamus is the center for thermoregulation, and likely to be the site of action of NT in the brain. The preoptic area of hypothalamus contains microcircuitry through which

cutaneous and core thermal signals are integrated for thermoregulation and temperature homeostasis [132, 133]. Studies have found that the interface between the median eminence and the arcuate nucleus of the hypothalamus is somewhat leaky to molecules in the circulation [134, 135]. Cheunsuang et al. confirmed the specialized nature of median eminence and medial arcuate nucleus BBB by testing the distribution of hydroxystilbamidine and wheat germ agglutinin after intravenous injection [134]. They found that hydroxystilbamidine was taken into the median eminence and medial part of the arcuate nucleus, while the wheat germ agglutinin diffusely distributed in the arcuate nucleus and median eminence following intravenous injection. Furthermore, Morita and Miyata reported the accessibility of low molecular weight blood-derived molecules to the parenchyma in the median eminence and arcuate nucleus [136]. The hypothermia effect caused by NT binding to NT receptor is likely to be mediated in the hypothalamus [119]. Young et al. explored the distribution of NT receptors in rat brains and found moderate to high density of NT receptors in hypothalamus. The hypothermia effect was induced when NT was injected to medial, lateral preoptic and anterior area of the hypothalamus. Thus, the dissociation between robust NT-mediated hypothermia effects vs. negligible binding to amyloid plaques in cortex after IV injection could be explained by a relatively leaky hypothalamic BBB. Future studies will be required to directly test this possibility.

4.5.1 Limitations

There are several limitations of this study. First, although the $M1_{P96H}$-NT induced substantial hypothermia, the kinetics of this anti-mTfR VHH variant have not been fully optimized. Figure 4.7 shows that the dissociation rate of the $M1_{P96H}$ from mTfR was 1.33X10-4 which could be still too low. Based on Hultqvist et al., after the VHH binds to the TfR and the complex is

internalized, the VHH needs to dissociate from the TfR to get released efficiently into the brain parenchyma [137]. When the dissociation rate is too slow, VHHs may not unbind from the TfR and not get released into the brain parenchyma. Second, it is possible that dye modification with Alexa 647 affected BBB transcytosis even though it did not affect mTfR binding affinity in vitro (Figure 4.14). Alternative labeling strategies will need to be tested in future experiments. Reduction in autofluorescence due to lipofuscin [138] may also improve the sensitivity of fluorescent dye-based detection methods. Third, the APP/PS1 mice used in the study can also develop astrogliosis [139]. It is possible that the astrogliosis around the plaques could impair BBB transcytosis. Fourth, we do not know the mTfR binding epitope of M1, though it does not appear to interfere with transferrin binding (not shown). Also, it is formally possible, though unlikely, that older APP/PS1 transgenic mice have a less permeable BBB than young WT mice; we have not directly tested hypothermia effects in older APP/PS1 mice. A minor limitation is that the temperature measurement was conducted using an infrared thermometer. Although belly fur was removed to decrease variation and increase the accuracy and precision of temperature measurement, the use of infrared thermometer to measure belly temperature still introduces inter- and intra- user error. Also, the mice need to be anesthetized for acquisition of a steady temperature using the thermometer. Although we kept the anesthesia time short (about 20 sec) each time to minimize the influence of anesthesia on mouse body temperature. The use of anesthesia still introduced extra variations. Other temperature measurement methods such as the use of implanted thermometers which provide real-time temperature readings and eliminate interference with mice should be considered for future experiments. Finally, we acknowledge that only one brain section posterior to bregma was analyzed for each mouse. More brain sections for each mouse which cover additional brain

areas, including hypothalamus, will need to be imaged and analyzed in the future.

4.5.2 Future directions

There are many important future directions for this line of investigation. We are in the process

of screening other VHH variants for anti-mTfR and anti hTfR-mediated BBB transcytosis.

Because the NT induced hypothermia effect does not correspond to target engagement of

targets in other brain areas like cortex, an alternative, efficient approach to assess BBB

transcytosis is needed. To allow high throughput testing and prediction of therapeutic and

diagnostic agent delivery to the CNS, in vitro BBB models have been used. Cecchelli et al.

developed a human in vitro BBB model using cord blood-derived hematopoietic stem cells

[140]. This model shows good correlation between in vitro predicted ratio of unbound drug

concentration in brain and in vivo ratio reported in humans. Shayan et al. made a murine in

vitro BBB model using murine brain microvascular endothelial cells which also shows good

correlation of compound permeability compared with in vivo values [141]. However, these in

vitro models do not always reflect the in vivo BBB function. Garberg et al. evaluated multiple

different in vitro models in comparison with an in vivo mouse brain uptake assay to understand

the in vitro models' potential to predict in vivo transport of compounds across BBB [142].

Low correlations between in vitro and in vivo data were obtained with a total of twenty-two

compounds. Because of the complexity of the in vivo environment, in vitro BBB models were

not recommended to be used in isolation to assess target engagement in brain [143]. There are

many other methods to assess BBB transcytosis. For example, Stocki et al. tested the BBB

transcytosis of a variable domain of new antigen receptors (VNAR) TXB2 by fractionating

capillaries from the brain parenchyma and measured the concentration in capillaries and brain

parenchyma [41]. Yu et al. assessed the uptake of an anti-TfR antibody by homogenizing the

brain target areas and measuring the antibody concentration with ELISA [40]. A new screening platform will need to be established and tested in the future to facilitate of the discovery of optimal anti-mTfR VHHs.

There were no apparent safety concerns raised during the experiments reported here, but the safety profile of the VHHs will be formally assessed in the future to make sure that the binding of VHHs to the mTfR does not interfere with physiological iron uptake and that the foreign protein constructs do not cause major immunological responses or other toxicities.

In addition, extension of VHH fusion protein half-life in the circulation may improve BBB transcytosis. The half-life of single VHHs and VHH triplets was measured to be 2-3 minutes in the mouse after IV injection [144]. The lack of differences in brain signal may be caused by the fast clearance of the VHHs, which did not allow enough VHHs to bind to the TfR on the brain endothelial cells. Conjugation of the VHHs to albumin binding domains, immunoglobulin Fc domains or PEG to prolong VHH' half-lives will be tested in the future [145-147].

While not directly related to the main aims of the project involving development of brain MRI molecular contrast agents, the mechanisms underlying potential differences in BBB function in the hypothalamus vs. cortex are worthy of further investigation. To begin, target engagement of the Triplet-647 in hypothalamus will need to be assessed. The hypothalamus area of the brain sections will be imaged with confocal microscope and analyzed using ImageJ. Then, the $M1_{P96H}$ could be conjugated to nanobodies against another widely distributed endogenous target such as the ATP-gated ion channel P2X7, which is widely distributed throughout the brain [148]. $M1_{P96H}$-anti P2X7 VHH fusion would then be intravenously injected to mice and its target engagement in cortex and hypothalamus would be assessed and compared. Furthermore,

different sizes of dextrans could be intravenously injected to the mice to understand the BBB penetration capacity in hypothalamus and other brain regions [136].

The ultimate goal of this study is to develop a family of molecular MRI contrast agents for diagnosis and assessment of neurodegenerative diseases. Misdiagnosis of neurodegenerative diseases is common because of their heterogeneous nature [149]. Early diagnosis of neurodegenerative diseases could help with early treatments and delay hospitalization, and accurate identification of target populations could help with the development of new treatments [149, 150]. MRI has been widely used for imaging neurodegenerative diseases; however, structural MRI provides indirect and nonspecific measurements. Neurodegenerative diseases are characterized by abnormal accumulation of misfolded proteins including α-synuclein, tau, TDP-43 and Huntingtin in the CNS. Novel families of MRI contrast agents with VHH and IONPs would allow visualization of pathologically specific biomarkers in the living human brain: each VHH would bind to the misfolded proteins while the IONPs provide T1 MRI signals. We have characterized the in vivo pharmacokinetics of the contrast agent and optimized the MRI sequence for MR T1 imaging [144, 151], but have not optimized BBB transcytosis of contrast agents. IONPs have been widely in a research context as MRI molecular contrast agents but are not typically used in clinical practice. Liu et al., developed an oligomer-specific scFv antibody W20 conjugated superparamagnetic iron oxide nanoparticles which specifically bound to oligomers in transgenic mouse models of Parkinson's disease or Huntington's disease and provided MRI signals [152]. Sillerud et al. synthesized an anti-AβPP conjugated superparamagnetic iron oxide nanoparticle for MRI detection of amyloid plaques in AD [24]. However, none of these contrast agents have provided optimal BBB penetration to allow high quality in vivo imaging. The ability of molecular contrast agents to cross the BBB

and bind to brain targets in sufficient quantity to give conspicuous MRI signals will need be tested with in vivo MR imaging in the future.

4.6 Conclusions

This study used a NT based modular system to screen anti-mTfR VHHs for transferrin receptor mediated transcytosis across BBB. A M1 variant, $_{M1P96H}$, was identified with good performance in inducing hypothermia, an effect which requires crossing the BBB. This M1 variant was fused to the anti-Aβ VHH dimer and labeled with Alexa 647. Surprisingly, however, the dye labelled VHH did not show detectible labeling of amyloid plaques compared with controls after intravenous injection into transgenic mice. Other methods assessing VHH BBB transcytosis will need to be developed for screening VHHs to facilitate the development of MRI molecular contrast agents.

Chapter 5: Future Directions

VHHs' binding affinities will need to be optimized in the future. As mentioned in chapter 4, the association and dissociate rate constants of the VHHs to mTfR will need to be adjusted to achieve optimal BBB transcytosis. Also, the NT based VHH screening system will need to be further explored to understand its lack of correspondence with fluorescence microscopy results. Meanwhile, an alternative, efficient approach to assess VHHs' BBB transcytosis could be developed to facilitate VHHs screening.

After identifying an appropriate anti-mTfR VHH for BBB transcytosis, the VHH will be conjugated to iron oxide nanoparticle and the contrast agent brain target engagement will be assessed using MRI. The NIR imaging and PK model will be used to optimize the contrast agent's kinetic in vivo and to find time points post intravenous injection for MR imaging. Also, radiological-pathological correlation study will be performed to understand the specificity of this contrast agent.

In the meantime, the VHH module of the contrast agent can be adjusted for other neurological diseases such as chronic traumatic encephalopathy, Parkinson's disease, prion diseases, etc. These neurological diseases could be identified using pathological hallmarks lesions such as tau, α-synuclein and protease-resistant prion protein [153, 154].

<u>References</u>

1.   Global Burden of Disease 2016 Neurology Collaborators, *Global, regional, and national burden of neurological disorders, 1990-2016: a systematic analysis for the Global Burden of Disease Study 2016.* Lancet Neurol, 2019. **18**(5): p. 459-480.

2.   Erkkinen, M.G., M.O. Kim, and M.D. Geschwind, *Clinical Neurology and Epidemiology of the Major Neurodegenerative Diseases.* Cold Spring Harb Perspect Biol, 2018. **10**(4).

3.   Srinivas, N., K. Maffuid, and A.D.M. Kashuba, *Clinical Pharmacokinetics and Pharmacodynamics of Drugs in the Central Nervous System.* Clinical Pharmacokinetics, 2018. **57**(9): p. 1059-1074.

4.   Sridhar, V., et al., *Pharmacokinetics and pharmacodynamics of intranasally administered selegiline nanoparticles with improved brain delivery in Parkinson's disease.* Nanomedicine, 2018. **14**(8): p. 2609-2618.

5.   Basaia, S., et al., *Automated classification of Alzheimer's disease and mild cognitive impairment using a single MRI and deep neural networks.* Neuroimage Clin, 2019. **21**: p. 101645.

6.   LaFerla, F.M. and S. Oddo, *Alzheimer's disease: Abeta, tau and synaptic dysfunction.* Trends Mol Med, 2005. **11**(4): p. 170-6.

7.   The Alzheimer's Association, *2021 Alzheimer's disease facts and figures.* Alzheimers Dement, 2021. **17**(3): p. 327-406.

8.   Graham, W.V., A. Bonito-Oliva, and T.P. Sakmar, *Update on Alzheimer's Disease Therapy and Prevention Strategies.* Annu Rev Med, 2017. **68**: p. 413-430.

9.   Takizawa, C., et al., *Epidemiological and economic burden of Alzheimer's disease: a systematic literature review of data across Europe and the United States of America.* J Alzheimers Dis, 2015. **43**(4): p. 1271-84.

10.   Risacher, S.L. and A.J. Saykin, *Neuroimaging and other biomarkers for Alzheimer's disease: the changing landscape of early detection.* Annu Rev Clin Psychol, 2013. **9**: p. 621-48.

11.   Clark, C.M., et al., *Biomarkers for early detection of Alzheimer pathology.* Neurosignals, 2008. **16**(1): p. 11-8.

12. Beach, T.G., et al., *Accuracy of the clinical diagnosis of Alzheimer disease at National Institute on Aging Alzheimer Disease Centers, 2005-2010.* J Neuropathol Exp Neurol, 2012. **71**(4): p. 266-73.

13. ten Kate, M., et al., *MRI predictors of amyloid pathology: results from the EMIF-AD Multimodal Biomarker Discovery study.* Alzheimer's Research & Therapy, 2018. **10**(1): p. 100.

14. Morris, E., et al., *Diagnostic accuracy of 18F amyloid PET tracers for the diagnosis of Alzheimer's disease: a systematic review and meta-analysis.* European Journal of Nuclear Medicine and Molecular Imaging, 2016. **43**(2): p. 374-385.

15. Alphandéry, E., *Biodistribution and targeting properties of iron oxide nanoparticles for treatments of cancer and iron anemia disease.* Nanotoxicology, 2019. **13**(5): p. 573-596.

16. Rubio, I.T., et al., *The superparamagnetic iron oxide is equivalent to the Tc99 radiotracer method for identifying the sentinel lymph node in breast cancer.* Eur J Surg Oncol, 2015. **41**(1): p. 46-51.

17. Ma, D., et al., *Zwitterion-coated ultrasmall iron oxide nanoparticles for enhanced T1-weighted magnetic resonance imaging applications.* Journal of Materials Chemistry B, 2017. **5**(35): p. 7267-7273.

18. Kim, B.H., et al., *Large-scale synthesis of uniform and extremely small-sized iron oxide nanoparticles for high-resolution T1 magnetic resonance imaging contrast agents.* J Am Chem Soc, 2011. **133**(32): p. 12624-31.

19. Ta, H.T., et al., *Molecular imaging of activated platelets via antibody-targeted ultra-small iron oxide nanoparticles displaying unique dual MRI contrast.* Biomaterials, 2017. **134**: p. 31-42.

20. Nahrendorf, M., et al., *Noninvasive vascular cell adhesion molecule-1 imaging identifies inflammatory activation of cells in atherosclerosis.* Circulation, 2006. **114**(14): p. 1504-11.

21. Barrow, M., et al., *Design considerations for the synthesis of polymer coated iron oxide nanoparticles for stem cell labelling and tracking using MRI.* Chem Soc Rev, 2015. **44**(19): p. 6733-48.

22. Tarin, C., et al., *Targeted gold-coated iron oxide nanoparticles for CD163 detection in atherosclerosis by MRI.* Scientific Reports, 2015. **5**(1): p. 17135.

23. Wei, H., et al., *Exceedingly small iron oxide nanoparticles as positive MRI contrast agents.* Proc Natl Acad Sci U S A, 2017. **114**(9): p. 2325-2330.

24.   Sillerud, L.O., et al., *SPION-enhanced magnetic resonance imaging of Alzheimer's disease plaques in AβPP/PS-1 transgenic mouse brain.* J Alzheimers Dis, 2013. **34**(2): p. 349-65.

25.   Singh, N., et al., *Potential toxicity of superparamagnetic iron oxide nanoparticles (SPION).* Nano Rev, 2010. **1**.

26.   Piñero, D.J. and J.R. Connor, *Iron in the Brain: An Important Contributor in Normal and Diseased States.* The Neuroscientist, 2000. **6**(6): p. 435-453.

27.   Ropele, S. and C. Langkammer, *Iron quantification with susceptibility.* NMR Biomed, 2017. **30**(4).

28.   *Food and Drug Administration. Feraheme (ferumoxytol) Information.* https://www.fda.gov/drugs/postmarket-drug-safety-information-patients-and-providers/feraheme-ferumoxytol-information. June 2009.

29.   Toth, G.B., et al., *Current and potential imaging applications of ferumoxytol for magnetic resonance imaging.* Kidney Int, 2017. **92**(1): p. 47-66.

30.   Na, H.B., et al., *Versatile PEG-derivatized phosphine oxide ligands for water-dispersible metal oxide nanocrystals.* Chem Commun (Camb), 2007(48): p. 5167-9.

31.   Liu, J., et al., *PEGylation and zwitterionization: pros and cons in the renal clearance and tumor targeting of near-IR-emitting gold nanoparticles.* Angew Chem Int Ed Engl, 2013. **52**(48): p. 12572-6.

32.   Lee, G., et al., *Drug transporters in the central nervous system: brain barriers and brain parenchyma considerations.* Pharmacol Rev, 2001. **53**(4): p. 569-96.

33.   Pardridge, W.M., *Drug and gene targeting to the brain with molecular Trojan horses.* Nat Rev Drug Discov, 2002. **1**(2): p. 131-9.

34.   Oller-Salvia, B., et al., *Blood-brain barrier shuttle peptides: an emerging paradigm for brain delivery.* Chem Soc Rev, 2016. **45**(17): p. 4690-707.

35.   Malakoutikhah, M., M. Teixidó, and E. Giralt, *Shuttle-mediated drug delivery to the brain.* Angew Chem Int Ed Engl, 2011. **50**(35): p. 7998-8014.

36.   Bien-Ly, N., et al., *Transferrin receptor (TfR) trafficking determines brain uptake of TfR antibody affinity variants.* J Exp Med, 2014. **211**(2): p. 233-44.

37.   Gupta, Y., A. Jain, and S.K. Jain, *Transferrin-conjugated solid lipid nanoparticles for enhanced delivery of quinine dihydrochloride to the brain.* J Pharm Pharmacol, 2007. **59**(7): p. 935-40.

38.   Jefferies, W.A., et al., *Transferrin receptor on endothelium of brain capillaries.* Nature, 1984. **312**(5990): p. 162-3.

39.   Pardridge, W.M., J.L. Buciak, and P.M. Friden, *Selective transport of an anti-transferrin receptor antibody through the blood-brain barrier in vivo.* J Pharmacol Exp Ther, 1991. **259**(1): p. 66-70.

40.   Yu, Y.J., et al., *Boosting brain uptake of a therapeutic antibody by reducing its affinity for a transcytosis target.* Sci Transl Med, 2011. **3**(84): p. 84ra44.

41.   Stocki, P., et al., *Blood-brain barrier transport using a high affinity, brain-selective VNAR antibody targeting transferrin receptor 1.* Faseb j, 2021. **35**(2): p. e21172.

42.   Carraway, R. and S.E. Leeman, *The isolation of a new hypotensive peptide, neurotensin, from bovine hypothalami.* J Biol Chem, 1973. **248**(19): p. 6854-61.

43.   Ratner, C., et al., *Effects of Peripheral Neurotensin on Appetite Regulation and Its Role in Gastric Bypass Surgery.* Endocrinology, 2016. **157**(9): p. 3482-92.

44.   Martin, G.E., C.B. Bacino, and N.L. Papp, *Hypothermia elicited by the intracerebral microinjection of neurotensin.* Peptides, 1980. **1**(4): p. 333-9.

45.   Kokko, K.P., et al., *In vivo behavioral effects of stable, receptor-selective neurotensin[8-13] analogues that cross the blood-brain barrier.* Neuropharmacology, 2005. **48**(3): p. 417-25.

46.   Bissette, G., et al., *Hypothermia and intolerance to cold induced by intracisternal administration of the hypothalamic peptide neurotensin.* Nature, 1976. **262**(5569): p. 607-609.

47.   Wouters, Y., et al., *Identification and in vivo characterization of a brain-penetrating nanobody.* Fluids Barriers CNS, 2020. **17**(1): p. 62.

48.   Hamers-Casterman, C., et al., *Naturally occurring antibodies devoid of light chains.* Nature, 1993. **363**(6428): p. 446-8.

49.   Hassanzadeh-Ghassabeh, G., et al., *Nanobodies and their potential applications.* Nanomedicine (Lond), 2013. **8**(6): p. 1013-26.

50.   Harmsen, M.M. and H.J. De Haard, *Properties, production, and applications of camelid single-domain antibody fragments.* Appl Microbiol Biotechnol, 2007. **77**(1): p. 13-22.

51.   Oliveira, S., et al., *Rapid visualization of human tumor xenografts through optical imaging with a near-infrared fluorescent anti-epidermal growth factor receptor nanobody.* Mol Imaging, 2012. **11**(1): p. 33-46.

52.   Stijlemans, B., et al., *Efficient targeting of conserved cryptic epitopes of infectious agents by single domain antibodies. African trypanosomes as paradigm.* J Biol Chem, 2004. **279**(2): p. 1256-61.

53.   van der Linden, R.H., et al., *Comparison of physical chemical properties of llama VHH antibody fragments and mouse monoclonal antibodies.* Biochim Biophys Acta, 1999. **1431**(1): p. 37-46.

54.   Sheff, J., et al., *Defining the epitope of a blood–brain barrier crossing single domain antibody specific for the type 1 insulin-like growth factor receptor.* Scientific Reports, 2021. **11**(1): p. 4284.

55.   Stanimirovic, D.K.K., K.; Haqqani, A.S.; Sulea, T.; Arbabi-Ghahroudi, M.; Massie, B.; Gilbert, R., *Insulin-like growth factor 1 receptor-specific antibodies and uses thereof.* 2018.

56.   Danis, C., et al., *Inhibition of Tau seeding by targeting Tau nucleation core within neurons with a single domain antibody fragment.* Mol Ther, 2022. **30**(4): p. 1484-1499.

57.   Dupré, E., et al., *Single Domain Antibody Fragments as New Tools for the Detection of Neuronal Tau Protein in Cells and in Mice Studies.* ACS Chem Neurosci, 2019. **10**(9): p. 3997-4006.

58.   Ratain MJ, P.W.J., *Principles of Pharmacokinetics.*, in *Holland-Frei Cancer Medicine. 6th edition.*, P.R. Kufe DW, Weichselbaum RR, et al., Editor. 2003, BC Decker: Hamilton (ON).

59.   Lee, M.J., et al., *Rapid pharmacokinetic and biodistribution studies using cholorotoxin-conjugated iron oxide nanoparticles: a novel non-radioactive method.* PLoS One, 2010. **5**(3): p. e9536.

60.   Hoshyar, N., et al., *The effect of nanoparticle size on in vivo pharmacokinetics and cellular interaction.* Nanomedicine (Lond), 2016. **11**(6): p. 673-92.

61.   Kang, H., et al., *Pharmacokinetics, pharmacodynamics and toxicology of theranostic nanoparticles.* Nanoscale, 2015. **7**(45): p. 18848-62.

62.   Tong, S., et al., *Coating optimization of superparamagnetic iron oxide nanoparticles for high T2 relaxivity.* Nano Lett, 2010. **10**(11): p. 4607-13.

63.   Hamers-Casterman, C., et al., *Naturally occurring antibodies devoid of light chains.* Nature, 1993. **363**(6428): p. 446-448.

64.   Muyldermans, S., *Applications of Nanobodies.* Annu Rev Anim Biosci, 2021. **9**: p. 401-421.

65. Li, T., et al., *Camelid single-domain antibodies: A versatile tool for in vivo imaging of extracellular and intracellular brain targets.* J Control Release, 2016. **243**: p. 1-10.

66. Vandesquille, M., et al., *Chemically-defined camelid antibody bioconjugate for the magnetic resonance imaging of Alzheimer's disease.* MAbs, 2017. **9**(6): p. 1016-1027.

67. Rincon, M.Y., et al., *AAV mediated delivery of a novel anti-BACE1 VHH reduces Abeta in an Alzheimer's disease mouse model.* bioRxiv, 2019: p. 698506.

68. Esparza, T.J., et al., *High affinity nanobodies block SARS-CoV-2 spike receptor binding domain interaction with human angiotensin converting enzyme.* Scientific Reports, 2020. **10**(1): p. 22370.

69. Huo, J., et al., *Neutralizing nanobodies bind SARS-CoV-2 spike RBD and block interaction with ACE2.* Nature Structural & Molecular Biology, 2020. **27**(9): p. 846-854.

70. Dong, J., et al., *Development of humanized tri-specific nanobodies with potent neutralization for SARS-CoV-2.* Scientific Reports, 2020. **10**(1): p. 17806.

71. Schoof, M., et al., *An ultrapotent synthetic nanobody neutralizes SARS-CoV-2 by stabilizing inactive Spike.* Science, 2020. **370**(6523): p. 1473-1479.

72. Scully, M., et al., *Caplacizumab Treatment for Acquired Thrombotic Thrombocytopenic Purpura.* N Engl J Med, 2019. **380**(4): p. 335-346.

73. *Food and Drug Administration. FDA approved caplacizumab-yhdp* https://www.fda.gov/drugs/resources-information-approved-drugs/fda-approved-caplacizumab-yhdp. February 2019.

74. Ackaert, C., et al., *Immunogenicity Risk Profile of Nanobodies.* Front Immunol, 2021. **12**: p. 632687.

75. Vincke, C., et al., *General strategy to humanize a camelid single-domain antibody and identification of a universal humanized nanobody scaffold.* J Biol Chem, 2009. **284**(5): p. 3273-3284.

76. Knöbl, P., et al., *Integrated Safety Results from the Phase II and Phase III Studies with Caplacizumab in Patients with Acquired Thrombotic Thrombocytopenic Purpura.* Blood, 2018. **132**(Supplement 1): p. 3739-3739.

77. Lankveld, D.P., et al., *The kinetics of the tissue distribution of silver nanoparticles of different sizes.* Biomaterials, 2010. **31**(32): p. 8350-61.

78. Xue, W., et al., *Effects of core size and PEG coating layer of iron oxide nanoparticles on the distribution and metabolism in mice.* Int J Nanomedicine, 2018. **13**: p. 5719-5731.

79. Zhang, X., et al., *Oligoethyleneoxy-Modified (99m)Tc-Labeled β-Amyloid Imaging Probes with Improved Brain Pharmacokinetics for Single-Photon Emission Computed Tomography.* J Med Chem, 2018. **61**(3): p. 1330-1339.

80. Dogra, P., et al., *Establishing the effects of mesoporous silica nanoparticle properties on in vivo disposition using imaging-based pharmacokinetics.* Nat Commun, 2018. **9**(1): p. 4551.

81. Poulin, É., et al., *Optimization of the reference region method for dual pharmacokinetic modeling using Gd-DTPA/MRI and (18) F-FDG/PET.* Magn Reson Med, 2015. **73**(2): p. 740-8.

82. Alacam, B., et al., *Pharmacokinetic-rate images of indocyanine green for breast tumors using near-infrared optical methods.* Phys Med Biol, 2008. **53**(4): p. 837-59.

83. Lortie, M., et al., *Quantification of myocardial blood flow with 82Rb dynamic PET imaging.* European Journal of Nuclear Medicine and Molecular Imaging, 2007. **34**(11): p. 1765-1774.

84. Quan, S., et al., *Isolation of bacteria envelope proteins.* Methods Mol Biol, 2013. **966**: p. 359-66.

85. Luciano, M.P., et al., *A Nonaggregating Heptamethine Cyanine for Building Brighter Labeled Biomolecules.* ACS Chem Biol, 2019. **14**(5): p. 934-940.

86. Eeftens, J.M., et al., *Copper-free click chemistry for attachment of biomolecules in magnetic tweezers.* BMC Biophysics, 2015. **8**(1): p. 9.

87. Brudno, Y., et al., *In vivo targeting through click chemistry.* ChemMedChem, 2015. **10**(4): p. 617-20.

88. *The Math Works, Inc. MATLAB. (Version R2019b).*

89. Marini, F. and B. Walczak, *Particle swarm optimization (PSO). A tutorial.* Chemometrics and Intelligent Laboratory Systems, 2015. **149, Part B**: p. 153-165.

90. Shargel, L., & Yu, A. B. C., *Applied biopharmaceutics & pharmacokinetics.* 2012, New York: McGraw-Hill Education / Medical; 7 edition. 928.

91. Burnham, K. and D. Anderson, *Multimodel Inference: Understanding AIC and BIC in Model Selection.* Sociological Methods & Research, 2004. **33**(2): p. 261-304.

92. Debie, P., et al., *Effect of Dye and Conjugation Chemistry on the Biodistribution Profile of Near-Infrared-Labeled Nanobodies as Tracers for Image-Guided Surgery.* Mol Pharm, 2017. **14**(4): p. 1145-1153.

93. Sato, K., et al., *Effect of charge localization on the in vivo optical imaging properties of near-infrared cyanine dye/monoclonal antibody conjugates.* Mol Biosyst, 2016. **12**(10): p. 3046-56.

94. Longmire, M., P.L. Choyke, and H. Kobayashi, *Clearance properties of nano-sized particles and molecules as imaging agents: considerations and caveats.* Nanomedicine (Lond), 2008. **3**(5): p. 703-17.

95. Haraldsson, B., J. Nyström, and W.M. Deen, *Properties of the glomerular barrier and mechanisms of proteinuria.* Physiol Rev, 2008. **88**(2): p. 451-87.

96. Lawrence, M.G., et al., *Permeation of macromolecules into the renal glomerular basement membrane and capture by the tubules.* Proceedings of the National Academy of Sciences, 2017. **114**(11): p. 2958-2963.

97. Weissleder, R. and V. Ntziachristos, *Shedding light onto live molecular targets.* Nature Medicine, 2003. **9**(1): p. 123-128.

98. Xiang, H., et al., *Near-infrared phosphorescence: materials and applications.* Chemical Society Reviews, 2013. **42**(14): p. 6128-6185.

99. Maawy, A.A., et al., *Comparison of a chimeric anti-carcinoembryonic antigen antibody conjugated with visible or near-infrared fluorescent dyes for imaging pancreatic cancer in orthotopic nude mouse models.* J Biomed Opt, 2013. **18**(12): p. 126016.

100. Zaheer, A., et al., *In vivo near-infrared fluorescence imaging of osteoblastic activity.* Nature Biotechnology, 2001. **19**(12): p. 1148-1154.

101. Ash, C., et al., *Effect of wavelength and beam width on penetration in light-tissue interaction using computational methods.* Lasers Med Sci, 2017. **32**(8): p. 1909-1918.

102. Gadkar, K., et al., *Mathematical PKPD and safety model of bispecific TfR/BACE1 antibodies for the optimization of antibody uptake in brain.* Eur J Pharm Biopharm, 2016. **101**: p. 53-61.

103. Gobburu, J.V., et al., *Pharmacokinetic-pharmacodynamic modeling of rivastigmine, a cholinesterase inhibitor, in patients with Alzheimer's disease.* J Clin Pharmacol, 2001. **41**(10): p. 1082-90.

104. Nagashima, R., G. Levy, and R.A. O'Reilly, *Comparative pharmacokinetics of coumarin anticoagulants. IV. Application of a three-compartmental model to the analysis of the dose-dependent kinetics of bishydroxycoumarin elimination.* J Pharm Sci, 1968. **57**(11): p. 1888-95.

105. Uno, Y., et al., *A Three-Compartment Pharmacokinetic Model to Predict the Interstitial Concentration of Talaporfin Sodium in the Myocardium for Photodynamic Therapy: A*

Method Combining Measured Fluorescence and Analysis of the Compartmental Origin of the Fluorescence. Bioengineering (Basel), 2018. **6**(1).

106.   Benet, L.Z., *General treatment of linear mammillary models with elimination from any compartment as used in pharmacokinetics.* J Pharm Sci, 1972. **61**(4): p. 536-41.

107.   Sim, H., et al., *Pharmacokinetic modeling of tumor bioluminescence implicates efflux, and not influx, as the bigger hurdle in cancer drug therapy.* Cancer Res, 2011. **71**(3): p. 686-92.

108.   Nosrati, H., et al., *Bovine Serum Albumin (BSA) coated iron oxide magnetic nanoparticles as biocompatible carriers for curcumin-anticancer drug.* Bioorg Chem, 2018. **76**: p. 501-509.

109.   Li, Y., et al., *PEG-b-AGE Polymer Coated Magnetic Nanoparticle Probes with Facile Functionalization and Anti-fouling Properties for Reducing Non-specific Uptake and Improving Biomarker Targeting.* J Mater Chem B, 2015. **3**(17): p. 3591-3603.

110.   Liu, Z., et al., *Anti-biofouling polymer-decorated lutetium-based nanoparticulate contrast agents for in vivo high-resolution trimodal imaging.* Small, 2014. **10**(12): p. 2429-38.

111.   Patil, R.M., et al., *Comprehensive cytotoxicity studies of superparamagnetic iron oxide nanoparticles.* Biochem Biophys Rep, 2018. **13**: p. 63-72.

112.   Pradhan, P., et al., *Comparative evaluation of heating ability and biocompatibility of different ferrite-based magnetic fluids for hyperthermia application.* J Biomed Mater Res B Appl Biomater, 2007. **81**(1): p. 12-22.

113.   Gaasch, J.A., et al., *Brain iron toxicity: differential responses of astrocytes, neurons, and endothelial cells.* Neurochem Res, 2007. **32**(7): p. 1196-208.

114.   Wurtman, R., *Biomarkers in the diagnosis and management of Alzheimer's disease.* Metabolism, 2015. **64**(3 Suppl 1): p. S47-50.

115.   Wiley, D.T., et al., *Transcytosis and brain uptake of transferrin-containing nanoparticles by tuning avidity to transferrin receptor.* Proc Natl Acad Sci U S A, 2013. **110**(21): p. 8662-7.

116.   *Food and Drug Administration. FDA approved caplacizumab-yhdp.* February 2019.

117.   Ishiwatari-Ogata, C., et al., *Ozoralizumab, a Humanized Anti-TNFα NANOBODY® Compound, Exhibits Efficacy Not Only at the Onset of Arthritis in a Human TNF Transgenic Mouse but Also During Secondary Failure of Administration of an Anti-TNFα IgG.* Frontiers in Immunology, 2022. **13**.

118. D'Huyvetter, M., et al., *Phase I Trial of (131)I-GMIB-Anti-HER2-VHH1, a New Promising Candidate for HER2-Targeted Radionuclide Therapy in Breast Cancer Patients.* J Nucl Med, 2021. **62**(8): p. 1097-1105.

119. Young, W.S., 3rd and M.J. Kuhar, *Neurotensin receptor localization by light microscopic autoradiography in rat brain.* Brain Res, 1981. **206**(2): p. 273-85.

120. Pardon, E., et al., *A general protocol for the generation of Nanobodies for structural biology.* Nature Protocols, 2014. **9**(3): p. 674-693.

121. Paraschiv, G., et al., *Epitope structure and binding affinity of single chain llama anti-β-amyloid antibodies revealed by proteolytic excision affinity-mass spectrometry.* J Mol Recognit, 2013. **26**(1): p. 1-9.

122. Martin, A.C., *Accessing the Kabat antibody sequence database by computer.* Proteins, 1996. **25**(1): p. 130-3.

123. Jankowsky, J.L., et al., *Mutant presenilins specifically elevate the levels of the 42 residue beta-amyloid peptide in vivo: evidence for augmentation of a 42-specific gamma secretase.* Hum Mol Genet, 2004. **13**(2): p. 159-70.

124. Jankowsky, J.L., et al., *Co-expression of multiple transgenes in mouse CNS: a comparison of strategies.* Biomol Eng, 2001. **17**(6): p. 157-65.

125. Styren, S.D., et al., *X-34, a fluorescent derivative of Congo red: a novel histochemical stain for Alzheimer's disease pathology.* J Histochem Cytochem, 2000. **48**(9): p. 1223-32.

126. Mamat, U., et al., *Detoxifying Escherichia coli for endotoxin-free production of recombinant proteins.* Microbial Cell Factories, 2015. **14**(1): p. 57.

127. Varatharaj, A. and I. Galea, *The blood-brain barrier in systemic inflammation.* Brain Behav Immun, 2017. **60**: p. 1-12.

128. *Food and Drug Administration. Bacterial Endotoxins/Pyrogens. https://www.fda.gov/inspections-compliance-enforcement-and-criminal-investigations/inspection-technical-guides/bacterial-endotoxinspyrogens.* November 2014.

129. Schröter, C., et al., *A generic approach to engineer antibody pH-switches using combinatorial histidine scanning libraries and yeast display.* MAbs, 2015. **7**(1): p. 138-51.

130. Maeda, K., Y. Kato, and Y. Sugiyama, *pH-dependent receptor/ligand dissociation as a determining factor for intracellular sorting of ligands for epidermal growth factor receptors in rat hepatocytes.* J Control Release, 2002. **82**(1): p. 71-82.

131.   Tyler-McMahon, B.M., M. Boules, and E. Richelson, *Neurotensin: peptide for the next millennium.* Regul Pept, 2000. **93**(1-3): p. 125-36.

132.   Morrison, S.F., *Central control of body temperature.* F1000Res, 2016. **5**.

133.   Yoo, S. and S. Blackshaw, *Regulation and function of neurogenesis in the adult mammalian hypothalamus.* Prog Neurobiol, 2018. **170**: p. 53-66.

134.   Cheunsuang, O., A.L. Stewart, and R. Morris, *Differential uptake of molecules from the circulation and CSF reveals regional and cellular specialisation in CNS detection of homeostatic signals.* Cell and Tissue Research, 2006. **325**(2): p. 397-402.

135.   Haddad-Tóvolli, R., et al., *Development and Function of the Blood-Brain Barrier in the Context of Metabolic Control.* Front Neurosci, 2017. **11**: p. 224.

136.   Morita, S. and S. Miyata, *Accessibility of low-molecular-mass molecules to the median eminence and arcuate hypothalamic nucleus of adult mouse.* Cell Biochem Funct, 2013. **31**(8): p. 668-77.

137.   Hultqvist, G., et al., *Bivalent Brain Shuttle Increases Antibody Uptake by Monovalent Binding to the Transferrin Receptor.* Theranostics, 2017. **7**(2): p. 308-318.

138.   Chen, C., et al., *In Vivo Near-Infrared Two-Photon Imaging of Amyloid Plaques in Deep Brain of Alzheimer's Disease Mouse Model.* ACS Chem Neurosci, 2018. **9**(12): p. 3128-3136.

139.   Kamphuis, W., et al., *GFAP isoforms in adult mouse brain with a focus on neurogenic astrocytes and reactive astrogliosis in mouse models of Alzheimer disease.* PLoS One, 2012. **7**(8): p. e42823.

140.   Cecchelli, R., et al., *A stable and reproducible human blood-brain barrier model derived from hematopoietic stem cells.* PLoS One, 2014. **9**(6): p. e99733.

141.   Shayan, G., et al., *Murine in vitro model of the blood-brain barrier for evaluating drug transport.* Eur J Pharm Sci, 2011. **42**(1-2): p. 148-55.

142.   Garberg, P., et al., *In vitro models for the blood-brain barrier.* Toxicol In Vitro, 2005. **19**(3): p. 299-334.

143.   Stanimirovic, D.B., et al., *Blood-brain barrier models: in vitro to in vivo translation in preclinical development of CNS-targeting biotherapeutics.* Expert Opin Drug Discov, 2015. **10**(2): p. 141-55.

144.   Su, S., et al., *Pharmacokinetics of Single Domain Antibodies and Conjugated Nanoparticles Using a Hybrid near Infrared Method.* Int J Mol Sci, 2021. **22**(16).

145.   van Faassen, H., et al., *Serum albumin-binding V(H) Hs with variable pH sensitivities enable tailored half-life extension of biologics.* Faseb j, 2020. **34**(6): p. 8155-8171.

146.   Rotman, M., et al., *Fusion of hIgG1-Fc to 111In-anti-amyloid single domain antibody fragment VHH-pa2H prolongs blood residential time in APP/PS1 mice but does not increase brain uptake.* Nucl Med Biol, 2015. **42**(8): p. 695-702.

147.   Li, Q., et al., *Improved Inhibition of Tumor Growth by Diabody-Drug Conjugates via Half-Life Extension.* Bioconjug Chem, 2019. **30**(4): p. 1232-1243.

148.   Lord, B., et al., *A novel radioligand for the ATP-gated ion channel P2X7: [3H] JNJ-54232334.* Eur J Pharmacol, 2015. **765**: p. 551-9.

149.   Basak, I., et al., *microRNAs as neuroregulators, biomarkers and therapeutic agents in neurodegenerative diseases.* Cell Mol Life Sci, 2016. **73**(4): p. 811-27.

150.   Koikkalainen, J., et al., *Differential diagnosis of neurodegenerative diseases using structural MRI data.* Neuroimage Clin, 2016. **11**: p. 435-449.

151.   Kim, J.H., et al., *Sensitive detection of extremely small iron oxide nanoparticles in living mice using MP2RAGE with advanced image co-registration.* Scientific Reports, 2021. **11**(1): p. 106.

152.   Liu, X.G., et al., *ScFv-conjugated superparamagnetic iron oxide nanoparticles for MRI-based diagnosis in transgenic mouse models of Parkinson's and Huntington's diseases.* Brain Res, 2019. **1707**: p. 141-153.

153.   Skovronsky, D.M., V.M.-Y. Lee, and J.Q. Trojanowski, *NEURODEGENERATIVE DISEASES: New Concepts of Pathogenesis and Their Therapeutic Implications.* Annual Review of Pathology: Mechanisms of Disease, 2006. **1**(1): p. 151-170.

154.   McKee, A.C., et al., *The spectrum of disease in chronic traumatic encephalopathy.* Brain, 2013. **136**(Pt 1): p. 43-64.